

Four wave mixing at 1550 nm in silicon waveguides: enhancement and application

vorgelegt von

**Dipl.-Ing
M.Sc. Andrzej Gajda
geb. in Szczecin**

**von der Fakultät IV - Elektrotechnik und
Informatik der Technischen Universität Berlin
zur Erlangung des akademischen Grades**

**Doktor der Ingenieurwissenschaften
-Dr.-Ing-**

genehmigte Dissertation

Promotionsausschuss:

Vorsitzender: Prof. Dr. Bernd Tillack

Gutachter: Prof. Dr. Klaus Petermann

Gutachter: Prof. Dr. Juerg Leuthold

Gutachter: Dr. Lars Zimmermann

Tag der wissenschaftlichen Aussprache: 10. April 2017

Berlin 2017

Andrzej Gajda
**Four wave mixing at 1550 nm in silicon
waveguides:
enhancement and application**

Gratias autem Deo qui dat sapientiam

Acknowledgments

Even though it is unusual I would like to thank God for all the people that I have met on the long and hard way towards PhD degree.

I would like to thank Prof. Petermann for giving me the opportunity to accomplish my PhD in his research group in the institute "Hochfrequenztechnik/Photonics" at the Technische Universität Berlin. His guidance, support, encouragement and technical advises have been very precious.

I would like to express my appreciation to Dr. Lars Zimmermann, Prof. Bernd Tillack and Dr. Andreas Mai who gave me the opportunity to learn an advanced silicon photonics technology, and enabled possibility to fabricate the p-i-n waveguides and finish this thesis at IHP Microelectronics GmbH in Frankfurt(Oder). Advice and comments of Dr. Lars Zimmermann have been a great help in the development of this thesis.

I would like to acknowledge Dr. Jürgen Bruns who coordinated the project in the first part of the work. Here I would like to acknowledge all the people that contributed to the fabrication and measurements of the samples. My special thanks goes to Dave Stolarek and Hui Tian for their guidance in the process development and fabrication of the samples. I would like to thank Christian Mai, Dr. Dieter Knoll, Stefan Lischke for their advisory on samples production.

I have greatly benefited from Thomas Richter, Robert Elschner who helped with the expertise on high power measurement setup and dr. Colja Schubert for support with high power devices that enabled building the measurement setup for characterization of the first samples. My appreciation goes to Dr. Francesco Da Ros, Dr. Dragana Vukovic and Prof. Christophe Peucheret for a very productive and joyful time at the laboratory Danmarks Tekniske Universitet, even though I still did not manage to make sightseeing in Copenhagen. I would like to thank Dr. Mahmoud Al Jazayerifar and Giannino Dziallas for their support in numerical simulations of four-wave mixing in silicon of insulator waveguides. I would like to acknowledge Dr. Benjamin Wohlfeil for the simulations of the grating couplers. I am indebt to Georg Winzer for the late hours measurements and supporting discussions, although he was sometimes right. I am deeply grateful to Ania Peczek who patiently withstand my growing requests for the basic measurements on the samples.

Here I would like to acknowledge all the colleagues for their kindness, helpfulness and the friendly atmosphere and the pleasant time we spent together. My special thanks goes to friends from IHP and TU Berlin: Ania Peczek, Despoina Petousi, David Stolarek, Georg Winzer, Mariana Cascalheira, Maurizio Cirillo, Marcin Brzozowski, Marcel Kroh, Ivano Giunttoni, Karsten Voigt, Benjamin Wohlfeil, Maurizio Cirillo, Jesus Gutierrez Teran and all the others who kindly supported me in every-day struggling with scientific and not scientific problems.

Last but not least I would like to thank to my family. Especially my beloved wife Monika who gave me hand every time I thought I will never come to the end of this thesis. Monika and my great kids Alicja and Miłosz helped me a lot to find the everyday bright side of life. I would like to thank my parents Danuta and Jerzy Gajda and grandparents Irena Gajda, Wacława and Bronisław Kaczyński who constantly

asking for the progress in my thesis, did not allow me to even think about giving up. I am deeply grateful to my older sister Ola for her invaluable help in correcting the thesis. I believe that the long hours we've spent on it made it easier to understand. I would like to thank all the members of my big family for encouraging me to pursue my goals.

Berlin, September 2016

Table of contents

Introduction	1
1 Background theory	5
1.1 Relevant properties of silicon material	7
1.2 Propagation of light wave in silicon	10
1.2.1 Electrical susceptibility and polarization	10
1.2.2 Propagation of light in silicon waveguide	12
1.2.3 Nonlinear Schrödinger equation (NLSE) and nonlinear coefficient	14
1.2.4 Absorption and dispersion from free carriers and generation of free carriers by two photon absorption . .	15
1.2.5 Effective area	16
1.2.6 Self phase modulation	17
1.2.7 Cross phase modulation	18
1.2.8 Four-wave mixing	18
1.2.9 Four wave mixing simulation model	22
2 Numerical simulations of the SOI waveguide for CW four wave mixing	25
2.1 Optical properties approximation of applied materials . . .	25
2.1.1 Linear absorption of bulk Si	25
2.1.2 Two photon absorption and free carriers absorption induced by two-photon absorption	27
2.1.3 Material dispersion of silicon, silicon nitride and silicon oxide	27
2.2 Optical properties of silicon nano-rib waveguide with lateral p-i-n diode	29
2.2.1 Structure of the modeled waveguide	30
2.2.2 Mode of the silicon nano-rib waveguide	31
2.2.3 Dispersion in silicon nano-rib waveguides	32
2.2.4 Linear loss sources in a nano-rib waveguide with lateral p-i-n diode	34
2.2.5 Simulation of power dependent loss in silicon nano-rib waveguides	37
2.3 Simulations of CW four wave mixing in SOI waveguide . .	40
2.4 Reduction of free carrier lifetime	45
2.5 Electric simulations of free carrier lifetime in waveguide with lateral p-i-n diode	47

TABLE OF CONTENTS

3	Design, fabrication and characterization of samples	55
3.1	Samples design	56
3.2	Fabrication process	58
3.2.1	Process design	58
3.2.2	Manufacturing	60
3.3	Characterization of fabricated nonlinear waveguides	61
3.3.1	Electrical and opto-electrical characterization of waveguide based p-i-n diode	62
3.3.2	Dispersion	63
3.3.3	Linear loss	65
3.3.4	Linear loss dependence on bias voltage in p-i-n waveguides	66
3.3.5	Power dependent loss due to TPA and FCA	69
3.3.6	Continuous-wave four-wave mixing experiments . .	73
3.3.7	Phase sensitive amplification measurement	87
3.3.8	Summary of Continuous Wave (CW) Four Wave Mixing (FWM) and Phase Sensitive Amplification (PSA) measurement	91
4	System oriented experiments of wavelength conversion	93
4.1	All-optical wavelength conversion of the amplitude modulated signal	94
4.2	Phase regeneration of DPSK modulated signals	97
5	State of the Art	103
6	Conclusions	107
	List of Acronyms and Chemical Symbols	111
	List of symbols	113
	List of used constants	118
	Bibliography	119
	List of figures	132
	List of Publications	139

Introduction

Traffic in data communication networks has seen continuous growth over many decades. Taking the example of transport networks we observe a growth rate of about 60% per year in capacity. The increase in traffic is supported by various technologies but mainly driven by application related to social media, moving images, internet of things etc. An important contender for future increase of fiber optical network capacity is optical signal processing. Work on optical signal processing has developed over many decades, but only recently the integration platforms for optical signal processing have attracted increased attention. Nevertheless many nonlinear platforms for integrated optical signal processing are incompatible with the two major platforms for photonic and photonic-electronic integration which are indium phosphide and silicon. The platforms' maturity is an issue, because the main drivers behind the technological progress of the integrated photonic platforms are the common optical network applications such as coherent transmission, low cost optical links for data centers or switches. There is consensus that future growth of Internet will require photonic and photonic-electronic integration. Therefore it would be desirable to make use of the major platforms for nonlinear optical signal processing.

The work presented in this thesis was performed in the framework of a larger research project concerning the nonlinear optical signal processing on the silicon-on-insulator platform. Within this project different concepts were developed by several partners. Among others the particular projects focused on the following key issues: crystalline silicon, amorphous silicon and electro-optical polymers nonlinearity.

This thesis reports on the optical properties and numerical simulations of the silicon-on-insulator waveguide for continuous-wave four wave mixing. Moreover, it discusses the process of design, fabrication and characterization of samples. The purpose of the research activities was to construct an appropriate silicon waveguide supporting the FWM at the wavelengths around 1550 nm. The CW FWM can be used for the amplification of the signal, phase conjugation and wavelength conversion. Moreover, it can be useful for applications such as optical sampling, channel demultiplexing, pulse generation and high speed optical switching [1].

First of all the choice of silicon as a nonlinear optical material platform is motivated. Next the optical properties of the applied materials were set. It was a preparatory stage to establish the optical properties of silicon nanorib waveguide with lateral p-i-n diode. The mode field and an effective

INTRODUCTION

index of the silicon waveguide were determined with the optical simulations. Next, the dispersion of the waveguide was calculated considering different materials covering the waveguide. The problem of the free carriers accumulating in the waveguide rib was identified. According to the research of other authors in the past the p-i-n junction was proposed as an appropriate solution to this problem. The electrical simulations allowed to adapt the diode presented in the literature to the chosen waveguide geometry. The simulation of the nonlinear optical effects defined the direction of the design process. Next, the samples were fabricated in the BiCMOS pilot line at IHP GmbH.

Following the design and the fabrication process, the properties of the constructed waveguides with the lateral p-i-n diode were characterized. At first the linear loss of the waveguide was measured together with the loss and the bandwidth of the grating couplers. The latter were used for the in- and out-coupling light from the optical fiber to the waveguide. The optical loss from the free carriers was observed in the waveguide even for the low power of the light. This effect was also subject to the research within this project being the subject of this thesis.

Once the samples were optically and opto-electrically characterized, it was researched whether the constructed silicon with the lateral p-i-n diode can be used in the fiber optic communication system. In the first experiment session the wavelength conversion efficiency and the quality of the converted signal were tested. In the second experiment session it was investigated if, the phase of the differential phase shift keying Differential Phase Shift Keying (DPSK) signal can be regenerated, using the waveguide developed in this research project.

The research project was founded by Deutsche Forschung Gemeinschaft (DFG) and was realized in cooperation between Technische Universitaet Berlin (TUB) and Institute for High Performance Microelectronics (IHP) in Frankfurt(Oder) within the Joint Lab Silicon Photonics. The first characterization measurements were conducted with the support of the Fraunhofer Heinrich Herz Institut Fraunhofer Heinrich Herz Institute (HHI). The second characterization session was performed at the Danske Tekniske Universitet (DTU). Also there it was checked if the constructed silicon waveguides can be used in the fiber optic telecommunication system around the wavelength 1550 nm.

Number of people contributed to the work conducted in this research project. Mahmoud Jazayerifar and Gianino Dziallas created the tool for

the simulations of the FWM in the silicon waveguide. Benjamin Wohlfeil simulated the influence of the p and n doped regions on the optical loss of the silicon waveguide using JCM Wave software. The samples fabrication process at Innovation for High Performance Institute IHP was coordinated by David Stolarek. The Fraunhofer Heinrich Herz Institute supported the first measurement session with the necessary experimental hardware. The measurements performed at DTU were a joint experimental effort where the most of work was done by Francesco Da Ros, Dragana Vukovic, Christophe Peucheret and the author of this thesis.

In the thesis there are six chapters. Chapter 1 introduces the necessary background theory used in the design of structures. It starts with the comparison of the silicon material with the other possible nonlinear material platforms. Next the theoretical background is introduced for the following effects: the self phase modulation, cross phase modulation and four-wave mixing in silicon waveguide. Then we investigate optical properties of materials used in waveguide fabrication process with special attention given to dispersion and excess loss.

In chapter 2 the numerical simulations are described. At first the models of the optical properties of applied materials were discussed. Then the simulations of the following effects in a silicon waveguide are explained: mode profile, dispersion, linear and nonlinear loss, dispersion and CW four wavemixing. Later the electrical properties of a p-i-n diode lateral to the waveguide are discussed.

Chapter 3 presents realization and measurements of the silicon nano-rib p-i-n waveguide. The characterization of the samples covers linear loss measurements, power dependent loss measurements, current-voltage characteristics of the p-i-n diode, determination of Two Photon Absorption (TPA), FWM conversion efficiency, PSA that will be used in chapter 4 for realization of phase regeneration.

The fourth chapter 4 discusses advanced measurements of the feasibility of the p-i-n nano-rib waveguide for system applications. In this part of the thesis wavelength conversion of the 40 Gbps signal shall be demonstrated with a negligible power penalty of 0.2 dB due to applied 20V reverse bias voltage. The second system measurement utilized FWM based phase sensitive amplification of p-i-n silicon nano-rib waveguide, in order to dynamically regenerate 10 Gbps differential phase shift keying (DPSK) signal.

Chapter 5 reports on the state of the art in the CW FWM conversion effi-

INTRODUCTION

ciency, and showing the achievements of this research. The different approaches to avoid the free carriers absorption problem are discussed there as well.

In the sixth chapter the conclusions of the research project are summarized and recommendations for the future are outlined.

1

Background theory

The optical waveguides need to fulfill certain requirements to support four-wave mixing (FWM). At first in this chapter it will be discussed why silicon was chosen as a nonlinear material platform. The number of parameters will be introduced in order to compare the chosen Silicon On Insulator (SOI) platform with the other major platforms used for the same purpose. Moreover, the relevant properties of the silicon material and the waveguide structure shall be introduced. The silicon (Si) material was selected as the most appropriate for this research project. Furthermore, in this chapter, it is explained how to achieve the enhancement of the FWM by adjusting waveguide geometry. Electrical and optical approaches are used separately since, at the time of preparation of this thesis, there was no available software to model both at once.

Reason for the choice of silicon

Many material platforms were examined for the nonlinear optical effects. Table 1.1 presents a selection of the so called $\chi^{(3)}$ material platforms. It was examined which of them can be applied to obtain the optical Kerr effect around 1550 nm. Below, the material parameters relevant for the choice of the nonlinear platform are briefly discussed. A more detailed explanation of these quantities will be performed later in the thesis. The integration of photonic devices requires a light confinement on a sub-micron area. This can be realized only with the high real linear refractive index $n_{1,real}$, thus creating the structures with high refractive index contrast (Δn). The real part

of the nonlinear refractive index n_2 , known as well as Kerr coefficient, tells how much the refractive index of the medium changes with the optical intensity of the propagating light. The nonlinear coefficient γ results from both: the linear refractive index and the nonlinear refractive index. The higher are $n_{1\text{ real}}$ and n_2 , the higher can be γ . Vital parameters of the nonlinear optical material are the optical loss parameters α_{lin} and β_{TPA} . In table 1.1, the α_{lin} is the reported in the literature state-of-the-art linear loss of the realized nonlinear wave-guiding structures. The two photon absorption β_{TPA} , is a TPA coefficient related to the intensity of the guided light. The two photon absorption results from the simultaneous absorption of two photons by the material with the excitation of the atom or the molecule to the higher energy level [2]. In silicon it results in a generation of an electron-hole pair. The detrimental influence of the Free Carrier Absorption (FCA) is also presented in the table 1.1. In other materials, included in table 1.1 the β_{TPA} and FCA are negligible.

The obvious solution in the case of a fiber optic system would be applying a silica (silicon dioxide (SiO_2)) waveguide. With the advantages of the high coupling efficiency and the low linear propagation loss, the SiO_2 material could be easily incorporated in a fiber optic system. However, these waveguides have a large cross-section due to the low refractive index. Moreover, the low Kerr coefficient (n_2) requires a structure with the length of several hundred meters, in order to exhibit high nonlinear effect. Shorter structures can be achieved when using a material with a higher refractive index like called Hydrex [19, 20]. Waveguides made of this material perform with a low linear and nonlinear loss. At the same time Hydrex have ten times larger n_2 nonlinearity than SiO_2 . Due to its proprietary composition, the material is relatively little reported in the literature. A silicon nitride (silicon nitride (Si_3N_4)) material is another material platform known for the nonlinear optical effects. It performs with the higher $n_{1\text{ real}}$ and n_2 than in Hydrex and can be used to produce a low loss waveguide. However a Si_3N_4 waveguide still needs to be relatively long to provide an efficient nonlinear interaction.

Another step in the minimization of the nonlinear waveguide dimensions and increase in nonlinear parameters might be possible with arsenic sulfide (As_2S_3). The material enabling further decrease in the length of the nonlinear structures is amorphous silicon ($\alpha\text{-Si}$). Its high n_0 and high n_2 allows for a strong light confinement in the small waveguide cross-section, and thus short structures. However, the nonlinear interaction efficiency in this material is affected by a high α_{lin} and (TPA). Moreover the TPA in-

duces free carrier absorption (FCA) in amorphous silicon. Furthermore, the amorphous silicon material tends to change its properties with time and temperature as well [3]. Some polymers (e.g. DDMEBT) or III-V semiconductor materials could be used, since they have high n_2 coefficient. These two sets of materials give high flexibility in design of properties by change in chemical composition [4–7]. For the aluminum gallium arsenide ($\text{Al}_x\text{Ga}_{1-x}\text{As}$) a broadband, TPA-free FWM was obtained with a wavelength conversion efficiency of -9 dB [7] as well as a bandwidth of 750 nm. Nevertheless, fabrication of this kind of materials for nonlinear functionality might be challenging. Moreover, the integration of polymer based or III-V nonlinear waveguide on one of the two above mentioned platforms introduces additional complexity and thus cost. The last but not least important challenge is providing the material stable over time and able to withstand high powers.

The above mentioned materials proved to be highly efficient nonlinear materials, however, most of them are either not stable for a long period of time (e.g. α -Si) or difficult to fabricate aside electronic devices (e.g. As_2S_3). Another issue to be addressed, while thinking about realization of components is the reliability of the material platform. These problems can be overcome by a choice of crystalline silicon (c-Si) material. Very high real refractive index $n_{1\text{real}}$ and relatively high n_2 coefficient combined with a highly reliable technology make c-Si a competitive nonlinear optical material. The disadvantage of this material though remains its relatively high β_{TPA} and thus the presence of the free carrier absorption FCA.

1.1 Relevant properties of silicon material

There are several reasons for increasing interest in integrated photonics on SOI during the last few decades. The very large scale of integration (VLSI) complementary metal-oxide-semiconductor (CMOS) technology was developed on c-Si platform gave rise to the high interest in silicon photonic circuits development. In this section the material properties of c-Si that are relevant for the subject of this thesis will be introduced. They are summarized in the table 1.2 after [11, 16–20, 24, 25].

The dielectric constant (relative permittivity) ϵ_{Si} is the ratio between permittivities of the silicon and the vacuum. The energy gap (E_g) of sili-

CHAPTER 1. BACKGROUND THEORY

Material	n_1	$\frac{n_2}{\times 10^{-18}}$ [m ² /W]	$[W^{-1}m^{-1}]$	α_{lin} [dB/cm]	$\frac{\beta_{TPA}}{\times 10^{-11}}$ [m/W]	FCA
SiO ₂ [8]	1.47	0.026	0.011	0.2×10^{-7}	Negligible	No
Hydex [9–11]	1.5–1.9	0.12	0.23–0.25	0.05	Negligible	No
Si ₃ N ₄ [11]	2.0	0.26	1.4	0.5	Negligible	No
As ₂ S ₃ [12–15]	2.37	3	1.7–9.9	<0.25	<0.001	No
c-Si [11, 16–20]	3.47	2.4 - 14.5	300	<1	0.4–0.9	Decrease possible
α -Si [21, 22]	3.6	13	770	4	0.392	Present
α -Si [3]	3.6	21	1200	4.5	0.25	Present
Al _x Ga _{1-x} As [5]	n/a	14.5	81.6	0.74	Negligible	No
Al _{0.25} Ga _{0.75} As [4]	3.34	19.8	521	6	Negligible	No
DDMEBT [23]	1.8	20	n/a	n/a	Negligible	No
Al _{0.17} Ga _{0.83} As [6, 7]	3.3	26	660	1.4	Negligible	No

Table 1.1: Properties of potential CMOS compatible material platforms for efficient wavelength conversion around 1.55 μ m wavelength.

con provides information about the photon energy needed to create an electron-hole pair in the material. This quantity defines wavelength ranges for single- and multi-photon absorption, which will be discussed later in this section. The indirect type of the energy gap prevents radiative recombination of electron-hole pairs in c-Si. Intrinsic carrier concentration (N_i) can be used for an estimation of the lowest possible optical loss in silicon. Drift mobility of electrons (μ_e) and holes (μ_h) are used to calculate the carrier transport dependence on the applied electric field. Saturation velocity (v_{sat}) determines the fastest drift speed of charge carriers in the presence of the high electric field [24]. Excessive electric field applied to the silicon material can result in a high current flowing through the material (break-

1.1. RELEVANT PROPERTIES OF SILICON MATERIAL

Property	Value	Unit
Dielectric constant ε_{Si}	11.9	-
Energy gap E_g	1.12	eV
Energy gap type	indirect	-
Intrinsic carriers concentration N_i	9.65×10^9	cm^{-3}
Drift mobility of electrons μ_e	1450	$cm^2/(V \cdot cm)$
Drift mobility of holes μ_h	500	$cm^2/(V \cdot cm)$
Saturation velocity v_{sat}	1×10^7	cm/s
Breakdown field \mathcal{E}_{BD}	$2.5 - 8.5 \times 10^5$	V/cm
Minority carrier lifetime	$\sim 1 \times 10^{-3}$	s
Index of refraction n_{Si} *	3.47	-
Kerr coefficient n_2 *	$2.4 - 14.5 \times 10^{-18}$	m^2/W
Two photon absorption coefficient β_{TPA} *	$0.4 - 0.9 \times 10^{-11}$	m/W
Material dispersion coefficient D_{Si} *	-0.875	ps/(nm · m)
Optical intensity damage threshold I_{damage} *	1 – 4	GW/cm ²

Note: All properties at room temperature; * Values for $\lambda=1550$ nm

Table 1.2: Selected properties of crystalline silicon material [11, 16–20, 24, 25].

down). In the extreme case it can lead to the damage of the material. Another reason for the material destruction can be excessive light intensity. The limit is given by the optical intensity damage threshold (I_{damage}) [25]. Minority carrier lifetime represents the lifetime of carriers in the bulk Si without an applied electric field. Index of refraction n_{Si} represents a real part of Si refractive index at 1550 nm wavelength. Material dispersion (D_{Si}) represents the group velocity dispersion in the bulk silicon material. The real part of the nonlinear refractive index n_2 , known as well as Kerr coefficient, tells how much the refractive index of the medium changes with the optical intensity of the propagating light. Similarly, the β_{TPA} informs about the change in the optical loss with the change of intensity of the light passing through the bulk material.

1.2 Propagation of light wave in silicon

Propagation of light in dielectrics is in general described by Maxwell's equations. Considering a homogeneous medium and an electromagnetic wave propagating in it, the Maxwell's equations can be used to derive the wave equation [1,26]:

$$\nabla \times \nabla \times \mathbf{E} + \frac{1}{c^2} \frac{\partial^2 \mathbf{E}}{\partial t^2} = -\mu_0 \frac{\partial^2 \mathbf{P}}{\partial t^2} \quad (1.1)$$

where \mathbf{E} is the electric field, \mathbf{P} is the electric polarization, μ_0 is the vacuum permeability and c represent the speed of light in vacuum.

1.2.1 Electrical susceptibility and polarization

The theoretical analysis of an interaction of light with the crystalline silicon has already been thoroughly performed in [26–29]. The electromagnetic wave propagating through the material causes the displacement of the bound electrical charges \mathbf{D} , proportional to the electric field $\mathbf{E}(\mathbf{r}, t)$ and the electric polarization of the medium \mathbf{P} [27,30]:

$$\mathbf{D} = \varepsilon_0 \varepsilon_{Si} \mathbf{E} = \varepsilon_0 (1 + \chi) \mathbf{E} \equiv \mathbf{P} + \varepsilon_0 \mathbf{E} \quad (1.2)$$

with vacuum permittivity ε_0 , relative silicon permittivity ε_{Si} and electric field \mathbf{E} . The electric polarization $\mathbf{P}(\mathbf{r}, t)$, induced by the electric field, where \mathbf{r} and t are the position and the time respectively. The electric polarization \mathbf{P} can be generally expressed by the power series of the electric field [27,28]:

$$\mathbf{P} = \mathbf{D} - \varepsilon_0 \mathbf{E} = \varepsilon_0 (\chi^{(1)} : \mathbf{E} + \chi^{(2)} : \mathbf{E}\mathbf{E} + \chi^{(3)} : \mathbf{E}\mathbf{E}\mathbf{E} + \dots) \quad (1.3)$$

with the i th-order susceptibility $\chi^{(i)}$ expressed by $(i+1)$ th-rank tensor and the electric field $\mathbf{E}(\mathbf{r}, t)$. From the equation (1.3), the two components of the polarization, the linear \mathbf{P}_L and the nonlinear \mathbf{P}_{NL} [27,28] can be extracted:

$$\mathbf{P}_L = \varepsilon_0 \chi^{(1)} : \mathbf{E} \quad (1.4)$$

$$\mathbf{P}_{NL} = \varepsilon_0 \left(\chi^{(2)} : \mathbf{E}\mathbf{E} + \chi^{(3)} : \mathbf{E}\mathbf{E}\mathbf{E} + \dots \right) \quad (1.5)$$

The linear part of the susceptibility $\chi^{(1)}$, which in general is complex, governs effects such as dispersion and linear absorption or amplification. The linear complex refractive index $n_1 = n_{1real} + in_{1imag}$ is related to first order susceptibility by [31, 32]:

$$n_1^2 = 1 + (\chi^{(1)}) \quad (1.6)$$

and thus

$$n_{1real}^2 - n_{1imag}^2 = 1 + \text{Re}(\chi^{(1)}) \quad (1.7)$$

$$2n_{1imag}n_{1real} = \text{Im}(\chi^{(1)}) \quad (1.8)$$

Silicon is an anisotropic and dispersive material and hence the $\chi^{(1)}$ is a tensor, where each component is the function of a wavelength. Additionally, silicon is a centrosymmetric material, and thus the second order susceptibility vanishes ($\chi^{(2)} \equiv 0$) [27]. The lowest order nonlinearity in Si becomes then the third order nonlinearity. Therefore, the nonlinear polarization can be defined as follows:

$$\mathbf{P}_{NL} \approx \varepsilon_0 \chi^{(3)} \mathbf{E}^3 \quad (1.9)$$

The assumptions of the following calculations are set below (as in [27]). Firstly, only the Kerr effect and the TPA contribution to the nonlinear polarization is taken into account. Moreover, it is considered that the light is monochromatic and linearly polarized. Thus isotropic approximation can be used. The Kerr and TPA effects have a response time of tens of femtoseconds, providing effectively instantaneous response to electric field variation. These effects are commonly described by a nonlinear refractive index n_2 and two photon absorption coefficient β_{TPA} , that are related to nonlinear susceptibility $\chi^{(3)}$ [27]:

$$n_2 = \frac{3}{4\varepsilon_0 c n_{1real}^2} \text{Re}(\chi_{eff}^{(3)}) \quad (1.10)$$

$$\beta_{TPA} = \frac{3\omega}{2\varepsilon_0 c^2 n_{1real}^2} \text{Im}(\chi_{eff}^{(3)}) \quad (1.11)$$

where the $\chi_{eff}^{(3)}$ is given, for the crystal orientations, which are relevant for the research project $\langle 100 \rangle$, $\langle 110 \rangle$ and $\langle 111 \rangle$ by [27, 30]:

$$\chi_{eff}^{(3)\langle 100 \rangle} = \chi_{1111}^{(3)} \quad (1.12)$$

$$\chi_{eff}^{(3)\langle 110 \rangle} = \frac{1}{2}(\chi_{1111}^{(3)} + 3\chi_{1122}^{(3)}) \quad (1.13)$$

$$\chi_{eff}^{(3)\langle 111 \rangle} = \frac{1}{3}(\chi_{1111}^{(3)} + 6\chi_{1122}^{(3)}) \quad (1.14)$$

Lin et al. in [30], proved experimentally that proportionality $\chi_{1111}^{(3)} = 2.36\chi_{1122}^{(3)}$ occurs in the range of wavelengths from 1.2 to 2.4 μm . This leads to simplified form of the formulas (1.13) and (1.14):

$$\chi_{eff}^{(3)\langle 110 \rangle} = 1.1356\chi_{1111}^{(3)} \quad (1.15)$$

$$\chi_{eff}^{(3)\langle 111 \rangle} = 1.1808\chi_{1111}^{(3)} \quad (1.16)$$

The formulas (1.15) and (1.16) suggest that the preferred direction for the best nonlinear optical Kerr interaction would be $\langle 111 \rangle$. In practice, however, the commonly available SOI substrates are perpendicular to the crystal direction $\langle 001 \rangle$ and the waveguiding structures are fabricated mostly along the crystal direction $\langle 110 \rangle$. Orientation of the waveguide in respect to the crystal directions is shown in figure 2.5).

1.2.2 Propagation of light in silicon waveguide

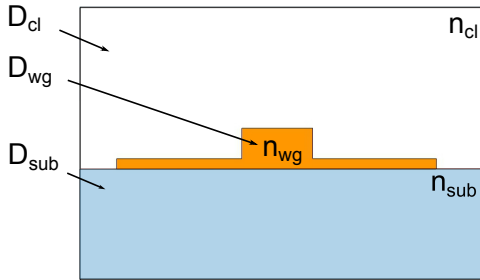


Figure 1.1: Silicon nano-rib waveguide cross-section used in optical simulations

To enhance the nonlinear optical effect, it is necessary to confine the light on the small cross-section. The cross-section concerned is depicted in figure 1.1 with D_{cl} , D_{sub} , D_{wg} being areas of the cladding, the substrate (here

it is just a layer under the waveguide) and the waveguide respectively. The total area D_{tot} contains all these areas. The materials have the refractive indices n_{cl} , n_{wg} and n_{sub} correspondingly. For the sake of further simplification in calculations the change in \mathbf{P} due to the propagating wave is treated as a small perturbation. Moreover, we assume, that the linearly polarized, quasi-monochromatic optical field maintains its polarization during propagation along the medium (along the z direction). Under these conditions, the optical field can be separated in the transverse component and the longitudinal components. Then it can be decomposed in the slowly varying envelope and the fast oscillating term at the frequency ω_0 [1, 26]:

$$\mathbf{E} = \hat{x} \mathcal{F}_E(x, y, t) A(z, t) e^{i(\beta(\omega_0)z - \omega_0 t)} \quad (1.17)$$

where \hat{x} is a unity polarization vector, $\mathcal{F}_E(x, y, t)$ is a vectorial electric transverse field distribution of the waveguide mode, $A(z, t)$ is the slowly varying amplitude, and $\beta(\omega_0)$ is a mode propagation constant dependent on the frequency ω_0 . The slowly varying amplitude is defined so that $|A(z, t)|^2$ is the average optical power. Similarly the magnetic field can be expressed as follows [33]:

$$\mathbf{H} = \hat{y} \mathcal{F}_H(x, y, t) A(z, t) e^{i(\beta(\omega_0)z - \omega_0 t)}. \quad (1.18)$$

where $\mathcal{F}_H(x, y, t)$ is a vectorial magnetic field distribution in the transverse plane of the waveguide. The functions $\mathcal{F}_E(x, y, t)$ and $\mathcal{F}_H(x, y, t)$ were calculated numerically with the full- vector mode solver developed by Fallahkhair et al. in Matlab environment and described in [34]. Results of the calculations are presented in the part considering the design of the structure.

As the susceptibility χ is a function of ω , the refractive index $n_{1,real}$ (or its equivalent n_{eff} in media with the limited transverse dimensions) and β depend on the optical frequency. Following the references [1, 27] the dispersion in the waveguide can be accounted for by the Taylor series expansion of the β around the center frequency ω_0 as follows:

$$\beta(\omega) = n_{1,real} \frac{\omega}{c} = \beta_0 + \beta_1(\omega - \omega_0) + \frac{1}{2} \beta_2(\omega - \omega_0)^2 + \dots \quad (1.19)$$

where:

$$\beta_m = \left(\frac{d^m \beta}{d\omega^m} \right)_{\omega=\omega_0} \quad (m = 1, 2, \dots) \quad (1.20)$$

the β_1 and β_2 are by definition expressed as follows [1]:

$$\beta_1 = \frac{1}{v_g} = \frac{n_g}{c} = \frac{1}{c} \left(n_{1real} + \omega \frac{dn_{1real}}{d\omega} \right), \quad (1.21)$$

$$\beta_2 = \frac{1}{c} \left(2 \frac{dn_{1real}}{d\omega} + \omega \frac{d^2 n_{1real}}{d\omega^2} \right) \quad (1.22)$$

where v_g and n_g are the group velocity and the group index respectively. Physically v_g represents the velocity of the optical pulse propagation while β_2 is a group velocity dispersion responsible for the pulse broadening. For convenient comparison with the commonly used terms in fiber optics, further in the thesis, the dispersion coefficient will be defined as in [1]:

$$D = \frac{d\beta_1}{d\lambda} = -\frac{2\pi c}{\lambda^2} \beta_2 = -\frac{\lambda}{c} \frac{d^2 n_{1real}}{d\lambda^2} \quad (1.23)$$

1.2.3 Nonlinear Schrödinger equation (NLSE) and nonlinear coefficient

In order to investigate the change of the amplitude $A(z, t)$ along the waveguide, the following Nonlinear Schrödinger Equation (NLSE) can be derived from the wave equation (1.1) [26]:

$$\begin{aligned} \frac{\partial A}{\partial z} = & -\frac{\alpha_{lin}}{2} A + \left(\sum_{n=1}^N (-i)^{(n+1)} \frac{\beta_n}{n!} \frac{\partial^n}{\partial t^n} \right) A + i\gamma |A|^2 A + ik_0 \Delta n_{FCD} A + \\ & -\frac{\Delta \alpha_{FCA}}{2} A - \frac{\beta_{TPA}}{2A_{eff}} |A|^2 A \end{aligned} \quad (1.24)$$

where β_n is n-th order dispersion term and γ is the nonlinear coefficient defined as:

$$\gamma = \frac{k_0 n_2}{A_{eff}} \quad (1.25)$$

the $k_0 = \omega/c$ is the wave number, Δn_{FCD} and $\Delta \alpha_{FCA}$ are the change of the refractive index and the excess loss due to the presence of the free carriers (section 1.2.4). The effective area (A_{eff}) is described more precisely later in the thesis (section 1.2.5). Here the CW operation is considered, away from the zero group velocity dispersion wavelength. Additionally the frame of reference moving at the the group velocity is used as in [1]:

$$\tau \equiv t - \beta_1 z. \quad (1.26)$$

Hence the equation (1.24) can be simplified as follows:

$$\begin{aligned} \frac{\partial A}{\partial z} = & -\frac{\alpha_{lin}}{2} A - i \frac{\beta_2}{2} \frac{\partial^2 A}{\partial t^2} + i \gamma |A|^2 A + \frac{n_{1real} i k_0 \Delta n_{FCD}}{n_{eff real}} A + \\ & - \frac{n_{1real} \Delta \alpha_{FCA}}{2 n_{eff real}} A - \frac{\beta_{TPA}}{2 A_{eff}} |A|^2 A \end{aligned} \quad (1.27)$$

where $n_{eff real}$ represents a real part of a effective refractive index of the waveguide.

1.2.4 Absorption and dispersion from free carriers and generation of free carriers by two photon absorption

The free electrons and holes with densities N_e and N_h (both represented in cm^{-3}), respectively, cause the change in the loss and refractive index. Considering wavelengths of around 1550 nm the loss change $\Delta \alpha_{FCA}$ (given in cm^{-1}) and the refractive index change Δn_{FCD} can be calculated according to the empirical formulas [27,29,35]:

$$\Delta n_{FCD} = - \left(8.8 \cdot 10^{-4} N_e + 8.5 \cdot N_h^{0.8} \right) \times 10^{-18} \quad (1.28)$$

$$\Delta \alpha_{FCA} = (8.5 \cdot N_e + 6.0 \cdot N_h) \times 10^{-18} \quad (1.29)$$

In the TPA process, two photons simultaneously absorbed by silicon create a pair of free carriers. The number of photons taking part in this interaction is proportional to the square of power $P^2 = |A|^4$ and the probability of TPA is governed by β_{TPA} such that the average free carrier generation [36, 37]

$$G_{TPA} \left[\frac{\text{cm}^3}{\text{s}} \right] = \frac{\beta_{TPA}}{2\hbar\omega A_{\text{eff}}^2} |A|^4 \quad (1.30)$$

Moreover, it is assumed that the densities of electrons and holes generated by TPA are equal ($N_e = N_h = N$). Furthermore the recombination of free carriers is governed by an effective carrier lifetime τ_{eff} (Eq. 1.31). This quantity is defined as the time necessary for the free carriers concentration N (in cm^{-3}) to decrease by $1/e$ [38]. Then the steady state free carriers density ($dN/dt = 0$) can be expressed along the propagation direction as $N(z) = G_{TPA} \cdot \tau_{\text{eff}}$. In order to calculate the loss resulting from the TPA induced excess FCA in CW operation, the corresponding loss coefficient is taken:

$$\Delta\alpha_{FCA} [\text{cm}^{-1}] = (8.5 \cdot N + 6.0 \cdot N) \times 10^{-18} = \sigma_{FCA} \cdot N = \sigma_{FCA} G_{TPA} \tau_{\text{eff}} \quad (1.31)$$

with

$$\sigma_{FCA} [\text{cm}^2] = 1.45 \times 10^{-17} \cdot (\omega_r/\omega)^2 \quad (1.32)$$

Accordingly the influence of electrons and holes on the refractive index change was evaluated. Nevertheless, it was assumed that the impact of the holes on the refractive index change Δn_{FCD} is 5 times the influence of electrons, such that [29]:

$$\Delta n_{FCD} = - \left(6 \cdot 8.8 \cdot 10^{-4} N \right) \times 10^{-18} = \sigma_{FCD} \times N = \sigma_{FCD} G_{TPA} \tau_{\text{eff}} \quad (1.33)$$

with

$$\sigma_{FCD} [\text{cm}^3] = -5.3 \times 10^{-21} \cdot (\omega_r/\omega)^2 \quad (1.34)$$

1.2.5 Effective area

In this thesis only the waveguide nonlinearity is considered, which is determined by properties of c-Si material. The nonlinearity of the surrounding material was neglected as it is two orders of magnitude smaller and the most of the light travels in the waveguide. In the optical calculations performed in the thesis the nonlinear coefficient γ was applied as in the equation (1.25). To calculate γ the effective area parameter A_{eff} must be determined. The effective area shall be understood as the relation of the

power transported in the waveguide cross-section to the effective intensity. The effective intensity is by definition the intensity of the plane wave propagating in the bulk homogeneous medium with the optical properties of the waveguide material [33]. Assuming the orthogonality of the transverse mode fields the effective area can be defined as follows [33]:

$$A_{\text{eff}} = \frac{c^2 \mu_0^2}{n_{\text{Si}}^2} \frac{\left| \iint_{D_{\text{tot}}} \text{Re} \{ \mathcal{F}_E(x, y) \times \mathcal{F}_H(x, y)^* \} \cdot \mathbf{e}_z \, dx dy \right|^2}{\iint_{D_{\text{wg}}} |\mathcal{F}_E(x, y)|^4 \, dx dy} \quad (1.35)$$

where the $\mathcal{F}_E(x, y)$ and $\mathcal{F}_H(x, y)$ are the vectorial electric and magnetic mode profiles respectively, as given in formulas (1.17) and (1.18).

1.2.6 Self phase modulation

The optical wave, propagating through the medium, causes a change in the index of refraction proportional to its power P and the Kerr coefficient. However, for the high powers the detrimental influence of TPA gains importance. Therefore, by neglecting the influence of the free carriers Δn_{FCD} , $\Delta \alpha_{\text{FCA}}$ and the dispersion β_2 the equation (1.27) is simplified to [39]:

$$\frac{\partial A}{\partial z} = -\frac{\alpha_{\text{lin}}}{2} A + i\gamma |A|^2 A - \frac{\beta_{\text{TPA}}}{2A_{\text{eff}}} |A|^2 A \quad (1.36)$$

where $|A|^2 = P$. Due to the Self Phase Modulation (SPM) the output power $P(L_{\text{wg}})$ and the nonlinear phase shift $\phi_{(\text{SPM})}(L_{\text{wg}})$ take the form as in the equations below [40, 41]:

$$\begin{aligned} P(L_{\text{wg}}) &= \frac{P(0) \cdot e^{-\alpha_{\text{lin}} L_{\text{wg}}}}{1 + \frac{\beta_{\text{TPA}}}{A_{\text{eff}}} P(0) L_{\text{eff}}} \\ \phi_{(\text{SPM})}(L_{\text{wg}}) &= \frac{\gamma A_{\text{eff}}}{\beta_{\text{TPA}}} \ln \left(1 + \frac{\beta_{\text{TPA}}}{A_{\text{eff}}} P(0) L_{\text{eff}} \right) \end{aligned} \quad (1.37)$$

The effective length is the length of the waveguide on which the linear loss of the pump can be considered negligible:

$$L_{\text{eff}} = \frac{1 - e^{-\alpha_{\text{lin}} L_{\text{wg}}}}{\alpha_{\text{lin}}} \quad (1.38)$$

1.2.7 Cross phase modulation

When the two optical waves, with amplitudes A_p , A_s , propagate in the waveguide with Kerr nonlinearity the effect of the Cross Phase Modulation (XPM) can be observed. If $A_p \gg A_s$, the contribution of the weak wave amplitude A_s to the following effects: SPM, the XPM and the free carriers generation, can be ignored. The propagation of the stronger wave is described as in equation (1.36), and the evolution of the A_s is [40]:

$$\begin{aligned}\frac{\partial A_p}{\partial z} &= -\frac{\alpha_{lin}}{2} A_p + i\gamma |A_p|^2 A_p - \frac{\beta_{TPA}}{2A_{eff}} |A_s|^2 A_p \\ (1.39) \\ \frac{\partial A_s}{\partial z} &= -\frac{\alpha_{lin}}{2} A_s + i\gamma |A_p|^2 A_s - \frac{\beta_{TPA}}{2A_{eff}} |A_p|^2 A_s\end{aligned}$$

Analogically, the analytic solution for power and phase terms was established [40]:

$$\begin{aligned}P_p(L_{wg}) &= \frac{P_p(0) \cdot e^{-\alpha_{lin} L_{wg}}}{1 + \frac{\beta_{TPA}}{A_{eff}} P_p(0) L_{eff}} \\ (1.40) \\ \phi_{p(XPM)}(L_{wg}) &= \frac{\gamma A_{eff}}{\beta_{TPA}} \ln \left(1 + \frac{\beta_{TPA}}{A_{eff}} P_p(0) L_{eff} \right) \\ P_s(L_{wg}) &= \frac{P_s(0) \cdot e^{-\alpha_{lin} L_{wg}}}{\left(1 + \frac{\beta_{TPA}}{A_{eff}} P_p(0) L_{eff} \right)^2} \\ (1.41) \\ \phi_{s(XPM)}(L_{wg}) &= 2 \frac{\gamma A_{eff}}{\beta_{TPA}} \ln \left(1 + \frac{\beta_{TPA}}{A_{eff}} P_p(0) L_{eff} \right)\end{aligned}$$

It is important to note that the power of the signal (P_s) is inverse proportional to the square of the input pump power $P_p(0)$. At the same time the phase shift of the signal $\phi_{s(XPM)}(L_{wg})$ due to XPM ($\phi_{s(XPM)}$) is doubled in comparison to the phase shift of the pump ($\phi_{p(XPM)}$).

1.2.8 Four-wave mixing

The availability of the very fast Kerr effect enables four wave mixing on the SOI platform and thus the possibility of a wavelength conversion,

parametric amplification and signal regeneration [42–45]. These nonlinear effects arises from the third order optical nonlinearity in silicon. Propagation of two strong optical pump waves and one signal wave through the Kerr medium introduces a nondegenerate FWM, by which a fourth wave called idler is created. The three input waves, generate nine new waves [26]. Nevertheless, only four waves are considered since the other eight are substantially weaker in the case of waveguides with normal dispersion. Therefore, the present (most general) analysis focuses only on the interaction of the four strongest waves as shown in figure 1.2(a). In addition, two degenerate variants of FWM are analyzed in this thesis. They are the pump degenerate variant (figure 1.2(b)) and the signal degenerate variant (figure 1.2(c)). In the first one a single pump wave induces the nonlinear polarization response of the medium thus creating conditions to convert the signal to the idler wave. The signal degenerate variant appears when two pump waves and the single signal in the middle are used, while the signal and the idler are at the same frequency.

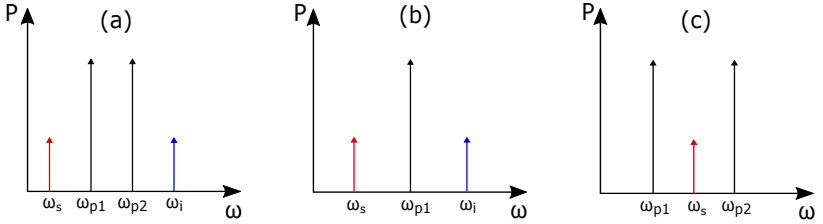


Figure 1.2: Four wave mixing scheme in variants: (a) nondegenerate, (b) pump degenerate, (c) signal degenerate

For the following analysis, it is assumed that [1,29,46]:

$$A = A_{p1} + A_{p2} + A_s + A_i \quad (1.42)$$

where the amplitude of the first strong pump wave is A_{p1} , the second strong pump wave is A_{p2} , the weak signal wave is A_s and the idler wave (converted signal wave) is A_i ($|A_s|, |A_i| < |A_{p1}|, |A_{p2}|$). Further, the equation (1.42) is inserted to the equation (1.27). Next the equation (1.27) is separated into a set of the coupled equations to describe the evolution of each of the four waves amplitudes over the waveguide length:

$$\begin{aligned} \frac{\partial A_{p1}}{\partial z} = & -\frac{\alpha_{lin}}{2} A_{p1} + (i\gamma_{p1} - \frac{\beta_{TPA}}{2A_{eff}}) \left(|A_{p1}|^2 + 2 \sum_{m=p2,s,i} |A_m|^2 \right) A_{p1} + \\ & + 2i\gamma_{p1} A_{p2}^* A_s A_i e^{i\Delta\beta z} - \left(ik_0 \Delta n_{FCD} + \frac{\Delta\alpha_{FCA}}{2} \right) A_{p1} \end{aligned} \quad (1.43)$$

$$\begin{aligned} \frac{\partial A_{p2}}{\partial z} = & -\frac{\alpha_{lin}}{2} A_{p2} + (i\gamma_{p2} - \frac{\beta_{TPA}}{2A_{eff}}) \left(|A_{p2}|^2 + 2 \sum_{m=p1,s,i} |A_m|^2 \right) A_{p2} + \\ & + 2i\gamma_{p2} A_{p1}^* A_s A_i e^{-i\Delta\beta z} - \left(ik_0 \Delta n_{FCD} + \frac{\Delta\alpha_{FCA}}{2} \right) A_{p2} \end{aligned} \quad (1.44)$$

$$\begin{aligned} \frac{\partial A_s}{\partial z} = & -\frac{\alpha_{lin}}{2} A_s + (i\gamma_s - \frac{\beta_{TPA}}{2A_{eff}}) \left(|A_s|^2 + 2 \sum_{m=p1,p2,i} |A_m|^2 \right) A_s + \\ & + 2i\gamma_s A_{p1} A_{p2} A_i^* e^{-i\Delta\beta z} - \left(ik_0 \Delta n_{FCD} + \frac{\Delta\alpha_{FCA}}{2} \right) A_s \end{aligned} \quad (1.45)$$

$$\begin{aligned} \frac{\partial A_i}{\partial z} = & -\frac{\alpha_{lin}}{2} A_i + (i\gamma_i - \frac{\beta_{TPA}}{2A_{eff}}) \left(|A_i|^2 + 2 \sum_{m=p1,p2,s} |A_m|^2 \right) A_i + \\ & + 2i\gamma_i A_{p1} A_{p2} A_s^* e^{-i\Delta\beta z} - \left(ik_0 \Delta n_{FCD} + \frac{\Delta\alpha_{FCA}}{2} \right) A_i \end{aligned} \quad (1.46)$$

In the general case of the FWM process in a silicon waveguide, all the waves contribute to the generation of the free carriers and thus to the increase of the loss coefficient $\Delta\alpha_{FCA}$. However, the contribution of the weak signal and the idler is neglected in the further calculations. The density of the free carriers generated by TPA process is then simplified to [36]:

$$N_{e,h} = \frac{\beta_{TPA} \tau_{eff}}{2h\nu A_{eff}^2} (P_{p1} + P_{p2})^2 \quad (1.47)$$

and allows to calculate $\Delta\alpha_{FCA}$ and Δn_{FCD} according to equations 1.29 and 1.28 respectively. The physics of FWM can be explained by the conditions: the energy conservation and the momentum conservation (phase-matching condition) [47]. For the FWM described by the equations (1.43-1.46) these conditions can be expressed by the equations below:

$$\omega_i = \omega_{p1} + \omega_{p2} - \omega_s \quad (1.48)$$

$$\Delta\beta = \beta_{p1} + \beta_{p2} - \beta_i - \beta_s = 0 \quad (1.49)$$

In section 3.3.6 the discussion will be limited to the pump degenerate version of FWM, where $\omega_{p1} = \omega_{p2} = \omega_p$, while the phase matching condition and the energy conservation condition are simplified to:

$$\Delta\beta = 2\beta_p - \beta_i - \beta_s = 0 \quad (1.50)$$

$$\Delta\omega = \omega_p - \omega_s = \omega_i - \omega_p \quad (1.51)$$

$$\omega_i = 2\omega_p - \omega_s \quad (1.52)$$

The SPM and XPM cause the nonlinear phase shift. In the case of the single strong pump this nonlinear phase shift must be taken into account and hence the phase matching condition (1.50) changes into [27]:

$$\Delta k_{nl} = 2\gamma P_p - \Delta\beta \quad (1.53)$$

where P_p is the power of the pump in the medium and the linear phase difference is:

$$\Delta\beta = -\beta_2(\Delta\omega)^2 - \frac{1}{12}\beta_4(\Delta\omega)^4 \quad (1.54)$$

where n_{eff} is the effective refractive index. Moreover, β_2 and β_4 are calculated at the pump wavelength. Phase matching, required by momentum conservation in equation (1.53) can be provided by the waveguide dispersion engineering. Silicon material dispersion needs compensation by the proper waveguide dimensions design to obtain the broadband operation and gain. As presented by Osgood et al. in [27], neglecting TPA, FCA and α_{lin} , the formula for the conversion efficiency defined as a ratio between output idler power $P_i(L_{wg})$ to input signal $P_s(0)$ becomes:

$$\eta_{0L} = \frac{P_i(L_{wg})}{P_s(0)} = \left[\frac{\gamma P_p}{g} \sinh(gL_{wg}) \right]^2, \quad (1.55)$$

where

$$g = \sqrt{\gamma P_p \Delta\beta - \left(\frac{\Delta\beta}{2}\right)^2} \quad (1.56)$$

represents the parametric gain and L_{wg} is the length of interaction in this ideal case. If $\Delta\beta = 2\gamma P_p$ then equation (1.55) is reduced to:

$$\eta_{0L,max} = \sinh^2(\gamma P_p L_{wg}). \quad (1.57)$$

In [27, 48] authors used the definition of wavelength conversion bandwidth when $|\Delta k_{nl} L_{wg}| < \pi$. Under the assumption of the small gain limit when $2\gamma P_p L_{wg} \ll \pi$, the wavelength conversion bandwidth can be expressed as:

$$BW_{FWM} \approx \sqrt{\frac{4\pi}{\beta_2 L_{wg}}} \quad (1.58)$$

where β_2 is the group velocity dispersion coefficient. These formulas give a good estimation of the maximum possible FWM wavelength conversion efficiency in the silicon waveguide.

1.2.9 Four wave mixing simulation model

The four wave mixing in the silicon waveguide is approximated by the first order nonlinear Schrödinger equation (described in section 1.2.3). It provides a good agreement to the measurement results available in the literature [27, 28, 42, 43]. For the FWM simulations, the model introduced by Jazayerifar and Dziallas et al. in [28, 46] is used. The method matches well with other models developed by the research groups working in the field [27, 49–51]. The nonlinear Schrödinger equation (NLSE) (equation (1.27)) with the sum amplitude from the equation (1.42) is solved numerically using the Fourier split step method [1, 26, 28]. This methods relies on the assumption that the linear and nonlinear effects can be treated separately, if sufficiently small propagation distance is taken into account. Therefore, dividing the waveguide in small segments of the length Δz , the amplitude evolution can be approximated by:

$$A(z + \Delta z, t) = A(z, t) \left(e^{\frac{1}{2}\Delta z \hat{D}} e^{\Delta z \hat{N}} e^{\frac{1}{2}\Delta z \hat{D}} \right) \quad (1.59)$$

where the differential operators are defined by:

$$\hat{D} = -i\frac{\beta_2}{2} \frac{\partial^2}{\partial t^2} - \frac{\alpha_{lin}}{2} \quad (1.60)$$

$$\hat{N} = -i\gamma|A|^2 - \frac{\beta_{TPA}}{2A_{eff}}|A|^2 - ik_0\Delta n_{FCD} - \frac{\Delta\alpha_{FCA}}{2} \quad (1.61)$$

where β_2 is a group velocity dispersion defined in equation (1.22), α_{lin} is linear loss coefficient of the waveguide. The γ is nonlinear coefficient defined as in equation (1.25), β_{TPA} is TPA coefficient introduced in equation (1.11). The terms $\Delta\alpha_{FCA}$ and Δn_{FCD} were calculated with the formulas (1.31) and (1.33). The numerical simulations were performed in the Matlab environment. The steps using Fast Fourier Transform (fft) and Inverse Fast Fourier Transform (ifft) within one Δz step were realized in the following order [28]:

$$A\left(z + \frac{1}{2}\Delta z, t\right) = \text{ifft} \left\{ \text{fft} \left(A(z, t) \right) \cdot e^{\left(i\frac{\beta_2}{2}\omega^2 - \frac{1}{2}\alpha_{lin} \right) \cdot \frac{1}{2}\Delta z} \right\} \quad (1.62)$$

$$A\left(z + \frac{1}{2}\Delta z, t\right) = A\left(z + \frac{1}{2}\Delta z, t\right) \cdot e^{\left(-i\gamma|A|^2 - \frac{1}{2}\alpha_{TPA} - ik_0\Delta n_{FCD} - \frac{1}{2}\Delta\alpha_{FCA} \right)} \quad (1.63)$$

$$A(z + \Delta z, t) = \text{ifft} \left\{ \text{fft} \left(A\left(z + \frac{1}{2}\Delta z, t\right) \right) \cdot e^{\left(i\frac{\beta_2}{2}\omega^2 - \frac{1}{2}\alpha_{lin} \right) \cdot \frac{1}{2}\Delta z} \right\} \quad (1.64)$$

where the ω is a vector consisting of all the frequencies taken into account for the nonlinear propagation simulations.

The graphical interpretation of the implementation of the symmetric split step Fourier method is presented in figure 1.3. The symmetric split step Fourier transform method was used to design structures as well as for better understanding of the obtained measurement results and finally to optimize waveguide structures.

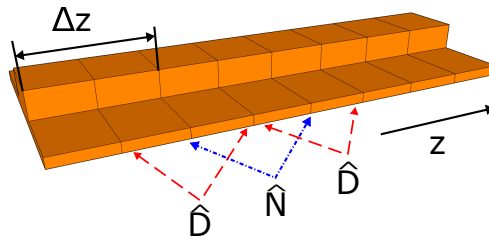


Figure 1.3: Visual representation for the sequence of calculations performed within the symmetric split step Fourier transform method

2

Numerical simulations of the SOI waveguide for CW four wave mixing

Designing samples for the nonlinear interaction will be presented in this chapter including different aspects of the structures optimization. This chapter contains detailed information about the models, parameters and properties of the materials used in the design process. It will start with the optical properties of the applied materials, which were necessary for the sample fabrication. Each property will be explained using an appropriate model. Then the linear optical properties of the waveguide such as a linear loss and dispersion shall be introduced. The further analysis will contain placing doped regions aside the waveguide and its consequence for the waveguide loss. Later results of the power dependent loss simulations will be presented. Moreover, the possibility of increasing recombination rate e.g. shortening the effective free carriers lifetime (τ_{eff}) will be analyzed.

2.1 Optical properties approximation of applied materials

2.1.1 Linear absorption of bulk Si

The key material feature, as regards the propagation of an optical signal is certainly the linear absorption (known as well as a single-photon absorption [2]). The linear optical loss of c-Si has been expected to be low for the optical wavelengths longer than 1200 nm due to its relatively high, indirect energy gap $E_g = 1.12$ eV [35, 52]. Indeed in 2013 optical absorption as low as $2 \cdot 10^{-5}$ dB/cm was measured at 1550 nm wavelength by Degallaix

CHAPTER 2. NUMERICAL SIMULATIONS OF THE SOI WAVEGUIDE FOR CW FOUR WAVE MIXING

et al. in a high resistivity c-Si substrate (impurity concentration $N = 10^{11} \text{ cm}^{-3}$) [53]. The free carriers absorption (FCA) mechanism, researched by Soref and Bennet in the highly doped Si substrates [35], was then confirmed for the samples with the low impurity concentration as well. The formula (see equation (1.29)) developed in [35] allows to estimate the excess absorption coefficient resulting from the free carriers, knowing the impurity concentration N_A (for acceptors) and/or N_D (for donors). From the

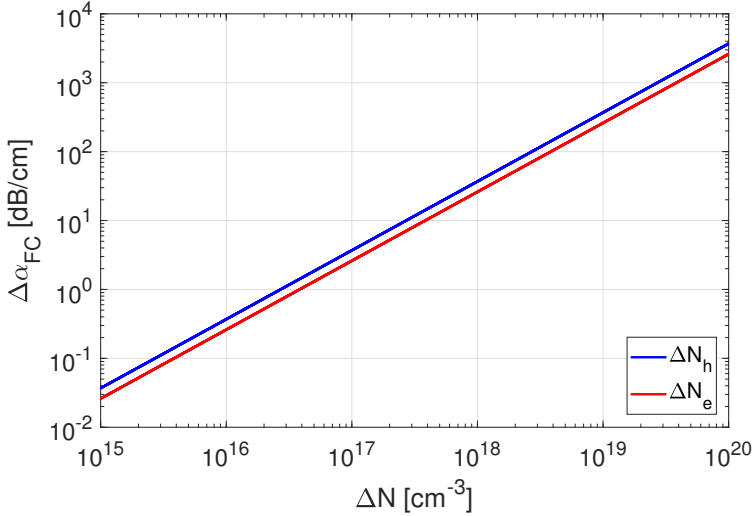


Figure 2.1: Loss coefficient from free carriers at 1550 nm wavelength, assuming uniform carriers distribution

formula (1.29) one can calculate the free carriers absorption in SOI substrate knowing the impurity doping concentration corresponding to the free carriers concentration N_e and N_h . Considering commonly used SOI substrate with the boron (B) doped top silicon layer, where the impurity concentration is $N_A = 10^{15} \text{ cm}^{-3}$, one shall take into account excess material optical loss from FCA of:

$$\alpha_{\text{FCA}_{dB}} \left[\frac{dB}{cm} \right] = 4.34 \cdot (8.5 \cdot 10^{-18} \text{ cm}^2 \cdot 9.65 \cdot 10^9 \text{ cm}^{-3} + 6 \cdot 10^{-18} \text{ cm}^2 \cdot 10^{15} \text{ cm}^{-3}) = 0.026 \left[\frac{dB}{cm} \right] \quad (2.1)$$

This shows that the pure silicon loss is about three orders of magnitude lower than the excess loss introduced by the impurity. Figure 2.1 depicts the relation between the carrier concentration (impurity concentration) and the excess loss. The results obtained in this short analysis and cited references suggest, that the major fraction of the optical loss in bulk Si can be attributed to the free carriers coming from impurities.

2.1.2 Two photon absorption and free carriers absorption induced by two-photon absorption

Exposing silicon Si to the high intensity light with $hc/E_g < \lambda < hc/E_g$ enables an effect known as two photon absorption TPA. Two photons, that in sum have energy higher then E_g , are absorbed simultaneously by the semiconductor material and create a free electron-hole pair. This effect is orders of magnitude weaker then the linear absorption and therefore becomes pronounced for the high light intensities (e.g. in Si over $0.1 \cdot 10^9 W/cm^2$ at $\lambda = 1550nm$). The loss due to TPA and TPA induced FCA was calculated from the corresponding formulas defined in the section 1.2.4. The value of $\beta_{TPA} = 0.56 \cdot 10^{-9} cm/W$ was obtained from the measurement reported later in the thesis in section 3.3.5.

2.1.3 Material dispersion of silicon, silicon nitride and silicon oxide

Simulation of the integrated, silicon based photonic structures requires taking into account dispersion of silicon and surrounding materials. In the following numerical calculations, we use the relation of the real part of the refractive index of Si versus wavelength λ given by the equation [27,54]:

$$n_{Si}(\lambda) = \sqrt{A + \frac{B_1}{\lambda^2} + \frac{B_2 \cdot \lambda^2}{\lambda^2 - \lambda_1^2}} \quad (2.2)$$

where $A = \varepsilon_{Si}(\lambda \rightarrow \infty) = 11.6858$, $\lambda_1 = 1.1071 \mu m$, $B_1 = 0.939816 \mu m^2$, $B_2 = 8.10461 \cdot 10^{-3}$. The blue curve in figure 2.2 shows this relation, while the red one depicts the chromatic dispersion coefficient (D) according to the formula (1.23) [55]:

Two other materials, used in the available technology for fabrication of the photonic integrated structures were silicon oxide (SiO_2) and silicon nitride

CHAPTER 2. NUMERICAL SIMULATIONS OF THE SOI WAVEGUIDE FOR CW FOUR WAVE MIXING

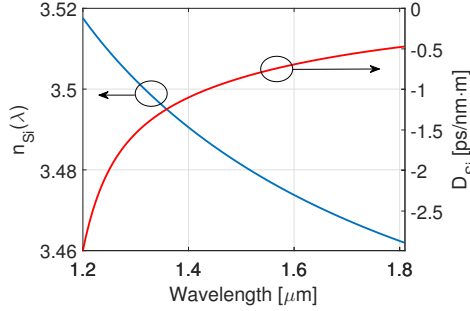


Figure 2.2: Refractive index n_{Si} and material dispersion coefficient of Si versus wavelength λ .

(Si_3N_4). Both these dielectrics influence the wave-guiding properties of the investigated structures. Figures 2.3 and 2.4 show the refractive indices and dispersion coefficients of these materials. The refractive index of SiO_2 was calculated with the Sellmeier formula published by Malitson et al. [56]:

$$n_{SiO_2}(\lambda) = \sqrt{A + \frac{B_1 \cdot \lambda^2}{\lambda^2 - \lambda_1^2} + \frac{B_2 \cdot \lambda^2}{\lambda^2 - \lambda_2^2} + \frac{B_3 \cdot \lambda^2}{\lambda^2 - \lambda_3^2}} \quad (2.3)$$

where $A = 1$, $B_1 = 0.6961663$, $B_2 = 0.4079426$, $B_3 = 0.8974794$, $\lambda_1 = 0.0684043 \mu m$, $\lambda_2 = 0.1162414 \mu m$, $\lambda_3 = 9.896161 \mu m$.

For the silicon nitride (Si_3N_4) the dependence of the real part of the refractive index $n_{Si_3N_4}$ on the wavelength was calculated with the formula provided by Levy in [57]:

$$n_{Si_3N_4}(\lambda) = \sqrt{A + \frac{B_1 \cdot \lambda^2}{\lambda^2 - \lambda_1^2} + \frac{B_2 \cdot \lambda^2}{\lambda^2 - \lambda_2^2} + \frac{B_3 \cdot \lambda^2}{\lambda^2 - \lambda_3^2} + \frac{B_4 \cdot \lambda^2}{\lambda^2 - \lambda_4^2}} \quad (2.4)$$

where $A = 2.3577$, $B_1 = 3.392$, $B_2 = -1.769$, $B_3 = 5 \cdot 10^{-5}$, $B_4 = 7.0599$, $\lambda_1 = 0.169 \mu m$, $\lambda_2 = 0.175 \mu m$, $\lambda_3 = 0.310 \mu m$, $\lambda_4 = 20.321 \mu m$.

In the table 2.1 below the coefficients for the above described approximations are summarized.

2.2. OPTICAL PROPERTIES OF SILICON NANO-RIB WAVEGUIDE WITH LATERAL P-I-N DIODE

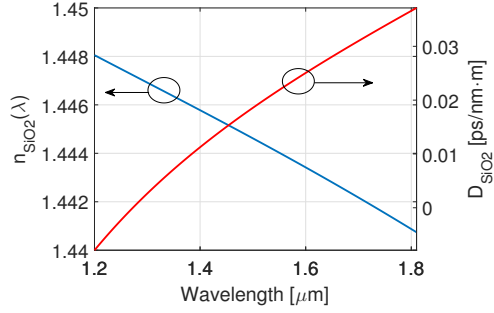


Figure 2.3: Refractive index n_{SiO_2} and material dispersion coefficient of SiO_2 versus wavelength λ .

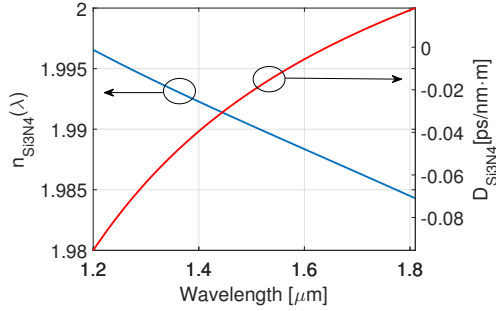


Figure 2.4: Refractive index $n_{\text{Si}_3\text{N}_4}$ and material dispersion coefficient $D_{\text{Si}_3\text{N}_4}$ of Si_3N_4 versus wavelength λ .

The values reported in this section are consistent with the results obtained in the ellipsometry measurements for the particular materials used during fabrication of the waveguides.

2.2 Optical properties of silicon nano-rib waveguide with lateral p-i-n diode

Several waveguide geometries were considered on the SOI platform with the aim to provide a high light confinement, and thus enhancing the op-

CHAPTER 2. NUMERICAL SIMULATIONS OF THE SOI WAVEGUIDE FOR CW FOUR WAVE MIXING

Model Coefficient	Si [27,54]	SiO ₂ [56]	Si ₃ N ₄ [57]
A	11.6858	1	2.3577
B_1	$0.939816 \mu\text{m}^2$	0.6961663	3.392
B_2	$8.10461 \cdot 10^{-3}$	0.4079426	-1.769
B_3	-	0.8974794	$5 \cdot 10^{-5}$
B_4	-	-	7.0599
λ_1	$1.1071 \mu\text{m}$	$0.0684043 \mu\text{m}$	$0.169 \mu\text{m}$
λ_2	-	$0.1162414 \mu\text{m}$	$0.175 \mu\text{m}$
λ_3	-	$9.896161 \mu\text{m}$	$0.310 \mu\text{m}$
λ_4	-	-	$20.321 \mu\text{m}$

Table 2.1: Coefficients used in the approximation of the materials' dispersion

tical Kerr effect [27, 33, 42, 43, 48, 58, 59]. Therefore, a sub-micron dimension stripe of silicon surrounded by low refractive index material like air or SiO₂ was used to guide the light to analyze the nonlinear optical effects [48, 60]. These experiments showed the detrimental influence of TPA and TPA induced FCA, apart from the enhancement in the nonlinear coefficient γ . To overcome the limitation due to the FCA the free carrier density in the wave-guiding area shall be suppressed. In order to fulfill the requirements of small A_{eff} and the low free carriers density it was decided to produce the sub-micron size nano-rib waveguide assisted by the lateral p-i-n diode [58].

2.2.1 Structure of the modeled waveguide

The commonly used SOI wafer consists of a silicon substrate with SiO₂ with a few micrometers thickness (typically from 1 to 3 μm) and a Si layer on the top (typically 220 nm thick). The waveguide is created by forming of a stripe pattern in the top silicon layer. Later it can be covered by another material. The considered structures were covered with both SiO₂ and Si₃N₄. Before the final choice of the dimensions of the waveguide for fabrication with a lateral p-i-n diode, different variants of a sub-micrometer single mode silicon rib waveguide were investigated.

Figure 2.5 depicts the general scheme of the waveguide considered for the evaluation. Next to the waveguide p- and n-doped regions were created. They provide connection of the bias voltage to induce an electric field in

2.2. OPTICAL PROPERTIES OF SILICON NANO-RIB WAVEGUIDE WITH LATERAL P-I-N DIODE

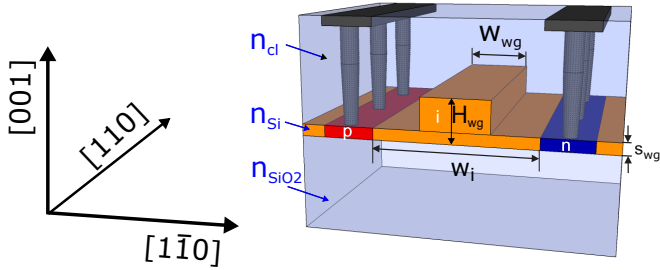


Figure 2.5: Silicon nano-rib waveguide with lateral p-i-n diode, schematic view showing cladding and metal contacts

the intrinsic region of the waveguide rib (marked with i). The doping regions need to be placed far enough from the waveguide not to contribute to the propagation loss but close enough to provide sufficient bias efficiency.

2.2.2 Mode of the silicon nano-rib waveguide

Using the values of the refractive indexes of Si, SiO₂ and Si₃N₄ (see 2.1.3), and setting the wavelength to $\lambda=1550$ nm, the mode profiles were calculated. For this purpose a full-vector finite difference mode solver is applied, as described by A.B. Fallahkhair and T.E. Murphy [34]. The mode profiles were calculated with the simple one material cladding (see 1.1) that was either air ($n_{air} = 1$), SiO₂ or Si₃N₄.

In figure 2.6 the strongest components of the resulting quasi-TE mode are depicted, where the major electric field component is parallel to the x direction. These field components profiles were used to determine the nonlinear effective area (A_{eff}) according to the equation (1.35). Due to the higher effective nonlinearity of the waveguide $\chi_{eff}^{(110)}$ (equation (1.15)) for the quasi-TE polarized wave, only the quasi-TE mode was further investigated in the present thesis. The mode profiles and the effective indexes were used to calculate the dispersion coefficients (D) and the nonlinear effective areas (A_{eff}) of different waveguides.

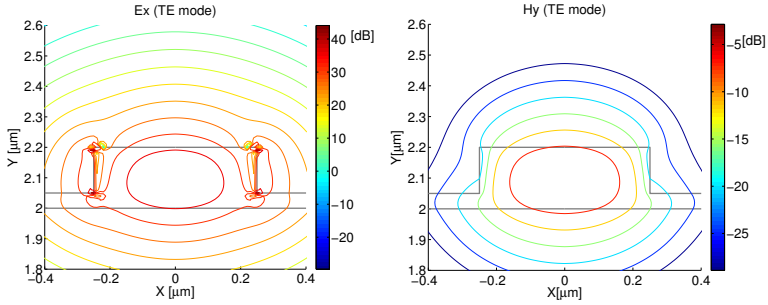


Figure 2.6: Results of the TE mode calculation for the quasi-TE mode in the silicon nano-rib waveguide with top and bottom SiO_2 cladding.

2.2.3 Dispersion in silicon nano-rib waveguides

The analysis of dispersion in various sub-micron nano-rib waveguides covers the C-band (1530-1565 nm) and the major part of the L-band (1565-1625 nm) of the fiber optic telecommunication spectrum. The optical dispersion of the waveguide results from its core material, shape and dimensions. The importance of the surrounding cladding material dispersion grows with the decrease in the waveguide dimensions. In the nano-rib waveguide also the slab region height plays an important role. The full-vector finite difference mode solver (see subsection 2.2.2), allowed to calculate the waveguide dispersion dependence on its dimensions and the covering cladding materials. The waveguide with an air cladding serves as a reference, giving the highest refractive index contrast and thus the highest confinement. Here neither the materials nor structures with $n_{\text{real}} < 1$ were considered. The dispersion change is shown by plotting dispersion coefficient (D) for different cases. The calculated dispersion may subtly differ from the absolute real values since they do not take into account a strain introduced by the cladding layers. However, the presented trend correlates well with the experiments of the dispersion in Si waveguides to be shown in the section 3.3.2.

The analysis of the Si nano-rib waveguide (figure 2.5) dispersion started with the air cladding ($n_{\text{air}} = 1$), examining the sole influence of the structure cross-section dimensions. At first, the effective indices n_{eff} for different wavelengths (λ) were calculated with the mode solver, including the models of the material dispersion presented in the section 2.1.3. Then

2.2. OPTICAL PROPERTIES OF SILICON NANO-RIB WAVEGUIDE WITH LATERAL P-I-N DIODE

using the equations (1.19)-(1.23), the values of β_1 , β_2 and D were determined. Figures 2.7-2.10 show the influence of the waveguide width (W_{wg}) on its dispersion. Keeping the height $H_{wg} = 220 \text{ nm}$ and the slab thickness $s_{wg} = 50 \text{ nm}$, even with the air top cladding, it can be observed that changing W_{wg} does not lead to anomalous dispersion ($D > 0 \text{ pm}/(\text{nm} \cdot \text{m})$). To obtain the dispersion coefficient $D(\lambda = 1550 \text{ nm}) \approx 0$ in the waveguide, with the $s_{wg} = 50 \text{ nm}$ and $H_{wg} = 220 \text{ nm}$, would require $W_{wg} = 550 \text{ nm}$. For the anomalous dispersion to occur, the waveguide height (H_{wg}) needs to increase (figure 2.11). The other of parameters that can be adjusted is the slab thickness (s_{wg}). Its impact on D is depicted in figure 2.12. In order to obtain the anomalous dispersion in the nano-rib waveguide, a certain balance between the waveguide slab and the rib height needs to be maintained. Examined variation suggests that, obtaining the anomalous dispersion around 1550 nm wavelength in the Si nano-rib waveguide with air cladding is possible for the ribs higher than 220 nm or for the slab thinner than 50 nm.

Next, a Si_3N_4 material is considered, as a top cladding of the waveguide. Depositing a layer of the silicon nitride pushes the dispersion further towards normal regime at the wavelengths around 1550 nm. This effect is depicted in figure 2.13. Although obtaining anomalous dispersion in Si nano-waveguide up to $H_{wg} = 400 \text{ nm}$ height is possible with Si_3N_4 cladding, as demonstrated by Osgood et al. in [27], it would require the slab height $s_{wg} \approx 0$. The latter is, however, inconvenient since the slab is needed as a sink for electrons and holes. Therefore, if the Si_3N_4 cladding is used in the production, it shall be removed from the guiding area. With a subtle modification of the fabrication process the Si_3N_4 layer can be substituted by silicon dioxide (SiO_2). The figures 2.14 visualize the result of the cladding change.

The dispersion coefficient shifted towards positive values for the waveguide width of 500 nm, rib heights over 300 nm and slab heights below 100 nm. The SiO_2 cladding allows more freedom in design of the waveguides for the optical nonlinear interaction.

From the analysis presented in this section it can be concluded that the covering material should have a refractive index as low as possible. In order to realize the active removal of electrons and holes from the nonlinear waveguide, the cladding is necessary. This aspect will be discussed later in the section 2.4. Since the SiO_2 cladding permits anomalous dispersion, and thus broadband operation, it shall be used instead of Si_3N_4 layer on

CHAPTER 2. NUMERICAL SIMULATIONS OF THE SOI WAVEGUIDE FOR CW FOUR WAVE MIXING

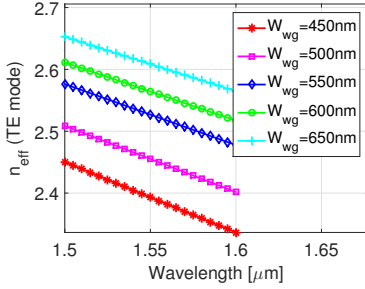


Figure 2.7: Effective index n_{eff} versus λ , (Air-cladded waveguide *)

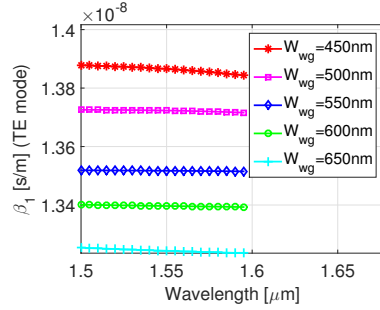


Figure 2.8: First order dispersion β_1 versus λ , (Air-cladded waveguide *)

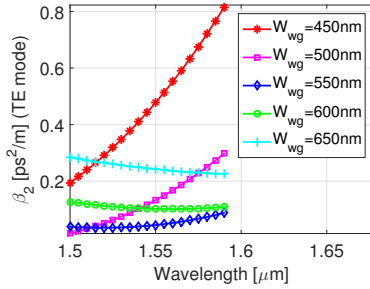


Figure 2.9: Second order dispersion β_2 versus λ , (Air-cladded waveguide *)

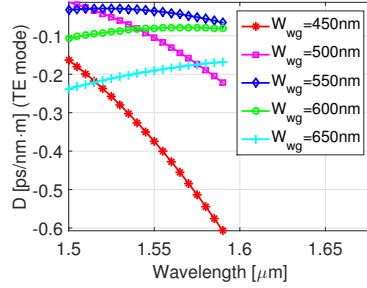


Figure 2.10: D versus λ , (Air-cladded waveguide *)

* quantities calculated for quasi TE-mode in the waveguide with dimensions $H_{\text{wg}} = 220 \text{ nm}$, $s_{\text{wg}} = 50 \text{ nm}$ and various W_{wg} .

the waveguide.

2.2.4 Linear loss sources in a nano-rib waveguide with lateral p-i-n diode

Linear and nonlinear absorption mechanisms in the bulk Si material was already discussed in subsections 1.2.4 and 2.1.1. However, in the real sub-

2.2. OPTICAL PROPERTIES OF SILICON NANO-RIB WAVEGUIDE WITH LATERAL P-I-N DIODE

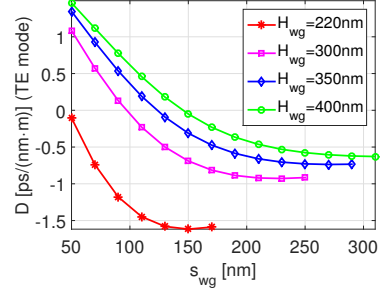
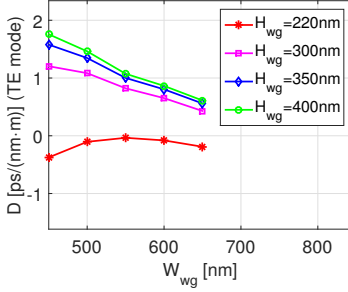


Figure 2.11: D versus W_{wg} for $s_{wg} = 50$ nm (Air-cladded waveguide *) Figure 2.12: D versus s_{wg} , for $W_{wg} = 500$ nm, (Air-cladded waveguide *)

* quantities calculated for quasi TE-mode in the waveguide at $\lambda = 1550$ nm and various H_{wg} .

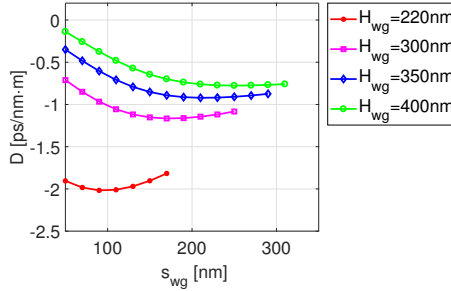


Figure 2.13: Quasi-TE mode dispersion coefficient at 1550 nm wavelength versus slab height for different waveguide rib heights and $W=500$ nm with Si_3N_4 cladding

micron waveguide as depicted in figure 2.5, the other sources of loss need to be taken into account as well. The loss can result from scattering centers introduced by material imperfection or ion implantation. Moreover, the fabrication process can introduce the surface roughness on the top and sidewalls of the rib waveguide. In the waveguide with a lateral p-i-n diode special attention needs to be given to the absorption coming from the doped regions placed on the side of the waveguide. Too close

CHAPTER 2. NUMERICAL SIMULATIONS OF THE SOI WAVEGUIDE FOR CW FOUR WAVE MIXING

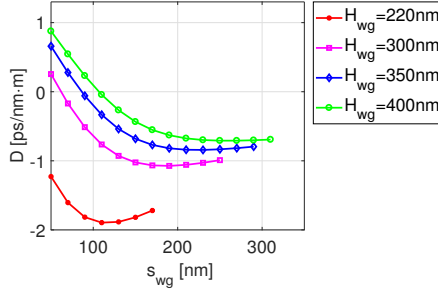


Figure 2.14: Quasi-TE mode dispersion coefficient D at 1550 nm wavelength versus slab height s for different H , and $W=500\text{nm}$ with SiO_2 cladding

placed doped regions overlap with the waveguide mode and thus lead to excessive absorption. To quantify this effect, the simulations with the commercially available JCMwave mode solver were performed by Benjamin Wohlfeil. The software was chosen due to higher flexibility and clarity in the definition of the custom waveguide structures than the one used in subsection 2.2.2. The slab thickness (s_{wg}), waveguide width (W_{wg}) and height (H_{wg}) were set to 50 nm, 500 nm and 220 nm respectively. The p- and n-doped regions separated by a distance w_i were placed symmetrically (figure 2.5) on each side of the waveguide. The separations w_i from 0.6 to 2.4 μm were analyzed for the equal doping concentrations ($N_e = N_h = N$) in the range from $3 \cdot 10^{17}$ to 10^{20} cm^{-3} . The calculations were performed for the wavelength $\lambda = 1550\text{nm}$. The free carrier loss in the doping regions was calculated as described in 2.1.1, and was used to determine the complex refractive indices of the doped regions. The latter were inserted in the structure definition. The values inserted into the JCM Wave software, allowed calculation of the complex effective refractive index (n_{eff}) of the waveguide with a given profile. The software used finite-element method to solve Maxwell's equations for the defined cross-section of the waveguide. The excess loss coefficient caused by both doping regions was extracted using the following relation:

$$\Delta\alpha_{pin} = \frac{4\pi}{\lambda} \cdot \text{Im}(n_{eff}) \quad (2.5)$$

The aim was to avoid additional loss due to p- and n-doped regions. Si-

CHAPTER 2. NUMERICAL SIMULATIONS OF THE SOI WAVEGUIDE FOR CW FOUR WAVE MIXING

a silicon waveguide, induces the free carriers generation via TPA phenomenon. The average density of free carriers in the waveguide cross-section can be calculated then with the equation (1.30) [29]. The change in the optical power P along the waveguide propagation direction z , due to TPA and TPA induced FCA can be described using the following formula [29]:

$$\frac{dP(z)}{dz} = -\alpha_{lin} \cdot P(z) - \frac{\beta_{TPA}}{A_{eff}} \cdot P^2(z) - \Delta\alpha_{FCA} P(z) \quad (2.6)$$

where α_{lin} is the linear loss coefficient, β_{TPA} is the TPA coefficient, $\Delta\alpha_{FCA}$ is expressed as in equation (1.31).

Numerical calculations were performed to investigate the sole influence of linear loss, TPA and TPA induced FCA. The calculations considered the waveguide height $H_{wg} = 220 \text{ nm}$, width $W_{wg} = 500 \text{ nm}$ and slab thickness $s_{wg} = 50 \text{ nm}$ ($A_{eff} = 0.1 \mu\text{m}^2$). The TPA coefficient β_{TPA} was assumed to be $5.6 \cdot 10^{-10} \text{ cm/W}$ in all the calculations. The value of β_{TPA} is the result of the measurement referred to in subsection 3.3.5). The calculations were performed applying the method introduced in subsection 1.2.9, considering the single wave propagating through the waveguide with the input power $P(0)$.

Here the total insertion loss of the waveguide is defined as:

$$IL \text{ [dB]} = 10 \cdot \log_{10} \left(\frac{P(0)}{P(L_{wg})} \right) \quad (2.7)$$

were the optical power P is given in Watts. At first (figure 2.16), the impact of TPA ($\tau_{eff} = 0 \text{ ps}$, blue curve) on IL was investigated. Then TPA induced FCA with τ_{eff} up to 3 ns was examined as a function of the input power ($P(0)$). The free carrier lifetime τ_{eff} , as short as 50 ps with the input power $P(0) = 30 \text{ dBm}$ causes substantial loss increase. At this input power the 3 ns free carrier lifetime results for this power in over 10 dB excess loss. The τ_{eff} of 3 ns is commonly assumed for the case of the sub-micron silicon waveguides without a lateral p-i-n diode. The high TPA induced FCA could have been a reason to consider different material platforms or a pulsed operation with the low repetition rate to benefit from nonlinear optical effects.

Secondly the impact of the linear loss on IL was examined. Here the power

2.2. OPTICAL PROPERTIES OF SILICON NANO-RIB WAVEGUIDE WITH LATERAL P-I-N DIODE

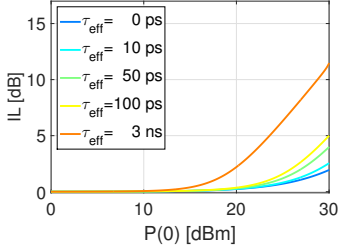


Figure 2.16: Insertion loss (IL) versus $P(0)$ for different τ_{eff} for $\alpha_{\text{lin}} = 0 \text{ dB/cm}$ and $L_{\text{wg}} = 1 \text{ cm}$.

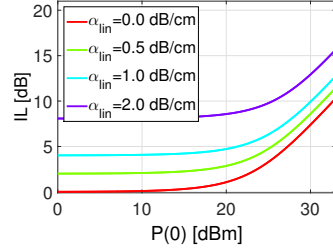


Figure 2.17: Insertion loss (IL) versus $P(0)$ for different α_{lin} , $\tau_{\text{eff}} = 50 \text{ ps}$ and $L_{\text{wg}} = 4 \text{ cm}$.

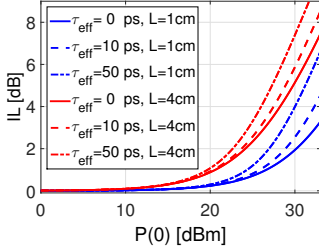


Figure 2.18: Insertion loss (IL) versus $P(0)$ for different L_{wg} , $\tau_{\text{eff}} = 50 \text{ ps}$ and $\alpha_{\text{lin}} = 0 \text{ dB/cm}$.

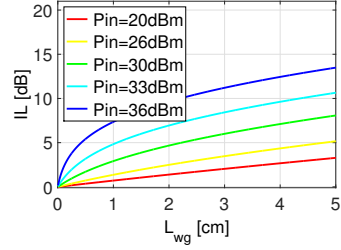


Figure 2.19: Insertion loss (IL) versus L_{wg} for different $P(0)$, $\tau_{\text{eff}} = 10 \text{ ps}$ and $\alpha_{\text{lin}} = 0.5 \text{ dB/cm}$.

higher than 4 W (36 dBm) incoupled to the waveguide was not considered, since the optical intensity damage threshold of the silicon material $I_{\text{damage}} = 1 - 4 \text{ GW/cm}^2$ [25]. With the effective area $A_{\text{eff}} \approx 10^{-9} \text{ cm}^2$ the intensity reaches 4 GW/cm^2 in the waveguide core. Figure 2.17 depicts the impact of the different values of the linear loss coefficient α_{lin} on the insertion loss in the 4 cm long sample. Lower increase in the nonlinear loss from TPA and FCA, results from the high linear attenuation of the pump. The impact of both carrier lifetime and TPA on IL is depicted in figure 2.18 for $\alpha = 0 \text{ dB/cm}$ and two waveguide lengths 1 and 4 cm . This picture shows the insertion loss generated by only TPA as well as by both FCA and TPA mechanisms.

Figure 2.19 presents the evolution of the IL along the waveguide for the different input power levels ($P(0)$). The increase of the input power causes

CHAPTER 2. NUMERICAL SIMULATIONS OF THE SOI WAVEGUIDE FOR CW FOUR WAVE MIXING

the increase of the generation rate. When the input power is high enough to generate the free carriers faster than they can be removed from the guiding area, the accumulation of the free carriers starts, thus increasing IL . Therefore in the next section an optimization of the p-i-n diode scheme, to sweep out the free carriers from the waveguide area will be performed. The model presented in this section was used later to fit the experimental data in the subsection 3.3.5.

2.3 Simulations of CW four wave mixing in SOI waveguide

Using the software described in section 1.2.9 the simulations of the continuous-wave (CW) four wave mixing (FWM) in the waveguides were performed. In this section the discussion is limited to the pump degenerated FWM effect (see figures 2.21 and 2.20). In figure 2.20 the typical spectrum obtained from the simulation tool was plotted. Figure 2.21 presents the waveguide and spectra before and after conversion.

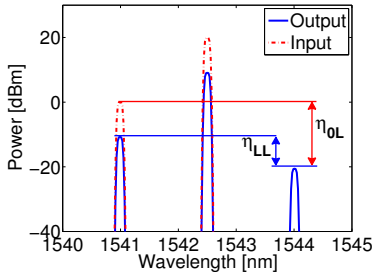


Figure 2.20: Input and output spectrum with the η_{OL} and η_{LL} .

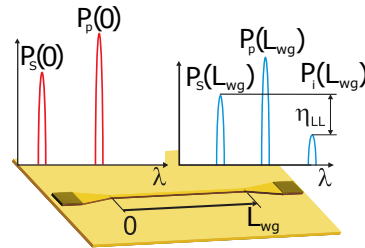


Figure 2.21: Scheme of η_{LL} determination.

For the clarity of the description and discussion of the results, two definitions of FWM wavelength conversion efficiency need to be introduced. Both of them are widely used in the literature describing FWM interaction in the silicon waveguide [27, 29, 49, 61].

The first definition is given by the formula (also in 1.2.8):

2.3. SIMULATIONS OF CW FOUR WAVE MIXING IN SOI WAVEGUIDE

$$\eta_{0L} = \frac{P_i(L_{wg})}{P_s(0)} \quad (2.8)$$

where the output power of the idler $P_i(L_{wg})$ is compared to the input signal power $P_s(0)$. This conversion efficiency definition is widely used in theoretical analysis and incorporates the loss and gain properties of the medium [27, 29]. However, for the sake of measurements some authors used the more convenient approach [42, 62]:

$$\eta_{LL} = \frac{P_i(L_{wg})}{P_s(L_{wg})} \quad (2.9)$$

where $P_i(L_{wg})$ and $P_s(L_{wg})$ are signal and the idler at the output of the measured sample. The formula (2.9) simplifies the necessary measurement setup and introduces less uncertainty in the evaluation of the results. Measuring and comparing signal and idler powers at the output allows for a straightforward determination of the conversion efficiency as shown in figure 2.21. The method to calculate η_{LL} was plotted in figure 2.21. For the purpose of replication of the signal guided at one wavelength it is enough to know the ratio between the signal and the idler at the output. However, if the four wave mixing gain properties shall be evaluated, the η_{0L} shall be applied. The other quantity used to evaluate the strength of the FWM effect is the nonlinear signal transmission which will be referred to as the gain, defined as follows:

$$G = \frac{P_s(L_{wg})}{P_s(0)} \quad (2.10)$$

In general the wavelength conversion efficiency depends on the following factors: pump power, waveguide dispersion, linear and nonlinear loss. The results presented below were obtained for the waveguide dimensions $W_{wg} = 500 \text{ nm}$, $H_{wg} = 220 \text{ nm}$ and $s_{wg} = 50 \text{ nm}$ ($A_{eff} = 0.1 \mu m^2$). In this analysis, the value of the material dispersion coefficient $D = -1.6 \text{ ps/nm} \cdot m$ is used. This coincides with the results in the figure 2.13. The linear loss of 1 dB/cm was taken into account. The TPA coefficient $\beta_{TPA} = 5.6 \cdot 10^{-10} \text{ cm/W}$ as in section 3.3.5. Below the effect of the pump power on the conversion efficiency was evaluated. The pump and signal wavelengths were fixed at 1552.5 nm and 1550 nm respectively, thus detuning $\delta\lambda = 2.5 \text{ nm}$. The input pump power $P_p(0)$ was scanned in the range from

CHAPTER 2. NUMERICAL SIMULATIONS OF THE SOI WAVEGUIDE FOR CW FOUR WAVE MIXING

10 to 30 dBm and the dispersion coefficient $D = -2$ ps/nm.m. These wavelengths of pump and signal disable the positive gain or the conversion efficiency η_{0L} . On the other hand η_{LL} can reach very high values as was confirmed experimentally in [61].

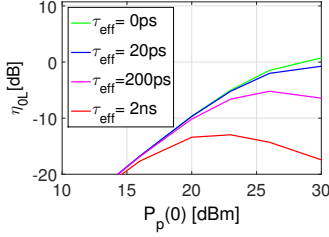


Figure 2.22: Conversion efficiency η_{0L} versus $P_p(0)$ for various carrier lifetimes τ_{eff}

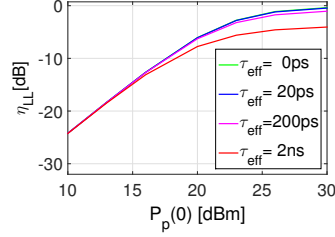


Figure 2.23: Conversion efficiency η_{LL} versus $P_p(0)$ for various carrier lifetimes τ_{eff}

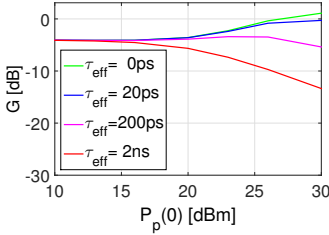


Figure 2.24: Gain G versus $P_p(0)$ for various carrier lifetimes τ_{eff}

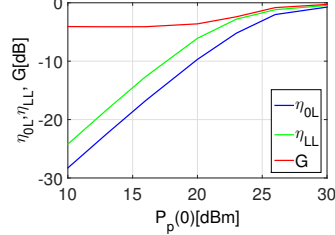


Figure 2.25: G , η_{0L} and η_{LL} versus $P_p(0)$ for carrier lifetime $\tau_{eff}=20ps$

In figures 2.22-2.25 the conversion efficiency η_{0L} , η_{LL} and the gain G are presented as a function of the input power $P_p(0)$. The values were calculated for the linear loss coefficient $\alpha_{lin} = 1$ dB/cm and waveguide length of 4 cm. The first three figures represent simulations of each single quantity for free carrier lifetimes τ_{eff} of 0, 20, 200 and 2000 ps. The fourth one depicts η_{0L} , η_{LL} and G for the effective carrier lifetime $\tau_{eff} = 20$ ps.

Below in this section the prospective of enhancing the CW FWM wavelength conversion at 1550 nm wavelength is discussed. During the propagation of the light the nonlinear phase change can be compensated by an anomalous dispersion of the waveguide. This compensation results in the

2.3. SIMULATIONS OF CW FOUR WAVE MIXING IN SOI WAVEGUIDE

FWM gain (G) at the wavelength detuned from the pump wavelength by a few nano-meters. With the increase of the waveguide length the peaks of gain are positioned closer to the pump wavelength. Following the introduction in 1.2.8 the CW FWM model (see 1.2.9) is used to draw the perspective of increasing of both the wavelength conversion efficiency and the gain.

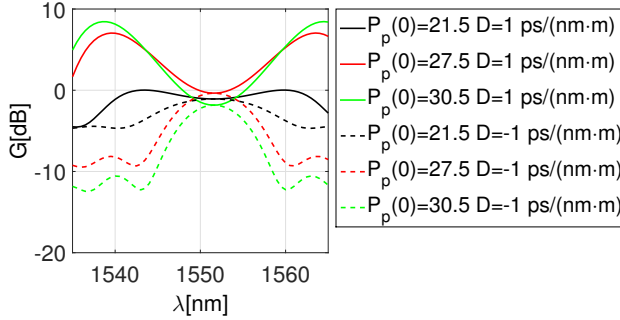


Figure 2.26: Gain versus wavelength for anomalous(solid) and normal(dashed) dispersion of $1\text{ps}/\text{nm} \cdot \text{m}$ for free carriers effective lifetime of $\tau_{\text{eff}} = 60\text{ps}$ and linear loss $\alpha = 0.5\text{dB}/\text{cm}$, $L_{\text{wg}} = 4.48\text{ cm}$, $A_{\text{eff}} = 0.1\text{ }\mu\text{m}^2$. (Input power $P_p(0)$ in dBm)

As shown in section 3.3.2, extending the waveguide rib height to 400 nm and using the silicon oxide cladding, results in the anomalous dispersion of $D = 1\text{ps}/(\text{nm}\cdot\text{m})$. Provided that the linear loss $\alpha = 1\text{ dB}/\text{cm}$ can be maintained or lowered to 0.5 dB, the gain can be positive. In the present analysis, the CW FWM was simulated considering the nonlinear parameter $\gamma = 280\text{ }1/[(W \cdot \text{m})]$ and TPA coefficient $\beta_{\text{TPA}} = 0.56 \cdot 10^{-11}[\text{m}/\text{W}]$. From this simulation it can be concluded that the positive gain is achieved only in the case of the anomalous dispersion. Figure 2.26 illustrates how the change of the dispersion from normal to anomalous affects the gain.

Figure 2.27 presents the gain versus the wavelength of the signal for the pump wavelength 1551.6 nm. With realistic assumptions (e.g. $\alpha_{\text{lin}}, \gamma, \beta_{\text{TPA}}$) a gain of around 8 dB may be obtained. Taking into account the possible reduction in the coupling loss of the grating coupler to 1 dB/coupler as in [63], the silicon waveguide may perform an external gain up to 6 dB.

CHAPTER 2. NUMERICAL SIMULATIONS OF THE SOI WAVEGUIDE FOR CW FOUR WAVE MIXING

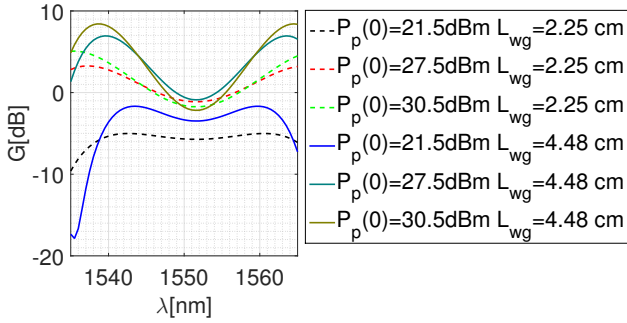


Figure 2.27: Gain versus wavelength at different pump power $P_p(0)$ and the two waveguide lengths 2.25 (dashed) and 4.48 cm (solid), $\alpha_{lin} = 0.5\text{dB/cm}$, $\tau_{eff} = 60\text{ps}$.

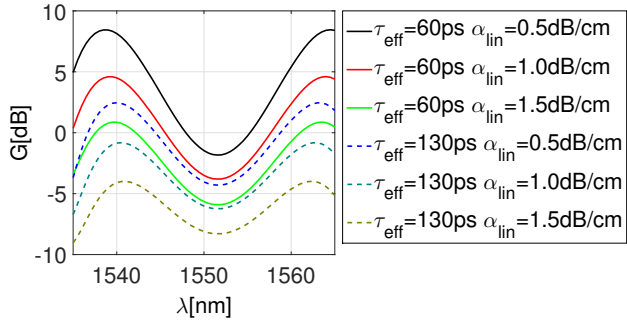


Figure 2.28: Gain versus wavelength for free carriers effective lifetime τ_{eff} of 60 and 130 ps and linear loss of 0.5 and 1dB/cm.

Additionally, the CW FWM gain varies with the waveguide loss coefficient α_{lin} and the effective free carrier lifetime (τ_{eff}). In this analysis, two realistic values of τ_{eff} and three values of α_{lin} were considered. These values were obtained by fitting the measured wavelength conversion efficiency reported later in section 3.3.5. Figure 2.28 presents the change in the gain of the 4.48 cm long waveguide with the varying loss coefficient α_{lin} and the free carrier lifetime τ_{eff} .

2.4 Reduction of free carrier lifetime

Many research groups examined the optical nonlinear effects around 1550 nm wavelength in silicon waveguides and faced the problem of accumulating carriers in the waveguide [22,29,37,48,64,65]. Accumulated carriers provoke the increase of the insertion loss (see 1.2.4), and detrimentally influence the efficiency of the nonlinear optical effects. Two concepts were developed to prevent the free electrons and holes from staying in the waveguide region. In the first concept the free carrier lifetime in the waveguide region decreases due to the implantation of different ions that serve as recombination centers. The results obtained with the implantation of helium He ions by Liu and Tsang [66], demonstrated a decrease of the effective carriers lifetime (τ_{eff}) from 100 ns to 1.9 ns with an increase of the linear loss ($\sim 0.3\text{dB/cm}$) due to the limited implant dose of 10^{12}cm^{-2} . The rib waveguide used in the experiment was $4\text{ }\mu\text{m}$ wide with an effective area of $6.2\text{ }\mu\text{m}^2$. Experiments with smaller waveguides and other ions, e.g. gold (Au) [67], Ar [68], O [69,70] or Si [71], usually led to a higher increase of loss due to doping. Decreasing the effective free carrier lifetime with these techniques and thus diminishing FCA, increased substantially the propagation loss due to the scattering from imperfections caused by implanted ions. This severe decrease in transmission through the doped waveguides made the devices in most of the cases inefficient and hence another solution had to be found.

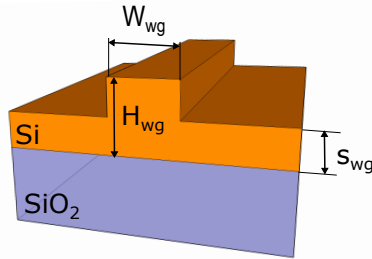


Figure 2.29: Schematic view of the silicon rib waveguide used gold doping experiment.

Part of this research project was Au doping of the waveguide with the width $W_{wg} = 1.5\text{ }\mu\text{m}$, height $H_{wg} = 1.5\text{ }\mu\text{m}$ and the slab height $s_{wg} =$

CHAPTER 2. NUMERICAL SIMULATIONS OF THE SOI WAVEGUIDE FOR CW FOUR WAVE MIXING

0.7 μm . For this purpose the commercially available Au spin-on-dopant was used. After spinning of the Au spin-on-dopant layer on top of the sample, the samples have been heated up to 800°C in the diffusion oven to promote diffusion of the Au ions into silicon. Four temperatures (500°C, 600°C, 700°C and 800°C) and two different diffusion times (10 minutes at 500°C, 700°C and 20 minutes at 800°C) were applied. Experimenting with parameters mentioned above it was expected to achieve different concentrations of gold in the silicon guiding layer. It must be noticed that gold saturating solubility levels are strongly dependent on the diffusion temperature. Figure 2.30 shows the results of the experiment. There is a clear disadvantage coming from the additional scattering loss ($\Delta\alpha_{\text{lin}}$) even though the carrier lifetime τ_{eff} decreased five times. Following these results, the possibility of an improvement in the loss figure was examined. Since no better value of the loss was obtained, the carrier lifetime modification by Au

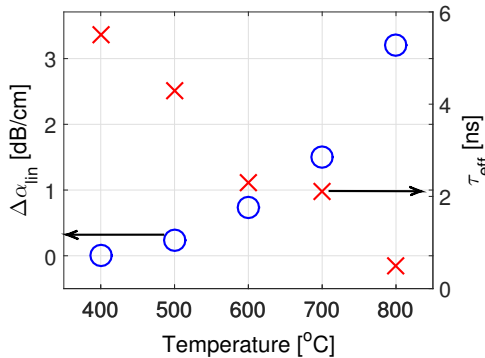


Figure 2.30: Excess linear loss $\Delta\alpha_{\text{lin}}$ and effective free carrier lifetime τ_{eff} in the 1.5 μm Au doped silicon rib waveguide versus diffusion temperature.

The active carrier removal was proposed as a solution, as it does not imply an increase of the loss while decreasing the carrier lifetime. In this method a reverse biased lateral p-i-n diode placed along the waveguide removes free carriers from the waveguide region. This solution was proposed by Rong et al. [64, 72, 73], who constructed the first all-silicon Raman laser, and demonstrated the most efficient four wave mixing observed in silicon rib waveguides until that time. Later Turner-Foster et al. proved experimentally that the effective carrier lifetime as short as 12 ps in a silicon

2.5. ELECTRIC SIMULATIONS OF FREE CARRIER LIFETIME IN WAVEGUIDE WITH LATERAL P-I-N DIODE

nano-rib waveguide can be obtained [38]. At the same time the electrical simulations were made within this research and the design rules for non-linear p-i-n assisted nano-rib waveguide were published [74]. The method will be described in the section 2.5.

2.5 Electric simulations of free carrier lifetime in waveguide with lateral p-i-n diode

In this section the well-established electronic device modeling techniques are used to analyze the free carrier lifetime reduction in the waveguide structures with a lateral p-i-n diode. The analysis covers the dependence of the carrier lifetime on the waveguide geometry, the intrinsic region width and the carrier screening effects. Some of the material discussed in this section was already presented in [74]. A vital part of the study were the carriers lifetime simulations in the waveguide structure with the commercially available Sentaurus Workbench software developed for the electronic device modeling [75]. The electronic device modeling using a commercial software was already applied to free carrier lifetime studies in p-i-n waveguide structures [36]. In a prior work, however, the authors focused their research on larger silicon waveguides (above $0.5\mu m$ silicon thickness) and obtained the free carrier lifetimes for the smallest structure in the order of hundreds of picoseconds. In [36], the smallest considered separation between doping regions was $w_i = 2.25 \mu m$. The dependence of the free carrier lifetime on the sole etch depth of the rib was not taken into account. The following section shows how the rib etch depth influences the performance of nano-rib waveguides. In [64] the authors confirmed experimentally the effectiveness of the p-i-n structures for the reduction of the free carrier lifetime in silicon waveguides and demonstrated a CW Raman laser on a SOI platform. Later, the free carrier lifetime in a smaller nano-rib waveguide ($H_{wg} = 295 nm$, $W_{wg} = 660 nm$, $s_{wg} = 40 nm$) was studied experimentally and published by Turner-Foster et al. [38], resulting in $\tau_{eff} = 12ps$. Other work focused on the modeling of the longitudinal carrier transport [76].

This analysis is based on the two-dimensional simulations of the transverse carrier transport in the waveguide with lateral p-i-n diode. A numerical finite element method for carrier recombination and transport in silicon was used to obtain the free carriers density (N_e , N_h) and velocity (v_e , v_h) across the waveguide cross-section. Since the software is multi-

CHAPTER 2. NUMERICAL SIMULATIONS OF THE SOI WAVEGUIDE FOR CW FOUR WAVE MIXING

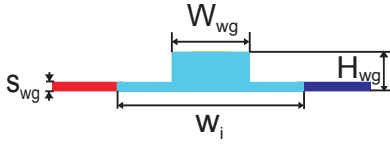


Figure 2.31: Scheme of the waveguide with marked doping regions

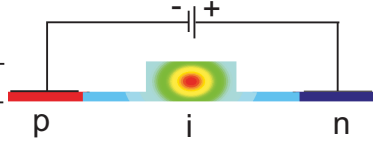


Figure 2.32: Bias connection scheme for p-i-n assisted waveguide and free carriers generation profile

purpose, containing a big number of implemented electrical models and numerical algorithms, the models recommended by the user guide were included in the calculations of the free carriers transport and diffusion [75]. The default values of the material parameters were provided by the simulation platform and used in the present analysis. Single photon absorption model incorporated in the software was used to simulate the free carriers generation in the waveguide region, since the TPA was not available in the software. Hence it was possible to define the generation profile in the waveguide region. The generation of the carriers by single photon absorption was set to be equal to the expected from TPA in the real structure G_{TPA} (equation(1.30)) [36,37]. However, instead of the real mode profile (figure 2.6), the Gaussian distribution of the carriers generation was used with the comparable size (see figure 2.32. The elliptical Gaussian and the mode profile were matched to have the same full-width at half maximum in either width and height. When the reverse bias voltage is applied to the p-i-n structure, the carrier transport mechanism dominates over recombination and diffusion mechanisms [36]. Electron and hole velocities obtained in the simulations were used to calculate the effective carrier lifetime according to the formula [36]:

$$\tau_{eff} = \frac{W_{wg}}{4} \left(\frac{1}{v_e} + \frac{1}{v_h} \right) \quad (2.11)$$

where W_{wg} is the waveguide width, and v_e, v_h are the velocity of electrons and holes respectively. For the calculation of free carrier absorption the equation (1.29) was used. The above stated approximations may result in a deviation from the real situation. Nevertheless, the free carrier lifetimes obtained this way match to the order of magnitude of the experimental results reported by Turner-Foster et al. [38]. On the other hand in the de-

2.5. ELECTRIC SIMULATIONS OF FREE CARRIER LIFETIME IN WAVEGUIDE WITH LATERAL P-I-N DIODE

sign procedure it was more important to define trends than to establish accurate absolute values of the effective free carrier lifetime.

This research concerns the waveguide (figure 2.31) with the fixed width (W_{wg}) and height (H_{wg}). Three slab height values (s_{wg}) were examined to quantify its impact on the carrier lifetime (τ_{eff}). The different values of the doping regions separation (w_i) and reverse bias voltage (U_{bias}) were also checked. The chosen optical power (P) range was between the value where the considerable TPA starts and the middle of the optical damage threshold reported in the table 1.2. The summary of the electrical simulations parameters is given in the table 2.2.

Parameter	Value	Unit
Waveguide width W_{wg}	500	nm
Waveguide height H_{wg}	220	nm
Waveguide slab height s_{wg}	50,100,150	nm
Doping regions separation w_i	1.0 to 2.4	μm
Bias voltage U_{bias}	-35 to 0	V
Optical power P	7 to 33	dBm
Wavelength λ	1550	nm

Table 2.2: Values of input parameters used in the electric simulations of the carrier density and transport by Sentaurus Device software [75]

In the first simulations the electric field distribution in the waveguide cross-section was examined with the carriers generation corresponding to the low light power ($P = 5mW$) and without reverse bias voltage ($U_{bias} = 0V$). Two slab heights (s_{wg}) of 50 and 150 nm were considered.

Results are presented in figure 2.33(a). Clearly higher electrons velocity (v_e) was obtained for the slab height $s_{wg} = 150\text{ nm}$. It can be attributed to the better penetration of the waveguide rib by the applied electric field (E_{bias}). The effect of applying 25 V reverse bias voltage (U_{bias}) to both structures is visualized in Figure 2.33(b). Under the low power conditions the carriers velocity saturated at v_{sat} in both structures. When increasing the optical power to 1 W, we observed a drop of the electrons velocity in the waveguide region (figure 2.34). The reason for this is the screening of the electric field by free carriers accumulated in the waveguide rib. In the waveguide with $s_{wg} = 150\text{ nm}$ the effect is less pronounced.

The further analysis focused on the influence of the applied reverse bias

CHAPTER 2. NUMERICAL SIMULATIONS OF THE SOI WAVEGUIDE FOR CW FOUR WAVE MIXING

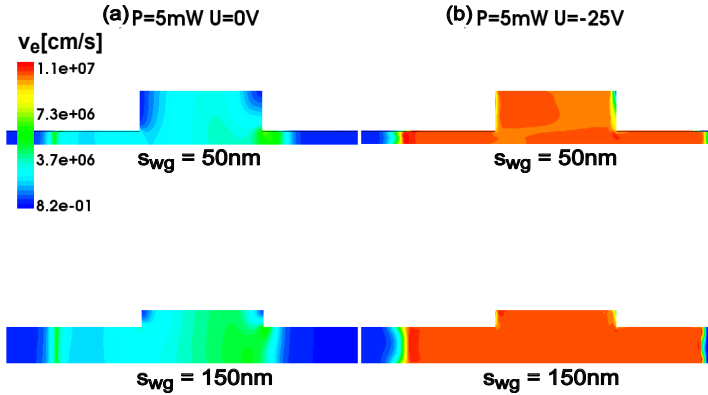


Figure 2.33: Electron drift velocity across the waveguides cross-section for slab heights s_{wg} of 50 nm and 150 nm. (a) $P=5mW$, $U_{bias}=0V$ (b) $P=5mW$, $U_{bias}=-25V$

voltage on the electrons velocity (v_e). The τ_{eff} and $\Delta\alpha_{FCA}$ were chosen as measures of the free carriers sweep efficiency. Two types of waveguides were considered: with the lateral p-i-n diode and without (simple waveguide). The waveguide with the lateral p-i-n diode was examined with different levels of the reverse bias voltage. Figures 2.35 and 2.36 show the advantage of using the lateral diode. The simple waveguide, had the following dimensions $W_{wg} = 500nm$, $H_{wg} = 220 nm$ and $s_{wg} = 50 nm$. This waveguide was compared to the waveguide with the same dimensions and the lateral p-i-n diode with $w_i = 1.2 \mu m$. The black line (figure 2.35) represents the dependence of $\Delta\alpha_{FCA}$ on the incoupled optical power (P) in the waveguide without p-i-n diode. A significant growth of the $\Delta\alpha_{FCA}$ is observed already at $P = 21dBm$.

The built-in electric field (red line, 0V bias) introduced solely by the doping regions sweeps the free carriers away. Therefore, the $\Delta\alpha_{FCA}$ -rise shifts towards 25 dBm. However, above this power the free carriers generated by TPA accumulate and screen the electric field. In a sub-micrometer photonic wire waveguide, FCA appears for even lower power level, thus lowering the FWM wavelength conversion efficiency at CW operation [48]. The reverse biased p-i-n diode lateral to the waveguide can push the carrier screening limit towards the power beyond 30dBm (green line) (Figure

2.5. ELECTRIC SIMULATIONS OF FREE CARRIER LIFETIME IN WAVEGUIDE WITH LATERAL P-I-N DIODE

c) $P=1W$ $U=-25V$

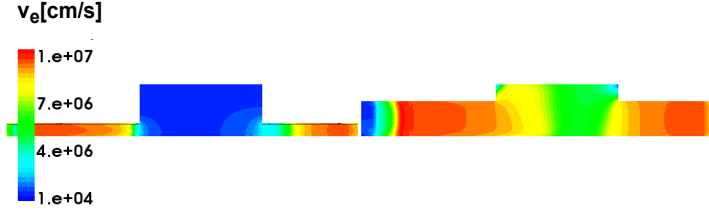


Figure 2.34: Electron drift velocity decrease, due to carriers screening, across the waveguide crosssection for slab heights s_{wg} of 50 nm(left) and 150 nm(right), power $P = 1 W$ and bias $U_{bias} = -25 V$.

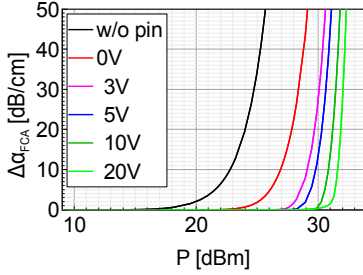


Figure 2.35: Excess free carrier loss coefficient $\Delta\alpha_{FCA}$ versus P in the waveguide for different U_{bias} ($w_i = 1.2 \mu m$, $s_{wg} = 50 nm$).

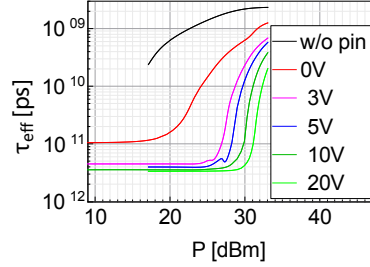


Figure 2.36: Free carrier lifetime τ_{eff} versus P in the waveguide for different U_{bias} , ($w_i = 1.2 \mu m$, $s_{wg} = 50 nm$).

2.36). Nonetheless, the reverse U_{bias} is limited by the breakdown voltage as expressed below:

$$V_{BD} = \mathcal{E}_{BD} \cdot w_i \quad (2.12)$$

where $\mathcal{E}_{BD} = 2.5 \cdot 10^5 V/cm$ is the breakdown field of silicon and w_i is the width of the intrinsic region [24]. The breakdown voltage of the structures analyzed in this work varies from 20 V to 40 V. The shortest carrier lifetime shown in figure 2.36 results from the maximum drift velocity of free carriers v_{sat} (for both electrons and holes the same [24]) and can be estimated from:

CHAPTER 2. NUMERICAL SIMULATIONS OF THE SOI WAVEGUIDE FOR CW FOUR WAVE MIXING

$$\tau_{eff,min} = \frac{1}{v_{sat}} \cdot \frac{W_{wg}}{2} \cong 3 \cdot 10^{-12} s \quad (2.13)$$

where $v_{sat} \cong 10^7 \text{ cm/s}$ and W_{wg} is the waveguide width. Next, it was examined how the distance between doping regions w_i impacts on the free carriers removal efficiency. Therefore, the waveguide with the dimensions: $W_{wg} = 500 \text{ nm}$, $H_{wg} = 220 \text{ nm}$, $s_{wg} = 50 \text{ nm}$ was analyzed. The simulations were conducted for three values of w_i ($1.0 \text{ }\mu\text{m}$, $1.2 \text{ }\mu\text{m}$ and $2.4 \text{ }\mu\text{m}$) and the applied bias voltage of 0 V and -20 V .

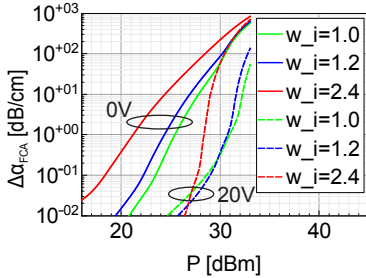


Figure 2.37: $\Delta\alpha_{FCA}$ versus optical power P for w_i of $1.0, 1.2, 2.4 \text{ }\mu\text{m}$ and bias voltage of 0 and -20 V .

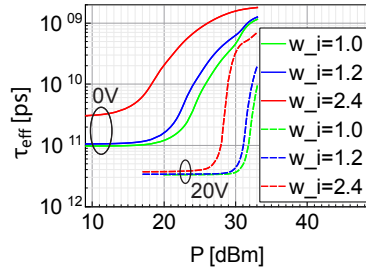


Figure 2.38: Free carrier lifetime τ_{eff} versus optical power P for w_i of $1.0, 1.2$ and $2.4 \text{ }\mu\text{m}$ and U_{bias} of 0 and -20 V .

For $U_{bias} = -20 \text{ V}$ and closely placed doping regions (e.q. $w_i = 1.0$ and $1.2 \text{ }\mu\text{m}$) at the power $P = 30 \text{ dBm}$ it was observed that $\Delta\alpha_{FCA}$ decreased by almost two orders of magnitude compared to the case with $U_{bias} = 0 \text{ V}$. The doping regions separation of $2.4 \text{ }\mu\text{m}$ even with the reverse biased junction also became inefficient.

Further it was simulated how the slab height (s_{wg}) influences the τ_{eff} and $\Delta\alpha_{FCA}$. The parameters concerned were as follows: $w_i = 1.2 \text{ }\mu\text{m}$ and three values of s_{wg} : $50, 100$ and 150 nm . The figures 2.39 and 2.40 show the results. In the linear mode (bottom dashed lines) there is no significant influence of the slab height, since the number of generated carriers is small. The $P = 1 \text{ W}$ generates substantially more carriers. The thinner the slab, the higher must be the reverse bias voltage, in order to remove the free carriers from the waveguide region. At the $U_{bias} = -30 \text{ V}$ there is an indication of $\Delta\alpha_{FCA}$ increase. This effect can be attributed to the fact that, the

2.5. ELECTRIC SIMULATIONS OF FREE CARRIER LIFETIME IN WAVEGUIDE WITH LATERAL P-I-N DIODE

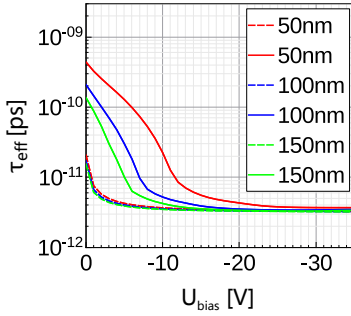


Figure 2.39: Free carrier lifetime τ_{eff} versus U_{bias} for different s_{wg} and P of 1mW(dashed) and 1W(solid).

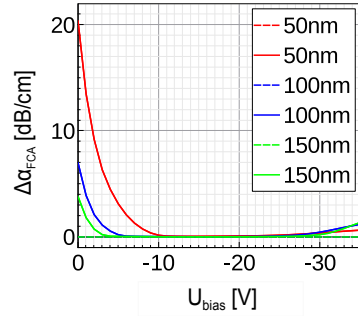


Figure 2.40: Excess free carrier loss $\Delta\alpha_{FCA}$ versus U_{bias} for different s_{wg} and P of 1mW(dashed) and 1W(solid).

number of carriers is enough to establish current flow through the junction. The difference between $\Delta\alpha_{FCA}$ in the waveguides with s_{wg} of 50 nm (dashed) and 150 nm (solid) becomes more evident with the growth of the optical power.

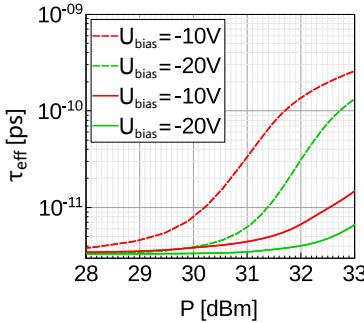


Figure 2.41: Free carrier lifetime τ_{eff} versus P for s_{wg} of 50 nm (dashed) and 150 nm (solid) for U_{bias} -10 V and -20 V .

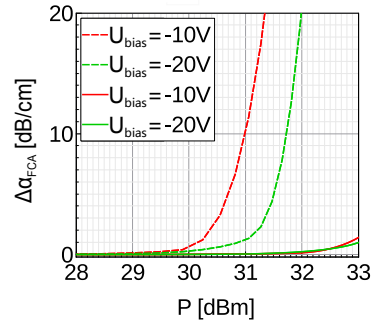


Figure 2.42: Excess free carrier loss $\Delta\alpha_{FCA}$ versus P for s_{wg} of 50 nm (dashed) and 150 nm (solid) for U_{bias} -10 V and -20 V .

The shallow etch waveguide would be the preferred choice, to achieve

CHAPTER 2. NUMERICAL SIMULATIONS OF THE SOI WAVEGUIDE FOR CW FOUR WAVE MIXING

an efficient carriers sweeping from the waveguide region. It enables the efficient free carrier removal at high optical powers. However, this waveguide exhibits high normal dispersion as presented in the section 2.2.3, that results in the very narrow FWM bandwidth. Although absolute values extracted from the CW measurement reported further in this thesis 3.3.5 differ by one up to two orders of magnitude from the presented here. This may be caused by the samples imperfections e.g. lower then expected voltage in the waveguide in the realized structures. Eventually the additional effects that were not taken into account in the simulations occurred in the real samples. Although the absolute values of τ_{eff} may be underestimated, the trends obtained with this method led to the optimization of the nonlinear waveguide with lateral p-i-n diode.

From the simulation results discussed in chapter 2 it is clear, that a compromise needs to be found between a demand for the anomalous dispersion and the free carriers sweeping efficiency ($\tau_{eff} < 10$ ps). The first requires high ($H_{wg} > 220$ nm) and deeply etched waveguide ($s_{wg} = 50$ nm) while the latter would promote use of the shallow etching ($s_{wg} \approx 150$ nm). The shallow etching proved also to be an ideal method to keep the waveguide loss very low [52]. This would help in reaching gain, provided that the anomalous dispersion was obtained. However the shallow etching of the waveguide determines the high normal dispersion. The broadband and highly efficient wavelength conversion (see equations (1.56) and (1.58)) can be obtained only if the anomalous dispersion regime is provided. Moreover, the efficient wavelength conversion and the gain can be obtained only if the linear loss is suppressed ($\alpha_{lin} < 1$ dB/cm). It is also worth mentioning that the cross-section of the waveguide is considerably smaller then the fiber core. An efficient incoupling scheme must also be ensured to avoid the loss at the interface fiber-to-waveguide. This issue will be addressed in the section 3.2.

3

Design, fabrication and characterization of samples

The integration of the p-i-n lateral diode along the nano-rib waveguide is beneficial for the nonlinear optical applications. This was discussed in sections 1.2.4, 1.2.8 and 2.5. The electrical simulations presented in section 2.5 proved that the smaller the separation is between the doping areas w_i the more efficient is removal of free carriers i.e. the lower the loss from the TPA induced FCA. In this chapter the fabrication process of the samples is introduced. It is described which challenges stand still on the way towards the realization of a silicon nano-rib waveguide for the FWM process. In section 3.1 the design process of the samples shall be presented. Later in the section 3.2 the fabrication process will be discussed, emphasizing the challenges in the production and some potential improvements that can be applied in the future. In section 3.3 the results of the characterization of the waveguides will be presented. Firstly, the electrical and optoelectrical characteristics of the waveguide with p-i-n diode will be measured in section 3.3.1. The description of the dispersion measurement will be presented in section 3.3.2. In section 3.3.3 the linear optical characteristics will be determined. The measurement of the dependence of the linear optical loss on the applied bias voltage will be described in section 3.3.4. Moreover, it will shown how the p-i-n diode influence the propagation of the light in the waveguide. Later in section 3.3.5 the measurement of the power dependent loss originating from TPA and TPA induced FCA will be reported. The CW four wave mixing measurements are described in section 3.3.6. In section 3.3.7 the phase sensitive amplification (PSA) for the wavelengths around 1550 nm will be demonstrated.

3.1 Samples design

Designing a waveguide for the nonlinear applications, one shall take into account the constraints of the material platform as well as the available technology.

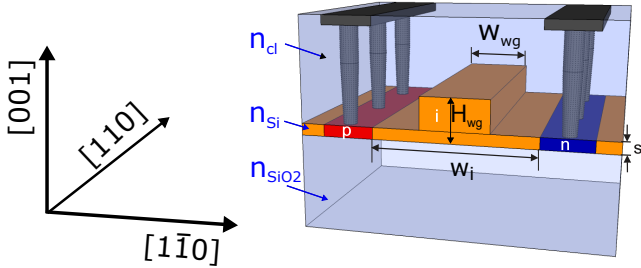


Figure 3.1: Schematic view of silicon nano-rib waveguide with lateral p-i-n diode, showing bottom SiO₂, cladding, metal contacts and metal paths at the top of the structure.

It is recalled that the focus of this research is to verify, whether it is possible to obtain a substantial enhancement of the CW FWM wavelength conversion efficiency η_{LL} in the SOI waveguide around the 1550nm wavelength. For this purpose it was decided in the design process that the samples must contain several nano-rib silicon waveguide with and without the lateral p-i-n diode. At first, the height of the rib was set by the commonly available SOI wafers to 220 nm. As already discussed in section 2.2.3 the waveguide with this height does not show the anomalous dispersion, which is normally required to obtain the FWM gain. Nevertheless, from earlier experiments it was supposed that such design could be effective and a low linear loss coefficient could be achieved ($\alpha_{lin} \approx 1\text{dB/cm}$). An effective area of $0.1\mu\text{m}^2$ (see 1.2.5) was achieved by setting the waveguide rib width (W_{wg}) and slab thickness (s_{wg}) to 500 nm and 50 nm respectively. The slab thickness of 50 nm was chosen to obtain the high confinement and the sufficient electrical contact for an active removal of free carriers. The waveguides were designed to fit to the process flow for photonic integrated circuits available at the time at the pilot line of IHP. The layout design contained two waveguide types. First one was the pas-

sive waveguides without p-i-n junction carrier removal. The second type contained p (boron) and n (arsenic) doping regions on the sides with doping concentrations of $N_A = 5 \cdot 10^{17} \text{ cm}^{-3}$ and $N_D = 3 \cdot 10^{18} \text{ cm}^{-3}$ respectively. These concentrations were required by the other structures realized on the same wafer. The other structures are irrelevant for this thesis. Nevertheless, the doping concentrations were suitable also for the free carrier removal scheme. In order to provide a good electrical contact within the p and n regions, the highly doped regions were created ($N_A = N_D = 10^{20}$). Next the cobalt silicide was formed on top of the highly doped areas. The cobalt silicide regions were electrically connected with the metal lines and pads via tungsten plugs distributed along them. The designed mask consist of the waveguides without doping regions on the side with lengths L_{wg} of: 1.52 cm, 1.9 cm, 2.37 cm, 2.87 cm, 4.74 cm. The lengths of the waveguides with lateral p-i-n diode were L_{wg} 1.7 cm, 2.25 cm and 4.48 cm. The dimensions of the waveguides are summarized in the Table 3.1.

Waveguide type	Length (L_{wg}) [cm]	w_i [nm]	W_{wg} [nm]	H_{wg} [nm]
no p-i-n	1.52, 1.9, 2.37, 2.87, 4.74	–	500	220
p-i-n	1.7, 2.25, 4.48	1.2	500	220

Table 3.1: Dimensions of the designed waveguides

The design of the p-i-n waveguides must take into account different and sometimes contradictory requirements. On the one hand the electrical scheme should be efficient (low τ_{eff} for a relatively low reverse U_{bias}). This requires a relatively high slab (see section 2.5). On the other hand for the enhancement of the FWM the anomalous dispersion is necessary and thus low slab height would be of advantage (see section 2.2.3. Therefore a compromising solution had to be found. To fulfill these requirements several optical and electrical simulations were performed. The simulations performed in section 2.5 suggests that the smaller the distance between doping regions (w_i) the better. How the separation of the doping regions influences the propagation loss was discussed in section 2.2.4. As result the minimum possible width of the intrinsic waveguide region was defined ($w_i = 1.2 \mu\text{m}$).

3.2 Fabrication process

In this section firstly the design and then the manufacturing will be discussed.

3.2.1 Process design

In this research project the waveguides were fabricated on the 8" silicon-on-insulator wafer with 220 nm thick top layer with the crystal orientation [100] (see figure 3.1). The substrate silicon wafer which is 750 μm thick is separated from the top silicon layer by 2 μm SiO_2 layer. The waveguides were produced along the crystal direction [110]. Apart from the waveguide itself structures serving as an interface between the optical fiber and the waveguide had to be produced. For this purpose the grating couplers were chosen [77]. Two lithography tools were applied: the Deep Ultra Violet (DUV) scanner and the i-line stepper. The DUV scanner with the wavelength of 248 nm served to produce the small size structures with low dimension tolerance, in particular the waveguides and the grating couplers (Grating Coupler (GRC)). Less critical areas (e.g. doping regions) were patterned using the i-line lithography tool with the wavelength 365 nm. In addition, the etching of the silicon, silicon oxide and nitride layers was realized with the Inductively Coupled Plasma (ICP) dry etch tools. The doping areas were created via boron and arsenic ion implantation. The contacts were fabricated by the deposition and patterning of oxides and metals. Several adjustments are required in the fabrication process for the low loss waveguides with sufficient efficiency of the light coupling. The waveguide lithography was a part of the process which needed an adjustment in the first place. The waveguide roughness needed to be lowered to minimum. The first step towards this aim was a proper patterning of the photo-resist (proper setting of the optics and the exposure times in the DUV lithography tool) to avoid the roughness of the exposed photo-resist. Next, the dry etching recipes were adjusted (plasma power, acceleration voltage, gases pressure, temperature, etc.) in the ICP etching tool. This was necessary to minimize the roughness of the sidewalls of the waveguide, thus ensuring low optical loss. It must be noted that the realization of the low loss deep etched waveguides is a key task to obtain the high efficiency broadband FWM on SOI platform. For the purpose of this research project the conservative design of the grating coupler was used, with the simulated coupling efficiency of 3 dB. Although the more efficient grating cou-

pler could be produced, the conservative one proved to be less sensitive to small changes in the dimensions. For the reliability purpose the coupler with the high tolerance for the dimension deviation and lower coupling efficiency was implemented in the design [77]. It needs to be noted that the grating coupler dimensions determine the coupling efficiency as well as the wavelengths that can be coupled to the waveguide.

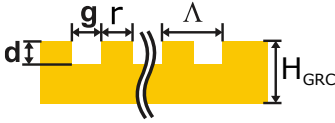


Figure 3.2: Side cross-section scheme of the fiber grating coupler

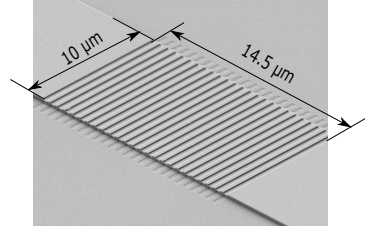


Figure 3.3: SEM picture of the standard fiber grating coupler

In Figure 3.2 the main parameters defining spectral characteristics and the coupling efficiency of GRC were presented. In this research project the height (H_{GRC}) of the grating coupler ridge and waveguide height (H_{wg}) were kept equal. The widths of the grating coupler groove (g) and ridge (r) were optimized in the lithography exposure step to reach $g = r = 315 \text{ nm}$ each. The depth of the grating groove (d) was tuned in dry etching step to 70 nm. The dry etching step, however, also needed to be tuned to avoid the excessive roughness and the change in the dimensions of the grating coupler's features. The manufactured grating coupler is shown in Figure 3.3. The coupling efficiency of the grating coupler with these dimensions was expected to reach about -3 dB . The p and n regions were implanted symmetrically on the sides of the waveguide rib with the separation $w_i = 1.2 \text{ μm}$. The rest of the technology process was taken from the standard front end of the line BiCMOS realization, which is described later. Figure 3.4 shows the procedure of the wafers processing.

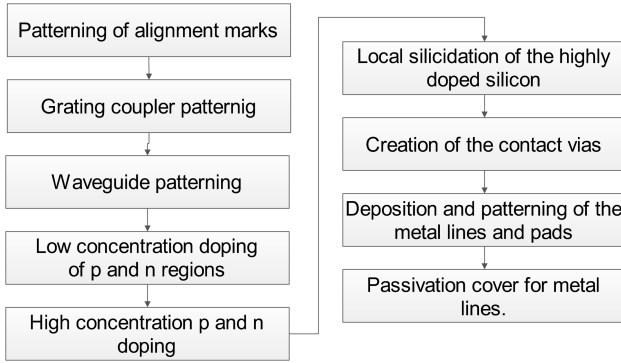


Figure 3.4: Fabrication procedure of samples

3.2.2 Manufacturing

The manufacturing process was performed at the IHP GmbH pilot line in Frankfurt(Oder). As the first step in fabrication, the wafers were cleaned and the alignment marks were patterned and etched. In the following steps the grating couplers and the waveguides were formed by Deep ultra violet (DUV) 248 nm wavelength photo-lithography and ICP dry etching. In the next steps each waveguide was covered and the window in the slab on the side of the waveguide was opened for doping. Boron (B) and arsenic (As) ions were implanted to create p- and n-doped regions respectively. Both regions were separated by 350 nm from the edge of the waveguide rib yielding $w_i = 1.2\mu m$. Within the low dose doping regions the target concentration levels for implanted ions were set for boron to $5 \cdot 10^{17} cm^{-3}$ and for arsenic $3 \cdot 10^{18} cm^{-3}$. Further from the waveguide rib highly concentrated doping regions were placed to create the low resistance contact with the metal pads. On the n-doped side arsenic (As) was implanted with the concentration of $10^{20} cm^{-3}$. For p-doped area the same concentration of B was used. After that cobalt silicide was introduced in the windows on the highly doped stripes that created conducting interface to the contact vias. Then the layer of oxide were deposited on the wafers. In the following step small holes for contact plugs were etched through the oxide to the silicided areas. They were filled with a metal compound, planarized to the level of oxide to be covered with a metal layer. In the last step the metal layer was placed and patterned. As a result the metal

3.3. CHARACTERIZATION OF FABRICATED NONLINEAR WAVEGUIDES

pads at the top of the sample had a sufficient contact with the buried p-i-n diode lateral to the waveguide.

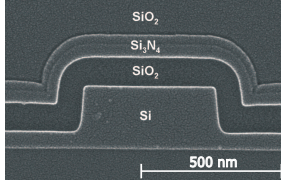


Figure 3.5: SEM cross-section of the waveguide with covering dielectric layers

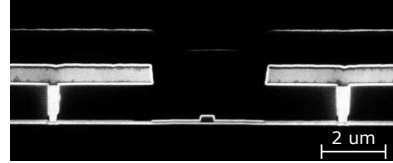


Figure 3.6: SEM cross-section with contact pads

Figure 3.5 depicts the cross-section of the realized SOI nano-rib waveguide made with the scanning electron microscope (SEM). The dielectric layers of 100 nm thick SiO₂ and 90 nm thick Si₃N₄ can be observed. They can substantially influence dispersion properties of the nano-rib waveguide (as shown in section 2.2.3). As it was already calculated and plotted in Figure 2.13, the nitride cladding promotes normal dispersion in the small silicon nano-rib waveguides with the rib height of 220 nm. Figure 3.6 shows the waveguide cross-section with the contact vias. Placed on both sides of the waveguide they connect the slab level with the metal stripes above. The metal lines are combined with the bigger metal pads. Consequently, by applying the bias voltage, the free carriers were swept away from the waveguide rib.

Potential improvements could be obtained by reduction of the roughness of the waveguide sidewalls and optimization of the waveguide geometry. A well controlled process for realization of the electrical contacts can enhance the carrier removal efficiency.

3.3 Characterization of fabricated nonlinear waveguides

This section presents electrical and optical measurements of the fabricated samples. The measurement setups are described followed by the results. Firstly, the electrical and opto-electrical characteristics of the p-i-n diode are measured (section 3.3.1). Dispersion measurements examine the possibility to obtain anomalous dispersion in the nano-rib waveguides with the lateral p-i-n diode (section 3.3.2). In section 3.3.3 the characteristics of

the linear optical loss versus wavelength are determined. Later, it is verified if the change in the linear optical loss varies with the change in the bias voltage applied to the p-i-n diode lateral to the waveguide (section 3.3.4). This provides an additional analysis of the influence of the lateral p-i-n diode on the wave propagation in the waveguide. The measurement of the power dependent loss originating from the two-photon absorption TPA and TPA induced free-carriers absorption FCA is reported in section 3.3.5. Moreover, the CW four wave mixing measurements are described in section 3.3.6. In section 3.3.7 it was examined if it is possible to obtain the phase sensitive amplification in the silicon nano-rib waveguide with the lateral p-i-n diode around 1550 nm wavelength.

3.3.1 Electrical and opto-electrical characterization of waveguide based p-i-n diode

In this section the electrical and opto-electrical measurement of the current-voltage (I-V) characteristics of the p-i-n waveguide diode are presented. The electrical measurements provide values of the dark current level for the reverse bias up to 25 V. The opto-electrical measurements confirm the presence of the free carriers generated by the TPA (as given in eq. 1.30) as well as the enhancement of the current by the applied voltage.

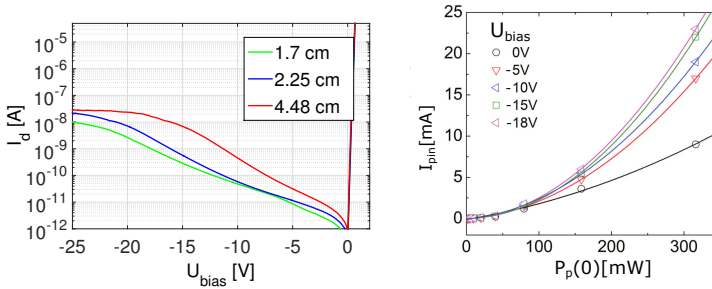


Figure 3.7: Electrical characteristics. Figure 3.8: Opto-electrical characteristics for different bias voltage. Diode current I_{pin} versus incident pump power $P_p(0)$ for $L_{wg} = 4.48$ cm, experimental data (symbols) and quadratic fit (lines) [78].

3.3. CHARACTERIZATION OF FABRICATED NONLINEAR WAVEGUIDES

The results were obtained using an electrical wafer probe station available at the IHP. Scanning the bias voltage in the range from -25 to 1 V, the dark current I_d of the diode was recorded. Figure 3.7 depicts the measured characteristics for the p-i-n diodes with lengths L_{wg} of 1.7 cm, 2.25 cm and 4.48 cm. It was observed that the dark current (I_d) increased with the increase of the waveguide's length from 1.7 cm to 4.48 cm. The highest value of I_d for the reverse bias $U_{bias} = -25$ V did not exceed $I_d = 20$ nA. This test provided also an information about the quality of the electrical contact while the diode was biased in the forward direction. Figure 3.8 depicts the characteristics of the current as function of the optical power incoupled to the waveguide $P_p(0)$. The quadratic behavior of the current (I_{pin}) confirms the dominant influence of the TPA generated carriers, as reported in [79].

3.3.2 Dispersion

A Mach-Zehnder Interferometer (MZI) structure was fabricated with a 0.5 mm long delay line in one arm. It was constructed on the same samples as the waveguides with the lateral p-i-n junction. The purpose of this structure was to characterize the dispersion of the waveguides. Waveguides with rib heights (H_{wg}) of 220 nm, 300 nm and 400 nm were manufactured. The slab height (s_{wg}) for the lowest waveguide was 50 nm and for the other two equal 80 nm. Two improvements were introduced. Firstly, the height of the waveguide's rib was increased to 400 nm, in order to obtain an anomalous dispersion. The second improvement was that in the case of the waveguides which were 300 nm and 400 nm high, the Si_3N_4 was substituted by SiO_2 in the area close to the waveguide rib. The measurements were performed using the setup depicted in the figure 3.11. The wavelength of the light incoupled to one input of the MZI was scanned in the range from 1510 nm to 1610 nm. Moreover, the output power was recorded at a single output in order to find the minima of the optical transmission characteristic. As result the free-spectral range was determined.

Figure 3.9(b) depicts the $\Delta\lambda_{FSR}$ values extracted from the spectral characteristics (figure 3.9(a)) as a function of the wavelength λ . The relation between free-spectral range $\Delta\lambda_{FSR}$ and the group index n_g is:

$$n_g(\lambda) = \frac{\lambda^2}{\Delta\lambda_{FSR} \cdot \Delta L} \quad (3.1)$$

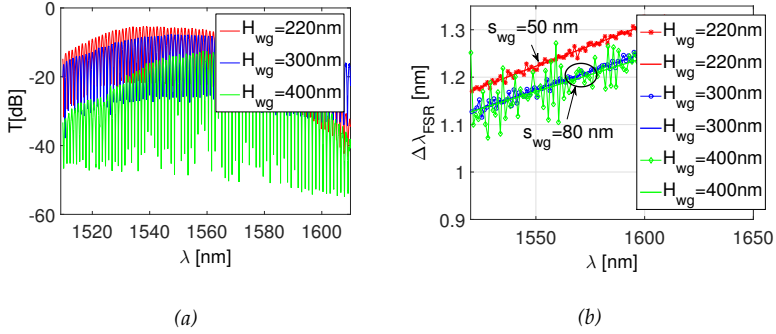


Figure 3.9: Measured transmission spectra (a) and extracted values (points with dashed lines) of $\Delta\lambda_{\text{FSR}}$ with linear fit (solid lines) (b) for MZI with delay line length $\Delta L = 0.5$ mm based on silicon nano-rib waveguide with rib heights $H_{\text{wg}} = 220, 300$ and 400 nm.

where λ is the central wavelength. The first order dispersion β_1 , second order dispersion β_2 and dispersion coefficient D were calculated using the equations (1.21-1.23)

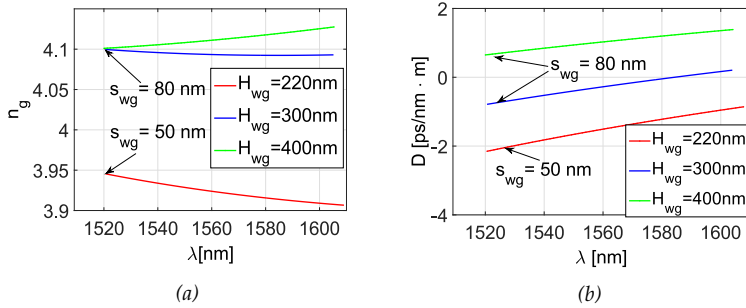


Figure 3.10: (a) Group index n_g and (b) dispersion coefficient D , for silicon nano-rib waveguide with rib heights H_{wg} of 220 nm, 300 nm and 400 nm, obtained from measurements.

Figure 3.10 presents the obtained experimental values of n_g and D . The normal material dispersion was successfully compensated with the enhancement of the waveguide rib height and substitution of the silicon ni-

tride cladding with oxide. Figure 3.10 presents a substantial change of the total dispersion versus wavelength.

The obtained values match those presented as a result of the theoretical research in figure 2.14. As expected, the positive value around $D=1 \text{ ps/nm} \cdot \text{m}$ was obtained for $\lambda = 1550 \text{ nm}$ when the $H_{\text{wg}} = 400 \text{ nm}$ and $s_{\text{wg}} = 80 \text{ nm}$. The subtle deviation of the measured D from the expected one may originate from the difference between the simulated and the real dimensions of the waveguide rib and the refractive indices of the cladding materials.

3.3.3 Linear loss

A virtual cutback loss measurement method was used to determine the waveguide loss. It relies on the transmission measurement of the waveguides with different lengths. The waveguides were placed on one sample close to each other. The same quality of the coupling from the fiber to the waveguides was assumed. The method delivers the average loss coefficient of the waveguides with the uncertainty from tenth to few dB per cm [47]. The high uncertainty in the determined loss values arises from the uncertainty in the fiber-waveguide-fiber coupling and the possible deviation between the waveguide structures. The measurements were realized in the scheme depicted in figure 3.11. The (Tunable Laser Source (TLS)) scanned the wavelength from 1520 nm to 1600 nm . The light polarization was optimized with the fiber polarization controller (Fiber Polarization Controller (FPC)) for the best incoupling to the Device Under Test (DUT). The grating couplers as designed allow the coupling of the TE polarized light. Standard single mode (SMF-8) fiber pigtails, which were placed on the nano-positioning stages, served the purpose of coupling of the light to the DUT via the fiber grating couplers. The output power was measured with the calibrated optical power meter (PWM). The Peltier element driven by the Temperature Controller (TEC) enabled the stabilization of the temperature. The scanning of the reverse bias voltage (DC) was performed, during the measurement of the waveguides with p-i-n junctions. Further the linear loss coefficient of the waveguide with and without the lateral p-i-n junction was determined. At the same time the fiber grating coupler spectral response was measured. Figure 3.12 depicts typical transmission measurement results of p-i-n waveguides. The 1dB bandwidth of the grating coupler was 15 nm . In Figure 3.13 the procedure of the propagation and coupling loss determination is shown. First the maxima of the

transmission curves are plotted corresponding to the length of the waveguides. Then the linear fit procedure was conducted. The slope of the line represents a loss of 2.5 dB/cm and 1.8 dB/cm for the waveguides with (at $U_{bias} = 0V$) and without p-i-n junction respectively. The crossing with the vertical axis (T) at -6.0 dB corresponds to the coupling loss of both in- and out-coupling grating (3.0 dB/coupler). The higher loss of the p-i-n doped waveguide shall be explained in more detail in section 3.3.4

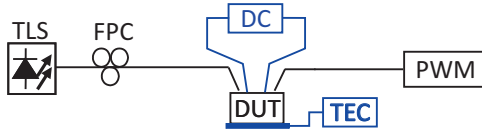


Figure 3.11: Scheme of the linear loss measurement setup with temperature control and bias voltage supply

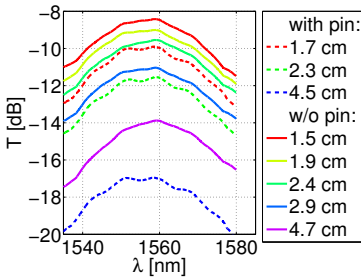


Figure 3.12: Transmission (fiber-chip-fiber) spectrum of the waveguides with lateral p-i-n junction and without different lengths L_{wg} . $W_{wg}=500$ nm, $H_{wg}=220$ nm, $s_{wg}=50$ nm. No voltage applied.

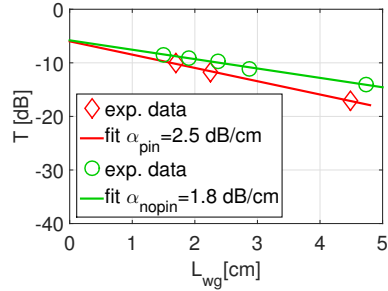


Figure 3.13: Transmission (fiber-chip-fiber) of waveguides with p-i-n (subscript pin) and without (subscript nopin) versus length L_{wg} .

3.3.4 Linear loss dependence on bias voltage in p-i-n waveguides

The measurements described in section 3.3.3 were followed by the tests of the linear loss dependence on the reverse bias voltage U_{bias} . In the wave-

3.3. CHARACTERIZATION OF FABRICATED NONLINEAR WAVEGUIDES

guide rib region the concentration of the minority free carriers nominally amounts to 10^{15} cm^{-3} . It was estimated from the resistivity values provided by the manufacturer of the wafers, and should be negligible for the waveguide's propagation loss (see section 2.1.1). Hence, the bulk linear loss shall not change substantially with the reverse voltage applied to the p and n regions. A change in the transmission with the reverse bias voltage can be caused by two effects. The excess loss can be introduced by p and n doped regions, if they overlap with the mode of the propagating wave, as already described in section 2.2. The second reason of the loss increase could be an inappropriate waveguide surface passivation. Thus the free carriers accumulate at the Si/SiO_2 interface, which was reported by Alloati et al. in [80]. The authors discovered that the free carriers at the waveguide surface introduced excess propagation loss as high as 1.8 dB/cm. In this thesis the result of the characterization of the optical loss of the waveguides versus the bias voltage of the p-i-n diode did not definitely determine the origin of the carriers. However, with the increase of the reverse bias voltage the transmission loss decreased.

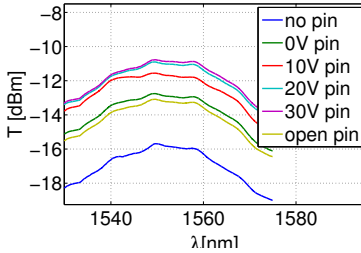


Figure 3.14: Transmission (fiber-chip-fiber) spectrum for different V_{bias} for $L=4.48 \text{ cm}$.

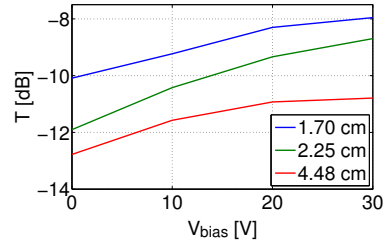


Figure 3.15: Transmission (fiber-chip-fiber) vs reverse bias voltage for 1.7, 2.25 and 4.48 cm long p-i-n nano-rib waveguides at $\lambda = 1555 \text{ nm}$.

Figure 3.14 presents the change in the transmission of the 4.48 cm long waveguide. The transmission was measured over the wavelength range 1530-1570 nm. The lowest values of the transmission on this sample (different sample than measured in fig. 3.12) were observed for the waveguide without the p-i-n junction. The transmission was higher in the waveguide with the p-i-n junction, even without the contact to the voltage ("open pin" curve in figure 3.14). The transmission is increasing with the increase of the reverse bias voltage up to 20 V. Above 20 V almost no change was ob-

served. With the 20 V reverse bias voltage all the carriers are swept away from the waveguide rib region. With the increase to 30 V there is no change in the loss. Figure 3.15 presents the evolution of the loss with the changing bias voltage at the wavelength of 1550 nm for the three lengths of waveguides. The linear loss values obtained with the cutback method were decreased from 1.8 dB/cm to 0.8 dB/cm with the applied voltage of 20 V. The results obtained with the virtual cutback method were verified by the measurement with the optical frequency domain reflectometer (OFDR) (model OBR 5T-50, commercial product of Luna Inc.) [81,82]. The results obtained by the two methods prove to be consistent with each other. The Optical Frequency Domain Reflectometry (OFDR) measurement determines the loss coefficient independently of the incoupling efficiency, provided that there is at least -125 dBm back-scattered light amplitude from the end of the measured structure. The biggest advantage of this method over the virtual cutback method is that the loss is measured for the single particular waveguide.

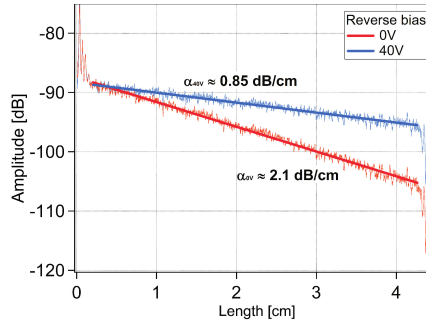


Figure 3.16: OFDR measurements on the 4.48cm long waveguide for different bias voltage. $W_{wg}=500$ nm, $H_{wg}=220$ nm, $s_{wg}=50$ nm.

Figure 3.16 confirms the previously determined decrease of the loss coefficient by more than 1 dB. This would suggest the average carriers concentration in the waveguide area of $N = 3 \cdot 10^{16} \text{ cm}^{-3}$. Applying the reverse bias voltage $U_{bias} = 40 \text{ V}$ to the structure did not indicate any breakdown effects and provided the lowest loss for the measured p-i-n waveguide.

3.3.5 Power dependent loss due to TPA and FCA

The power dependent loss in a silicon waveguide at the wavelength around 1550 nm originates from the two photon absorption (TPA) and the TPA induced free carrier absorption (FCA). Both absorption mechanisms have the detrimental impact on the nonlinear optical effects in a silicon waveguide. Therefore, their influence needs to be tested, quantified and minimized. The impact of the FCA effect can be treated as negligible until a certain power level. The results reported later in this section show these limits.

The experimental results discussed later leading to the determination of the β_{TPA} were provided by Edgar Krune (TUB). To quantify the TPA high peak power optical pulses were incoupled to the shallow etched waveguides with the length $L_{wg} = 1\text{ cm}, 3\text{ cm}$ and 6 cm . The waveguide width was $W_{wg} = 700\text{ nm}$, the height equals $H_{wg} = 220\text{ nm}$ and the slab thickness amounted to $s_{wg} = 150\text{ nm}$. The effective area $A_{eff} = 0.14\text{ }\mu\text{m}^2$, calculated with the JCMWave software, and the measured linear loss $\alpha_{lin} = 0.88\text{ dB/cm}$, were used in the calculations. Here the methodology applied to the measurement and the result evaluation followed the methodology of Claps et al. [83]. It was assured that the conditions were similar to those used by Claps et al. (e.g. pulses not longer than 1 ps , low repetition rate and optical intensity). To determine the TPA coefficient (β_{TPA}) the following formula was used (as in equation (1.37)):

$$\frac{P_{peak}(0)}{P_{peak}(L_{wg})} = e^{\alpha_{lin} L_{wg}} \left(1 + \frac{\beta_{TPA} L_{eff}}{A_{eff}} P_{peak}(0) \right) \quad (3.2)$$

hence:

$$\beta_{TPA} = -\frac{c_1 A_{eff}}{L_{eff}} e^{-\alpha_{lin} L_{wg}} \quad (3.3)$$

where A_{eff} represents the effective nonlinear area as defined in section 1.2.5 and $L_{eff} = ((1 - \exp(-\alpha_{lin} L_{wg}))/\alpha_{lin})$ is the effective length. The coefficient c_1 is the slope of the curve $P_{peak}(0)/P_{peak}(L_{wg})$ versus $P(0)_{peak}$, plotted in figure 3.18. The linear loss coefficient α_{lin} was measured in this case by the virtual cutback method, and L_{wg} is the physical waveguide length.

The measurement setup depicted in figure 3.17 was used to determine the TPA coefficient β_{TPA} . During the measurement the pulse of 80 fs was generated by a mode-locked laser with the repetition rate of 100 MHz. The

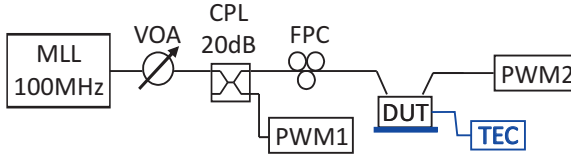


Figure 3.17: Measurement setup used to determine β_{TPA} with the mode locked pulsed pump laser.

pulse was attenuated by the Variable Optical Attenuator (VOA) and propagates in 99% through the 20 dB splitter. Furthermore the polarization of the signal was adjusted with the FPC to obtain the optimal incoupling to the waveguide. The pulse incoupled to the waveguide, broadened to 130 fs due to the limited bandwidth of fiber grating couplers. Propagating through the waveguide, the pulse induced the TPA effect and $P(L_{wg})$ was outcoupled to the power meter PWM2. The temperature of the sample was stabilized at 25 °C with the Peltier element driven by the temperature controller (TEC). The input power ($P(0)$) was monitored by the power meter PWM1.

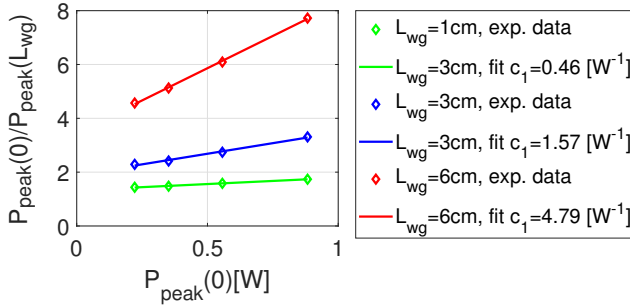


Figure 3.18: Resulting inverse transmission versus input pump peak power (points). The β_{TPA} from the linear fitting of the data according to formula 3.3. Waveguide without p-i-n diode.

The ratio of the pulse peak power at the input $P_{peak}(0)$ and the output $P_{peak}(L_{wg})$ are plotted in figure 3.18 as a function of $P_{peak}(0)$. When fitting the experimentally determined points with the line, the coefficient c_1 [1/W] was determined for each of the three waveguide lengths, with the formula 3.3. The β_{TPA} for all three waveguides amounts to

3.3. CHARACTERIZATION OF FABRICATED NONLINEAR WAVEGUIDES

$$(5.6 \pm 1.0) \cdot 10^{-10} \text{ cm/W}.$$

Moreover, it was determined how the power dependent loss of the waveguide with the lateral p-i-n diode in the CW mode varies with the change of the incoupled power and the reverse bias voltage. The effective carrier lifetime (τ_{eff}) was estimated applying the model presented in subsection 2.2.5 and in [37, 38]. The following parameters were used for calculations: the effective nonlinear area $A_{\text{eff}} = 0.1 \mu\text{m}^2$ (waveguide with $W_{\text{wg}} = 500 \text{ nm}$, $H_{\text{wg}} = 220 \text{ nm}$, $s_{\text{wg}} = 50 \text{ nm}$), $w_i = 1.2 \mu\text{m}$), $\beta_{\text{TPA}} = 5.6 \cdot 10^{-10} \text{ cm/W}$. The coupling efficiency and the waveguide loss of the sample were characterized with the virtual cutback method. The incoupling efficiencies were 4.2 dB/coupler and 3.6 dB/coupler, for 2.25 cm and 4.48 cm long waveguides respectively. The linear waveguide loss coefficient, determined without the applied bias voltage, totaled $\alpha_{\text{lin}} = 2.3 \text{ dB/cm}$ for both waveguides. In the following chapter this sample is referred to as sample 3.

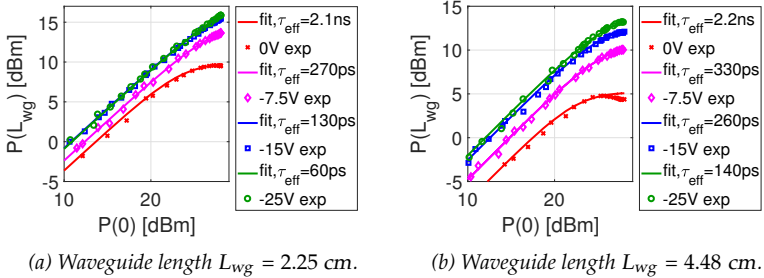


Figure 3.19: Continuous wave (CW) output power $P(L_{\text{wg}})$ versus input power $P(0)$. Fitting of the model developed in section 1.2.9 to the experimental data.

Figure 3.19 depicts the dependence of the output power on the input power (at the beginning of the waveguide). It was observed that the linear loss decreases with the increase of the reverse bias voltage applied to the sample. Moreover, the increase in the reverse bias voltage results in a lower saturation of the $P(L_{\text{wg}})$ for the higher values of $P(0)$. The vertical shift of the characteristics with the increase of the reverse bias voltage (U_{bias}) originates from the presence of the free carriers in the waveguide area (as discussed in section 3.3.4). The free carriers are not related to the TPA and contribute to the linear loss of the waveguide. An electric field, introduced by the bias voltage, sweeps out the carriers, and thus

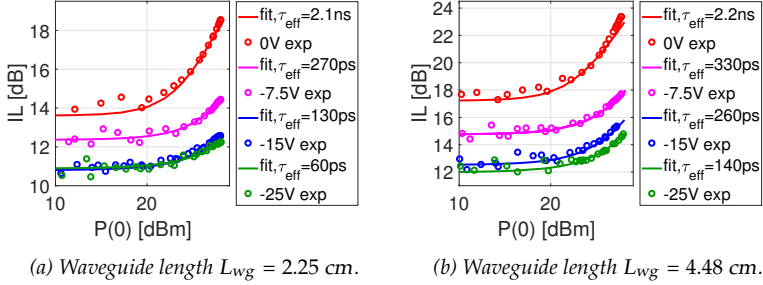


Figure 3.20: Insertion loss (IL) versus input power $P(0)$ (after grating coupler). Fitting of the developed model in section 1.2.9 to the experimental data.

lowers the waveguide loss. For the higher input power $P(0)$, TPA and TPA induced FCA cause a power depletion. For 0 V bias voltage the power depletion results in the saturation of the output power $P(L_{wg})$ at 10 dBm in the shorter waveguide ($L_{wg} = 2.25$ cm). In the longer waveguide ($L_{wg} = 4.48$ cm) the inflection can be observed. For both waveguides the carrier lifetime is similar in the case of the junction built-in field (0 V). However, the input power versus insertion loss characteristic for the 4.48 cm long waveguide suffers more from the carrier screening at about 28 dBm. Increasing voltage, as expected, caused the free carrier lifetime shortening and thus the FCA decrease. Both are depicted in figure 3.20.

When comparing values of $\tau_{eff} = 12$ ps as published in [38] and obtained within this work $\tau_{eff} = 130$ ps a few differences shall be mentioned. In [38] the authors describe the pulsed pump experiment with a pulse length of 9.1 ps, repetition rate of 38 MHz and an average power of 0.5 mW (peak power 2.9 W). The free carriers screening was avoided by using the low average power. In the case of the high power CW operation the accumulated free carriers screen the electric field (induced by the applied voltage U_{bias}) and thus the effective free carrier lifetime in the waveguide τ_{eff} increases. This is clearly visible on the characteristic at the 0 V bias voltage in figure 3.19(b), that for the high $P(0)$ the $P(L_{wg})$ is not only saturated but even decreases. There is no clear explanation about the origin of this high difference. It may result from the imperfections in the biasing structures, which would be suggested by an increase in the lifetime with the length of the waveguide. There may be other reasons, that were not taken into account in the simulations. The CW measurement results presented in this

3.3. CHARACTERIZATION OF FABRICATED NONLINEAR WAVEGUIDES

section were obtained from only two waveguides, due to the complexity of the setup and the limited time for the basic characterization. Therefore no systematic analysis based on a large number of measurements on many samples was possible. Nevertheless, the results are a good base for the calculations and the discussion about the particular samples in the following sections. The detrimental effect of the free carriers screening can be moved towards higher input power levels by the use of the waveguides with the thicker slab (see figure 2.41, 2.42). However, in these waveguides the bandwidth of the FWM wavelength conversion is limited by the normal dispersion (as shown in figure 2.14). There is a discrepancy between the τ_{eff} determined in the electrical simulations and resulting from the fitting curves of the optical measurement of samples. It may origin from the fact that the influence of the structure's length on the bias and the changes in the waveguide along the structure (tapering waveguide from grating coupler to the waveguide) were not taken into account there. It shall be noticed that no direct (pump-probe) measurement of the free carrier life-time was performed in this work.

3.3.6 Continuous-wave four-wave mixing experiments

This subsection describes in detail the results obtained from the measurements of the CW pump degenerated four wave mixing (FWM) wavelength conversion efficiency for the wavelengths around 1550 nm (as shown in figure 1.2(b) and 2.20). For convenience these figures are repeated in this section.

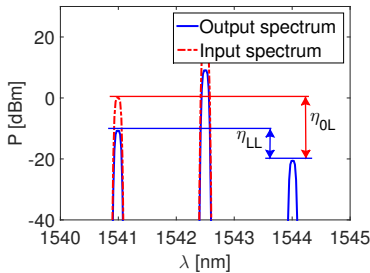


Figure 3.21: Input and output spectrum with the η_{OL} and η_{LL} .

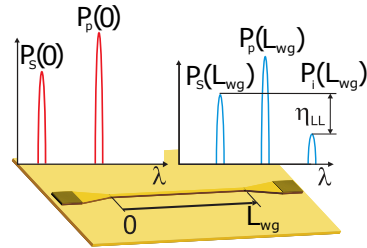


Figure 3.22: Scheme of η_{LL} determination

Part of the results were already published in [43, 58, 61]. By default the

beginning of the waveguide is defined in the position 0 and the end of the waveguide in the position L_{wg} , as depicted in figure 3.22. This is the case unless the contrary is explicitly mentioned. Furthermore, the dependence of the wavelength conversion on the following factors was examined:

- the waveguide length L_{wg} ,
- the presence of the lateral p-i-n diode,
- the detuning of the signal from the pump wavelength ($\Delta\lambda$),
- the reverse bias voltage applied (U_{bias}),
- and the incoupled pump power at the beginning of the waveguide ($P_p(0)$).

For this purpose two setups were built and several experiments were performed. Three samples were fabricated in the same production process. They had the same design and were constructed on the same type of SOI wafer. These samples were used in the experiments. It must be noted that the samples are not identical. There may be differences in their properties such as: waveguide loss, incoupling efficiency and the maximum reverse bias voltage. These differences may originate from the deviation in the fabrication process steps. In the first experiment session the samples 1 and 2 were used. The sample 3 was subject to the second measurement session. Samples 1 and 3 originate from the same wafer, whereas the sample 2 comes from the another wafer. Each sample contains waveguides with and without lateral p-i-n junction. The first results were obtained by measuring the waveguides with and without the lateral p-i-n junction on sample 1. Some of the grating couplers experienced a spot burning when exposed to the high intensity laser beam (10^6 W/cm^2). Therefore, for the next measurements sample 2 was used. The problem of the spot burning appeared firstly, due to a short, high power pulses generated by an Erbium Doped Fiber Amplifier (EDFA) during the electrical tuning of the output power. The other reason was dust or defects laying over or on the top of the grating coupler area.

The setup of the first measurement is presented in figure 3.23. Two tunable laser sources (TLS) were used. The first TLS emitted the signal light and was connected to one arm of the Fiber Optic Coupler (CPL)1. The light from the second TLS was amplified by EDFA (marked as pump laser in figure 3.23). The power of the pump was tuned with the mechanical variable optical attenuator (VOA). The pump laser was attached to the second

3.3. CHARACTERIZATION OF FABRICATED NONLINEAR WAVEGUIDES

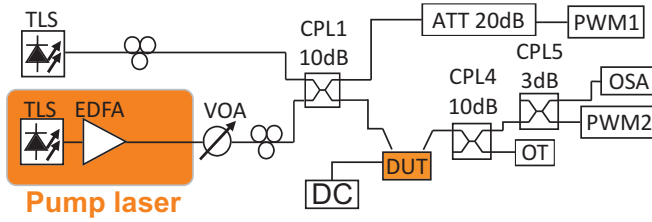


Figure 3.23: Scheme of the first setup for CW FWM measurement in Si waveguides. Realized in cooperation with Fraunhofer HHI in Berlin

arm of the CPL1. The polarization of both the pump and the signal waves was optimized, using fiber optic polarization controller (FPC), in order to obtain quasi-TE mode and thus maximal incoupling through the grating coupler. The fiber coupler CPL1 combined the 10 dB attenuated signal and the 1 dB attenuated pump power in the arm guiding to the DUT input. In the second arm of the fiber coupler CPL1 combined were the 10 dB attenuated pump power and the signal power decreased by 1 dB. Then the pump and the signal power were further attenuated by the 20 dB attenuator (ATT 20 dB) and were detected by the power meter PWM1. The output spectrum was attenuated by 10 dB (coupler CPL4) and further by 3 dB (coupler CPL5) and then delivered to the Optical Spectrum Analyzer (OSA) and the power meter PWM2. The high transmission output of the CPL4 was connected to the optical termination (OT). It must be underlined, that the setup did not allow to record neither the input signal power nor the input spectra. Therefore, the conversion efficiency η_{0L} (as defined in section 2.3) could not be reliably determined from the measured results. This measurement setup was used for the very first characterization of the degenerated CW FWM in the silicon waveguides. Firstly, the wavelength conversion was measured in waveguides without junction 1.5 cm, 1.9 cm and 4.74 cm long waveguides, and in p-i-n diode assisted waveguides with lengths 1.7 cm, 2.25 cm and 4.48 cm. The pump and signal wavelengths were set to $\lambda_p = 1552.5 \text{ nm}$ and $\lambda_s = 1550 \text{ nm}$ respectively. Then the influence of the reverse bias voltage (U_{bias}) on the wavelength conversion efficiency η_{LL} (as described in section 2.3) was measured. In the last experiment of the first measurement session, the wavelength of the signal wave was detuned from the λ_p in the range from 1 nm to 11 nm, for the three pump wavelengths (λ_p) of 1542 nm, 1552.5 nm and 1562 nm.

Figure 3.24 depicts the change of the output power of the pump $P_p(L_{wg})$,

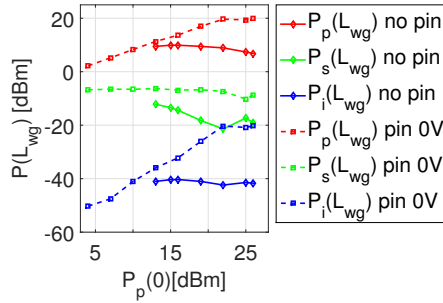


Figure 3.24: Output power of pump, signal and idler for two waveguides: waveguide without p - i - n junction and length of 1.7 cm (solid, no pin) and waveguide with the 0 V reverse biased lateral p - i - n diode and length 1.52 cm (dashed, with pin).

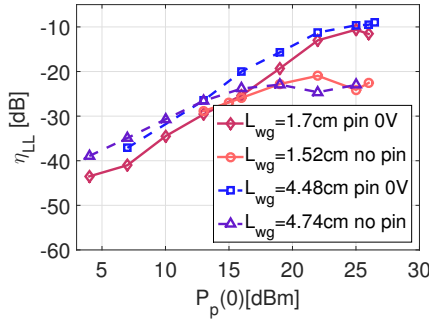


Figure 3.25: Conversion efficiency η_{LL} versus $P_p(0)$ for four waveguides: two waveguides without the p - i - n junction and the lengths of 1.52 cm (circles) and of 4.74 cm (triangles); two waveguides with the 0 V biased p - i - n diode and the lengths of 1.7 cm (diamonds) and 4.48 cm (squares).

signal $P_s(L_{wg})$ and idler $P_i(L_{wg})$ in two waveguides. The first one is the 1.52 cm long waveguide without p - i - n junction (referred to as no pin). The second is the 1.7 cm long waveguide with the p - i - n diode (marked as pin). To the second waveguide the 0 V bias voltage was applied from the power supply. An increase in the pump power above 12 dBm, incoupled to the first waveguide, resulted in the rising nonlinear loss, and thus in the depletion of the pump (P_p) and the signal power P_s . The measured output

3.3. CHARACTERIZATION OF FABRICATED NONLINEAR WAVEGUIDES

idler power (P_i) remained constant. The electric field induced solely by the p-i-n junction caused the shift of the saturation point of the output pump. For this waveguide the output pump power saturated at the input pump power $P_p(0) = 21.5 \text{ dBm}$. Figure 3.25 shows the wavelength conversion efficiency η_{LL} , as a function of the input power, for the doped waveguide(with p-i-n junction) and undoped waveguides (without p-i-n junction). Over 10 dB enhancement in η_{LL} can be observed, resulting only from the presence of the lateral p-i-n diode, for the similar waveguides lengths. The change of the waveguide length (L_{wg}) does not influence the conversion efficiency, which indicates that the effective length L_{eff} of the waveguide is shorter or equals 1.52 cm.

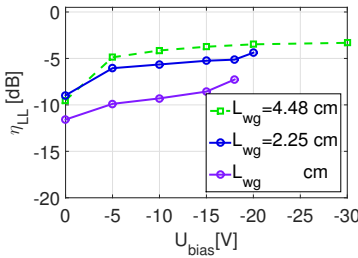


Figure 3.26: Conversion efficiency η_{LL} for L_{wg} of 1.7 cm, 2.25 cm and 4.48 cm, $P_p(0) = 26 \text{ dBm}$, $\lambda_p = 1552.5 \text{ nm}$, $\lambda_s = 1550 \text{ nm}$

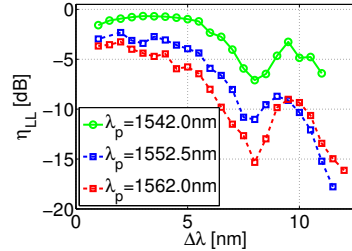


Figure 3.27: Conversion efficiency η_{LL} for three pump wavelengths versus signal detuning $\Delta\lambda$. $P_p(0) = 26 \text{ dBm}$, $L_{wg} = 4.48 \text{ cm}$, $U_{bias} = 30 \text{ V}$.

Figure 3.26 presents the measurement results of η_{LL} at the incoupled pump power $P_p(0) = 26 \text{ dBm}$, the wavelength of the pump $\lambda_p = 1552.5 \text{ nm}$ and of the signal $\lambda_s = 1550 \text{ nm}$. The increased conversion efficiency was noticed in this case. For the longest waveguide of $L_{wg} = 4.48 \text{ cm}$ the saturation of η_{LL} takes place at the bias voltage $U_{bias} = -20 \text{ V}$. This effect can be related to the fact that the maximum possible carriers velocity was obtained and thus the loss was minimized (see the saturation of the carrier lifetime at -30 V in figure 2.39).

Figure 3.27 shows how the conversion efficiency η_{LL} varies with the detuning between the pump wavelength and the signal wavelength $\Delta\lambda$ (hereinafter 'detuning') for three different pump wavelengths. The highest value of the $\eta_{LL} = -0.7 \text{ dB}$ was observed at the pump wavelength $\lambda_p = 1542 \text{ nm}$ when the detuning $\Delta\lambda = 3 \text{ nm}$. This is to date the highest value of η_{LL} re-

ported in the silicon waveguides for the wavelengths around 1550 nm. The conversion efficiency values η_{LL} of 2.5 and 3.3 dB were obtained for the remaining pump wavelengths of 1552 and 1562 nm, respectively. The conversion efficiency spectrum is symmetric with respect to the pump wavelength. Therefore, only the detuning towards longer wavelengths was measured. In these measurements it was determined that the 3 dB bandwidth of the conversion efficiency amounted to 12 nm. This is confirmed later in this section.

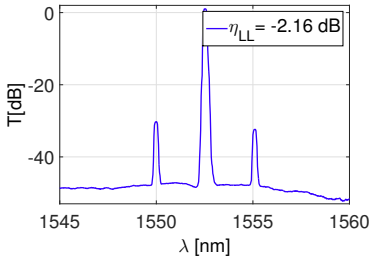


Figure 3.28: Output spectrum recorded by OSA for the waveguide of length $L_{wg} = 4.48$ cm, $P_p(0) = 26.5$ dBm, $\lambda_p = 1552.5$ nm, $\lambda_s = 1550$ nm, $U_{bias} = -20$ V.

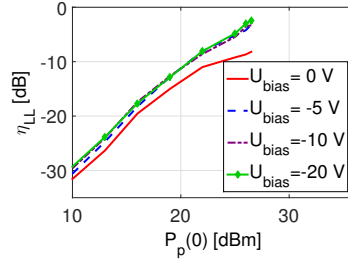


Figure 3.29: Dependence of the η_{LL} on $P_p(0)$ for several reverse U_{bias} values, $\lambda_p = 1552.5$ nm, $\lambda_s = 1550$ nm, $L_{wg} = 4.48$ cm.

Figure 3.28 shows the output spectrum recorded by an optical spectrum analyzer (OSA) for the pump power $P_p(0) = 26.5$ dBm. This corresponds to the pump power of 31 dBm before the grating coupler. In this case the pump wavelength equaled $\lambda_p = 1552.5$ nm and the signal wavelength equaled $\lambda_s = 1550$ nm. The conversion efficiency obtained with the 4.48 cm long p-i-n waveguide reached $\eta_{LL} = -2.16$ dB while the reverse bias voltage (U_{bias}) reached -20 V. To avoid destruction of the grating couplers the later measurements were performed for lower powers at the grating coupler.

The influence of the bias voltage on η_{LL} is depicted in figure 3.29. The highest increase of the conversion efficiency η_{LL} was observed with the change of the bias voltage from 0 V to 5 V. It was noted, however, that the conversion efficiency did not saturate for the applied pump power levels. This indicates that even a higher pump power could be used.

Furthermore, the η_{LL} values in relation to the incoupled pump power were

3.3. CHARACTERIZATION OF FABRICATED NONLINEAR WAVEGUIDES

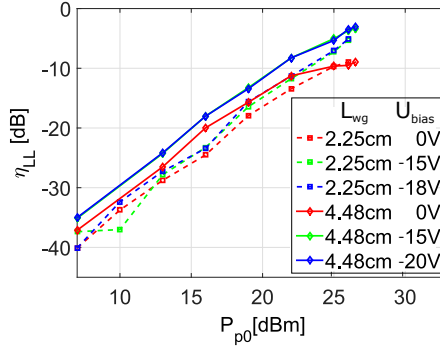


Figure 3.30: Comparison of η_{LL} relation to incoupled pump power $P_p(0)$ for 2.25 cm and 4.48 cm long waveguide for three bias voltage levels. $\lambda_p = 1552.5\text{nm}$, $\lambda_s = 1550\text{nm}$.

compared for two waveguide lengths (2.25 cm and 4.48 cm) and for three bias voltage levels. The pump wavelength equaled 1552.5 and the signal wavelength amounted to 1550 nm, hence the detuning totals 2.5 nm. The results of this comparison are depicted in figure 3.30. The conversion efficiency increases with the length of the waveguide, when a bias voltage over 15 V is applied. It saturates, however, at the level of -10 dB when the applied reverse bias voltage is 0 V, independently of the waveguide's length. This indicates that the electric field, built in by the doping regions, is not enough to allow for a removal of the generated free carriers (compare also figure 2.39).

The second setup (figure 3.31) for the nonlinear p-i-n nano-rib waveguides FWM characterization was built at the Technical University of Denmark (DTU) in Copenhagen and automated in order to record the conversion efficiency spectra. In the measurements performed with this setup the pump power before the grating coupler did not exceed 28 dBm (corresponding to 23.5 dBm in the waveguide) to prevent the grating coupler from burning. In this case the temperature could not be controlled with TEC like in the first setup (figure 3.23). On the other hand the second setup allowed to record faster the output powers of the pump, the signal and the idler as well as the input power of the signal and the pump.

As in the first measurement setup (see figure 3.23) also here two tunable laser sources (TLS) were used and on the signal arm the TLS was followed

by a fiber polarization controller (FPC). As in the first setup also here the second input arm delivered a pump wave from a TLS, amplified by an erbium doped amplifier (EDFA). Nevertheless, here the optical band pass filter (Optical Band-Pass Filter (OBPF)) attenuated the unwanted part of EDFA spectrum from the pump wavelength. Then the variable optical attenuator VOA was used to ensure a continuous change of the pump power without an overshoot of the light power. The (FPC) at the second arm provides the optimal polarization for a grating coupler of a waveguide. The two arms are connected via the 10 dB fiber optic coupler (CPL1) and so the pump wave and the signal wave are combined in one fiber.

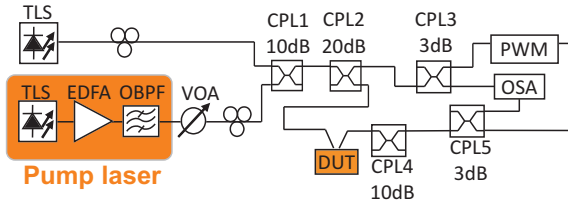


Figure 3.31: Second measurement setup for CW FWM measurement in Si waveguides. Realized in cooperation with the group at DTU.

The coupler CPL2 tapped off 1% of the light power, which was then then split by the 3dB-coupler CPL3 to the optical power meter (PWM) and an optical spectrum analyzer (OSA). Thus the optical power and spectra at the input of the waveguide is measured. The remaining 99% was routed to the device under test DUT. The light coupled out from DUT was attenuated by the 10 dB-coupler CPL4 and then split with the 3dB-coupler CPL5 to the optical power meter (PWM) and the (OSA). The output spectrum from the OSA allowed to measure the conversion efficiency η_{LL} . Measuring the power at the input and the output, gave the value of the total loss of the sample. In the case of the p-i-n diode assisted waveguide the bias voltage from the voltage source was connected with the probe needles. **The setup served also to determine the nonlinear loss of the waveguides. These results were already reported in section 3.3.5.**

At first the FWM wavelength conversion spectra were recorded. The wavelength of the pump was set $\lambda_p = 1552.5$ nm. The signal wavelength λ_s was scanned from 1535 nm to 1570 nm. For each λ_s the value of the optical power of the idler wave was measured at the wavelength λ_i . Using this method the spectra of the wavelength conversion efficiencies η_{OL} and η_{LL} were obtained. The value of the in and outcoupling loss

3.3. CHARACTERIZATION OF FABRICATED NONLINEAR WAVEGUIDES

$\alpha_{GRC} = -4.5$ dB/coupler (estimated from the cut-back measurement) introduced by the grating coupler was subtracted from the measured values of power. The noticeable difference in the incoupling as compared to the previous setup may originate from the difference in the applied coupling assembly. The setup input was calibrated until the fiber facet at the input of DUT and the output was calibrated from the outcoupling fiber facet with the flat power meter head.

The experiments were performed for the waveguides with the lateral p-i-n junction having the lengths L_{wg} of 1.7 cm, 2.25 cm and 4.48 cm. During the characterization of the waveguides we applied a different reverse bias voltage and varied the input pump power incoupled into the p-i-n diode assisted nano-rib waveguides.

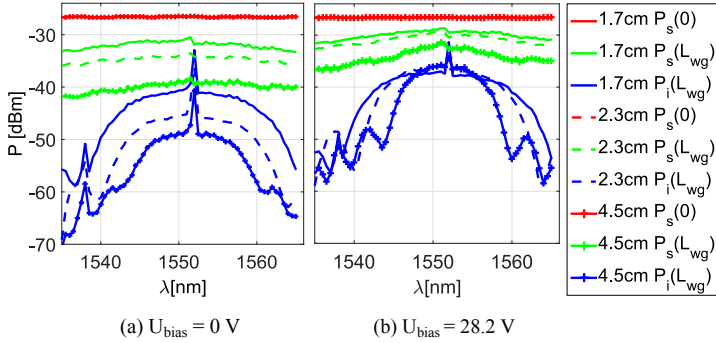


Figure 3.32: Measured power of signal at input $P_s(0)$ and output $P_s(L_{wg})$ and $P_i(L_{wg})$ idler versus wavelength of the input signal λ_s for $P_p(0) = 21.5$ dBm. The input signal was always the same, thus the signal curves overlap.

The measurements of the following quantities were performed: the power of the signal at the input of the waveguide $P_s(0)$, the power of the signal at the output of the waveguide $P_s(L_{wg})$ of the waveguide, the idler power at the output of the waveguide $P_i(L_{wg})$. The values were measured at the incoupled pump power $P_p(0) = 21.5$ dBm. The values at the reverse bias voltage U_{bias} of 0 V and 28.2 V are depicted in figures 3.32(a) and 3.32(b) respectively. The peak in the middle of the characteristics is caused by incomplete elimination of the pump power from the output measurement curves. For the bias voltage equaling 0 V several effects can be observed. For the same incoupled signal the output signals experience both linear and nonlinear effects. The highest absolute idler power can be observed

for the shortest waveguide. For the the longer waveguides the idler power decreases. However, the distance between the green (power of the signal at the output) and the corresponding blue curve remains the same for each waveguide. This results in the same η_{LL} for all lengths, while the highest value of η_{0L} was observed for the 1.7 cm long waveguide. Increasing the length of the waveguide L_{wg} diminishes the bandwidth of the wavelength conversion. It results from the fact that all three waveguides have a high normal dispersion due to their dimensions $W_{wg} = 500 \text{ nm}$, $H_{wg} = 220 \text{ nm}$ and $s_{wg} = 50 \text{ nm}$. At the bias voltage of 0 V the shortest waveguide would be the best choice for the wavelength conversion's point of view. It is due to the highest conversion efficiency η_{0L} and the widest conversion efficiency bandwidth (BW).

However, the reverse biasing of the p-i-n diode with the 28.2 V voltage changes a situation. The longest waveguide ($L_{wg} = 4.48 \text{ cm}$) emitted 1 dB more maximal idler power than the shortest waveguide ($L_{wg} = 1.7 \text{ cm}$). Despite the highest idler power obtained in the 4.48 cm long waveguide, the disadvantageous narrow bandwidth remains. The result shows that for the normal dispersion the FWM wavelength conversion efficiency bandwidth becomes narrower with the increase of the waveguide length. This situation would be even more disadvantageous in case of the shallow etched waveguides with the very low loss [52], since they have even higher normal dispersion. The very low loss of these waveguides would predestine them for the nonlinear optical applications. Nevertheless, their high normal dispersion and an effective area $A_{eff} = 0.14 \text{ } \mu\text{m}^2$, would limit the bandwidth and the FWM based wavelength conversion efficiency.

Figure 3.33 depicts the measured values of the η_{LL} (ratio of the output idler power to output signal power) and the η_{0L} (ratio of the output idler power to input signal power) for the pump power $P_p(0) = 21.5 \text{ dBm}$. The measured conversion efficiency is presented as the function of the wavelength of the input signal λ_s . The measurements were conducted for the waveguide lengths of 1.7 cm, 2.25 cm and 4.48 cm, whereas the bias voltage was 0 V. For the shortest and the longest waveguides similar values of η_{LL} were obtained. The η_{0L} (eq. (2.8)), however, shows the loss contribution of the waveguide. Therefore, the highest conversion efficiency η_{0L} was obtained for the 1.7 cm long waveguide. Applying the 28.2 V bias voltage, the conversion efficiency values (both η_{0L} and η_{LL}) became the highest in the longest waveguide. The optical loss due to the free carriers decreased, which led to an enhancement in η_{0L} by 3.2, 8.9 and 12.6 dB while η_{LL} was

3.3. CHARACTERIZATION OF FABRICATED NONLINEAR WAVEGUIDES

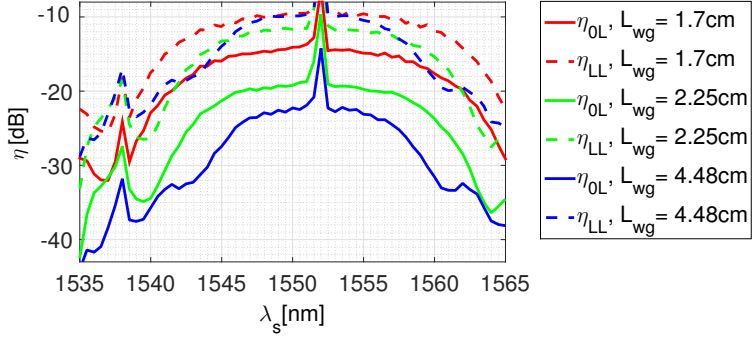


Figure 3.33: Measured conversion efficiency η_{OL} (solid) and η_{LL} (dashed) versus wavelength of the input signal λ_s for waveguide lengths 1.7 cm, 2.25 cm, 4.48 cm, pump wavelength $\lambda_p = 1552$ nm and $P_p(0) = 21.5$ dBm, $U_{bias} = 28.2$ V.

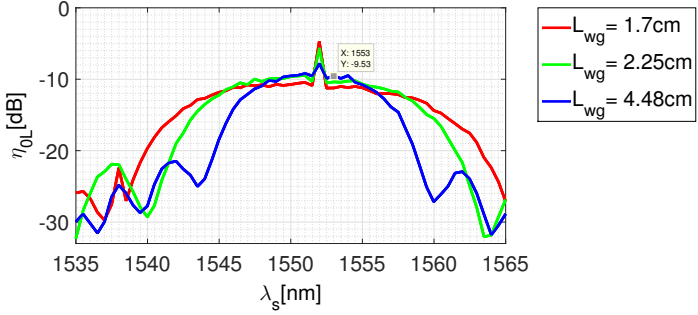


Figure 3.34: Measured conversion efficiency η_{OL} versus wavelength of the input signal λ_s , for waveguide lengths 1.7 cm, 2.25 cm, 4.48 cm, pump wavelength $\lambda_p = 1552$ nm and $P_p(0) = 21.5$ dBm, $U_{bias} = 28.2$ V.

enhanced by 1.48, 4.87, 5.9 dB for the waveguide lengths of 1.7 cm, 2.25 cm and 4.48 cm respectively. Please compare figure 3.33 with figures 3.34 and 3.35.

The decrease in the FCA increases the FWM conversion efficiency in the nano-rib waveguide with the lateral p-i-n diode. Three reverse bias voltage values U_{bias} of 0 V, 10 V and 20 V were applied to the 4.48 cm long waveguide, to quantify this effect. The input pump power incoupled to

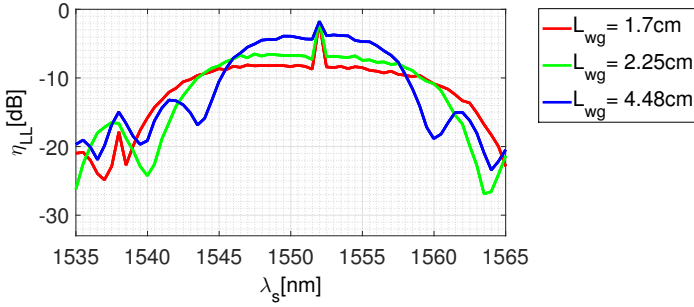


Figure 3.35: Measured conversion efficiency η_{LL} versus wavelength of the input signal λ_s , for waveguide lengths 1.7 cm, 2.25 cm and 4.48 cm, pump wavelength $\lambda_p = 1552$ nm, and $P_p(0) = 21.5$ dBm, $U_{bias} = 28.2$ V.

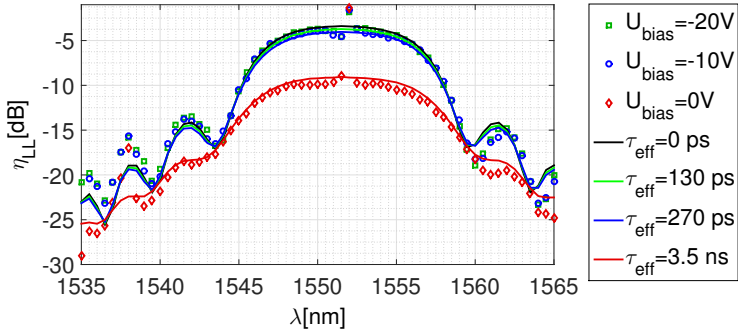


Figure 3.36: Experimentally determined η_{LL} versus λ_s variable U_{bias} (symbols) $L = 4.48$ cm, pump power $P_p(0) = 21.5$ dBm, and corresponding numerically determined characteristics for different free carrier lifetimes (solid curves). (Fit parameters $\gamma = 280$ [1/(W · m)], $\beta_{TPA} = 5.6 \cdot 10^{-10}$ cm/W, $A_{eff} = 0.1 \mu m^2$, $\alpha_{lin} = 1.2$ dB/cm)

the waveguide ($P_p(0)$) equalled 21.5 dBm. The output values of the pump power ($P_p(L_{wg})$), the signal power ($P_s(L_{wg})$) and the idler power ($P_i(L_{wg})$) were measured versus the signal wavelength (λ_s) at each of the reverse bias voltage levels (U_{bias}). The measurement results were used to calculate the following quantities: the conversion efficiency η_{LL} (ratio between the power values of the output idler and the output signal), the conversion

3.3. CHARACTERIZATION OF FABRICATED NONLINEAR WAVEGUIDES

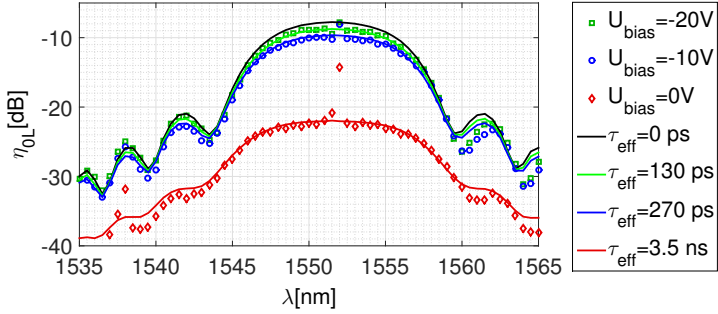


Figure 3.37: Experimentally determined η_{OL} versus λ_s variable U_{bias} (symbols) $L = 4.48$ cm, pump power $P_p(0)=21.5$ dBm, and corresponding simulated characteristics for different lifetimes (solid curves). (Fit parameters $\gamma = 280$ [1/(W · m)], $\beta_{TPA} = 5.6 \cdot 10^{-10}$ cm/W, $A_{eff} = 0.1 \mu m^2$, $\alpha_{lin} = 1.2$ dB/cm, $D = -1.9$ ps/(nm · m))

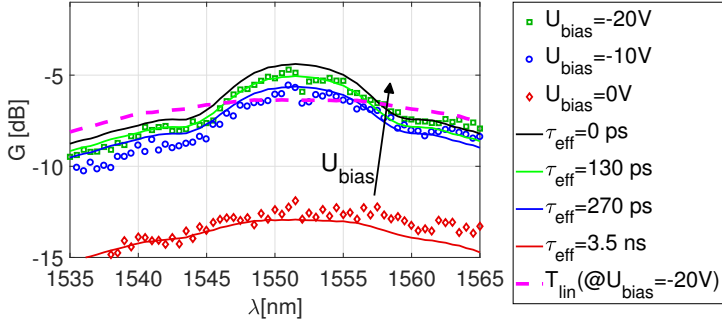


Figure 3.38: Measured nonlinear transmission G as a function of λ_s for variable U_{bias} (symbols) $L_{wg} = 4.48$ cm, pump power $P_p(0)=21.5$ dBm, and corresponding simulated characteristics for different effective lifetimes τ_{eff} (solid curves). Linear transmission curve (at $U_{bias} = -20$ V) was inserted (dashed) to indicate gain. (Fit parameters $\gamma = 280$ [1/(W · m)], $\beta_{TPA} = 5.6 \cdot 10^{-10}$ cm/W, $A_{eff} = 0.1 \mu m^2$, $\alpha_{lin} = 1.2$ dB/cm, $D = -1.9$ ps/(nm · m))

efficiency η_{OL} (ratio between the power values of the output idler and the input signal) and the gain G (ratio between the power values of the output

signal and the input signal) . The results of this test are illustrated in the figures 3.36, 3.37 and 3.38.

The model introduced in section 2.3 was used to generate the fitting curves. The following parameters were used: the TPA coefficient $\beta_{TPA} = 5.6 \cdot 10^{-10} \text{ cm/W}$, the nonlinear parameter $\gamma = 280 \text{ (W}^{-1} \cdot \text{m}^{-1}\text{)}$ and the linear propagation loss $\alpha_{lin} = 1.2 \text{ dB/cm}$. The curves, simulated with the model, fit to the obtained results, when for the applied reverse bias voltage levels of 0 V, 10 V and 20 V the set effective free carrier lifetime (τ_{eff}) equals 3500 ps, 270 ps and 130 ps, respectively. For reference the fitting curves using the effective free carrier lifetime $\tau_{eff} = 0$ were plotted. The obtained results indicate the shortening of the free carrier lifetime from 3.5 ns at 0 V bias voltage to 130 ps at 20 V bias voltage (explained in section 3.3.5). This allows for the $\eta_{0L} = -9 \text{ dB}$ at the input pump power $P_p(0) = 21.5 \text{ dB}$. The excessive loss of about 6 dB is observed when comparing linear transmission (Figure 3.38 dashed curve) curve to the gain (G) at $U_{bias} = 0 \text{ V}$ bias (Figure 3.38 red diamonds). This propagation loss comes from the free carriers present in the waveguide rib intrinsically (before TPA occurs) as well as generated by the high intensity pump wave (due to TPA). The noticeable on-off gain of more then 1 dB over the linear transmission indicates the compensation of the TPA loss by the gain of the signal. This was possible by applying the reverse bias voltage of 20 V. The experimentally achieved gain characteristics fit to the developed model.

As the next, it is shown how the characteristics of the conversion efficiency η_{LL} versus signal wavelength λ_s changes with the increase of the input pump power $P_p(0)$ for the waveguide with $L_{wg} = 4.48 \text{ cm}$. Two effects resulting from the increase in $P_p(0)$ were observed. Firstly, it was observed that the increase in the pump power leads to the saturation of the wavelength conversion efficiency η_{LL} . The growth of $P_p(0)$ by 3 dB from 15.5 dBm to 18.5 dBm resulted in a 6 dB enhancement of the conversion efficiency η_{LL} and the further doubling of the input power increased the η_{LL} only by 4 dB. Secondly, it was noticed from figure 3.36, that the bandwidth gets narrower by 1 nm with the increase of the input power from 14.5 dBm to 21.5 dBm.

In this section it was shown that the free carriers removal by the reversely biased p-i-n diode has a beneficial influence on the CW FWM wavelength conversion efficiency. Decrease in FCA was demonstrated for the low and high pump power incoupled to the waveguide. Nonlinear losses were quantified by correlation to the theoretical model. The experimentally obtained value of the two photon absorption coefficient $\beta_{TPA} = 5.6 \cdot$

3.3. CHARACTERIZATION OF FABRICATED NONLINEAR WAVEGUIDES

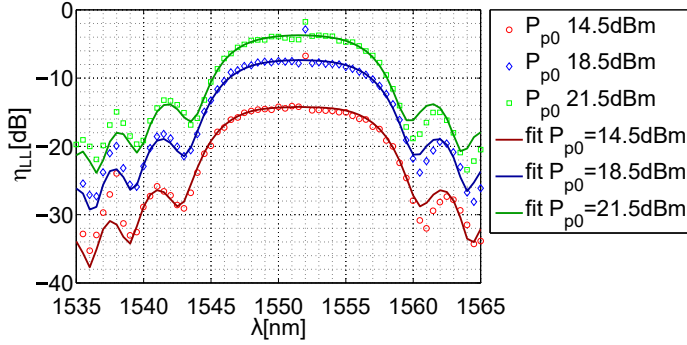


Figure 3.39: Conversion efficiency η_{LL} versus λ_s for various pump power $P_p(0)$, length $L_{wg}=4.48$ cm, $U_{bias}=-28.2$ V. Comparison of the experimental data(points) to the numerically obtained curves (solid line) for the same optical power. (Fit parameters $\gamma = 280$ $[1/(W \cdot m)]$, $A_{eff} = 0.1$ μm^2 , $\tau_{eff} = 130$ ps), $D = -1.9 ps/(nm \cdot m)$)

10^{-10} cm/W agrees with the reported by other research groups for the light polarized along [110] crystal direction [16,83]. The efficient mechanism of carriers removal enabled the wavelength conversion efficiency η_{LL} as high as -0.7 dB in the 4.48 cm long waveguides. This result was obtained at the input pump power $P_p(0)$ of 26 dBm. The conversion efficiency η_{0L} , was determined in the experiment, in which the input power was limited to $P_p(0) = 21.5$ dBm. Therefore the highest value of η_{0L} , which was obtained in the 4.48 long waveguide with p-i-n diode equals -9.5 dB.

3.3.7 Phase sensitive amplification measurement

Following the growing interest in the phase-sensitive all-optical signal regeneration [84] the phase sensitive amplification experiment was performed in order to evaluate silicon nano-rib waveguide as a potential candidate to replace highly nonlinear fiber in the phase regeneration device. The results presented here were obtained by joint measurement activities with DTU and were published in [44,45]. The characterization of the phase sensitive amplification in the silicon waveguides was performed using the setup depicted in figure 3.40.

A continuous wave signal was emitted at 1549.76 nm by a tunable, narrow

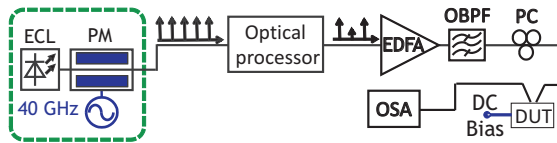


Figure 3.40: Measurement setup used to determine the phase sensitive gain in silicon waveguide

linewidth (~ 100 kHz) external cavity laser source (ECL). It was phase modulated (PM) with a 40-GHz radio frequency (RF) signal with a modulation index of 4.3 in order to generate an optical frequency comb with 40-GHz line spacing. The modulation index is defined as the ratio of the peak-to-peak voltage of the driving signal to the half-wave voltage of the phase modulator multiplied by $\pi/2$. An optical processor was used to select three neighboring comb lines: the outer ones act as pumps and the central one serves as signal. The pump power levels were equalized and the pump-to-signal power ratio was set to 30 dB in order to avoid the onset of saturation effects. The pumps and the signal were amplified with an erbium-doped fiber amplifier (EDFA) followed by an optical band-pass filter (0.8-nm full-width at half-maximum bandwidth) to suppress the out-of-band Amplified Spontaneous Emission (ASE) noise.

Three waves (two pumps and the signal in the middle) were injected into the waveguide through a vertical grating coupler after aligning their states-of-polarization to the TE mode of the device. A reverse-bias voltage of 20 V was applied to the p-i-n junction for free carrier removal. At the output of the waveguide, the signal power was measured using an optical spectrum analyzer (OSA) as the relative phase of the signal with respect to the phases of the pumps was changed using the optical processor. Figure 3.41 shows the input and the output spectra recorded for the minimum and the maximum gain in the 4.48 cm long p-i-n waveguide when applying the reverse bias voltage $U_{bias} = -20$ V. Comparing the output spectra for the maximum (constructive) and the minimum (destructive interference) signal power showed a 15.5-dB phase-sensitive extinction ratio (ER). To show how the PSA depends on the waveguide length, the following waveguides were tested: the 4.7 cm long waveguide without the lateral diode and three waveguides with the length of 1.7, 2.25 and 4.48 cm with the lateral p-i-n diode. In the experiment the two CW pumps were amplified to the total power of 24 dBm by EDFA. It resulted in the 16.5 dBm power per pump (19.5 dBm total pump power) in the waveguide due

3.3. CHARACTERIZATION OF FABRICATED NONLINEAR WAVEGUIDES

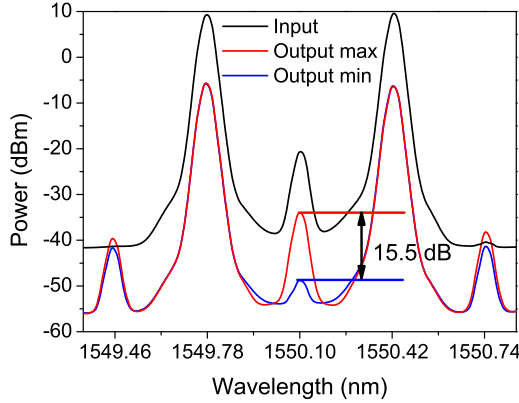


Figure 3.41: Spectra recorded at the input and output of the 4.48 cm long waveguide for maximum and minimum gain. The total power from two pumps $P_{p1}(0) + P_{p2}(0) = 19.5\text{dBm}$

to the fiber-to-grating incoupling loss of 4.5 dB at the angle of incidence $\text{AOI}=9^\circ$. Figure 3.41 presents the results of these measurements. In the waveguide without p-i-n diode the FCA and the TPA effects resulted in the 9 dB higher insertion loss (Insertion Loss (IL)) than in the waveguide with the comparable length and the p-i-n diode. This high loss diminished the PSA to the level of 0.5 dB. The PSA curves for all four waveguides are presented in figure 3.42. The PSA increased with the waveguide length to the maximum value of 15.5 dB for the 4.48 cm long waveguide with the p-i-n diode, when the reverse bias voltage of 20 V was applied.

In the next step the influence of increasing pump powers was tested on the 4.48 cm long p-i-n waveguide with $U_{\text{bias}} = -20\text{ V}$. The influence of the signal phase on the normalized output signal power is reported in figure 3.43 for total input power levels before the waveguide grating spanning from 24 dBm to 28 dBm corresponding to the effective powers coupled in the waveguide between 16.5 dBm and 20.5 dBm per pump. At highest input pump power (20.5 dBm per pump) the bias of 25 V was tested. As a consequence the 20 dB phase sensitive extinction ratio (ER) could be achieved, which is the best value for the CW PSA for 1550 nm wavelength

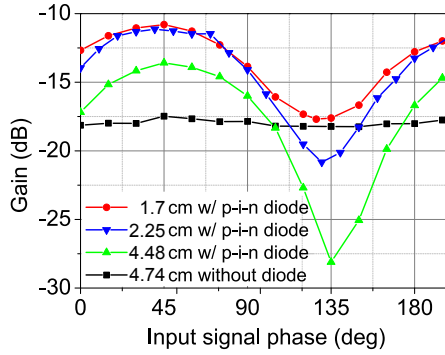


Figure 3.42: Phase sensitive amplification in 1.7, 2.25 and 4.48 cm long p-i-n diode waveguides and the reference waveguide without p-i-n diode with length of 4.74 cm. Total pump power 19.5 dBm

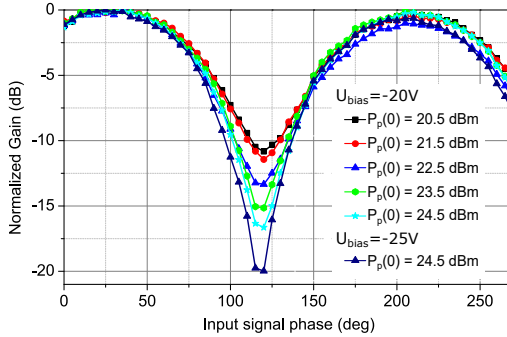


Figure 3.43: Phase sensitive amplification as a function of phase shift for different total pumps power after the grating coupler and bias of $U_{bias} = -20$ V. For the highest power voltage was increased to $U_{bias} = -25$ V. $L_{wg}=4.48$ cm.

being reported in silicon waveguides. For the time this is the best value of the CW PSA obtained in silicon waveguide.

Phase sensitive extinction ratio (ER) depicted in figure 3.43 is enhanced with the increasing pump power and applied reverse bias voltage. However, neither higher values of the pump power of more than 24.5 dBm (both pumps) nor the bias voltage higher than $U_{bias}=-25$ V were checked

during the measurement. The lack of the saturation trend in the ER, suggests that the pump power and the reverse bias voltage can be increased, in order to achieve an even higher PSA extinction ratio.

3.3.8 Summary of CW FWM and PSA measurement

In this chapter the highest CW η_{LL} around $\lambda = 1550 \text{ nm}$ wavelength was demonstrated, to our best knowledge. The description of the CW FWM wavelength conversion as a function of the pump power, applied voltage and waveguide length is provided. In section 3.3.7 the first demonstration of the phase sensitive amplification extinction ratio (ER) as high as 20 dB in the silicon p-i-n nano-rib waveguide is demonstrated around $\lambda = 1550 \text{ nm}$ wavelength.

4

System oriented experiments of wavelength conversion

According to the results obtained in chapter 3 the silicon waveguides proved to be efficient wavelength converters even in the telecommunication range where they suffer from the two photon absorption (TPA) and the TPA induced free carrier absorption (FCA). These two mechanisms limit the CW wavelength conversion in the silicon waveguides unless a lateral p-i-n diode is used. The reverse biasing of the diode, by removing the free carriers from the waveguide, limited significantly the detrimental influence of the TPA induced FCA. As shown in section 2.2.3 an appropriate design of the waveguide and the choice of the covering layers results in a broader bandwidth of the conversion efficiency. The low linear loss α_{lin} of the waveguide needs to be assured by suitable fabrication in order to obtain the high efficiency of the pumping. The highly efficient fiber-to-waveguide coupling must be granted as well, in order to avoid the high insertion loss of the nonlinear waveguide to the system. With the setup applied in this research project, however, the incoupling loss over the 10 nm conversion efficiency bandwidth reached a level over $\alpha_{GRC} = -4.5 \text{ dB/coupler}$. In this research it was demonstrated for the first time that, even with such a level of the incoupling loss, the amplitude modulated signal experienced a highly efficient wavelength conversion and the phase modulated signal was regenerated.

This chapter describes two possibilities to use the silicon waveguide in the telecommunication system at the wavelengths around 1550 nm. In the first experiment, the amplitude modulated signal was converted using the four wave mixing (FWM) wavelength conversion mechanism. The experiment was performed on the signal modulated with 40 Gbps non-return to zero

(Non Return to Zero (NRZ)) on-off keying (On-Off Keying (OOK)) [43]. The CW pump was used to convert the signal wavelength into idler. Applying the reverse bias voltage to the p-i-n diode, it was examined, how the removal of the (TPA) induced free carriers influences the wavelength conversion of the modulated signal. The quality of the signal was measured with the bit error ratio (Bit-Error Ratio (BER)) measurement. This is discussed in section 4.1. The high extinction ratio (ER) of the phase sensitive amplification (PSA) was presented in section 3.3.7. This indicated the possibility to regenerate the phase modulated signal. Therefore, the second experiment, which is described in this chapter examined the phase modulated signal regeneration in the silicon nano-rib waveguide with reversely biased p-i-n diode. This is discussed in section 4.2.

4.1 All-optical wavelength conversion of the amplitude modulated signal

In this section it is discussed how the silicon waveguide with the lateral p-i-n diode can be used for the all-optical wavelength conversion of the modulated signal, when using the CW pump.

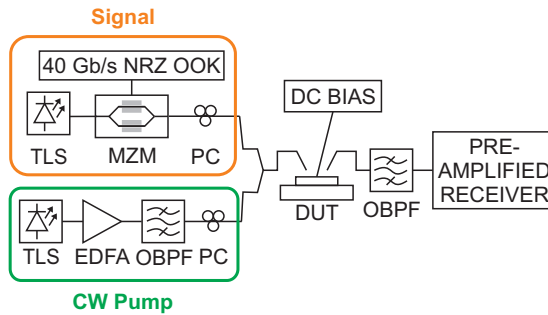


Figure 4.1: Measurement setup for the wavelength conversion of the 40 Gbps NRZ-OOK modulated signal in silicon waveguide with the lateral p-i-n diode. [43]

The wavelength conversion setup is depicted in figure 4.1. The pump arm consists of four elements: the CW laser (TLS) generating the wavelength 1552 nm, the erbium-doped amplifier (EDFA), the 0.8 nm 3-dB bandwidth optical band-pass filter (OBPF) and the fiber polarization controller (Fiber

4.1. ALL-OPTICAL WAVELENGTH CONVERSION OF THE AMPLITUDE MODULATED SIGNAL

Polarization Controller (PC)). The role of the OBPF is to suppress the out-of-band noise originating from the amplified spontaneous emission (ASE). In the "signal arm" of the setup the CW laser (TLS) is followed by the Mach-Zehnder Modulator (Mach-Zehnder Modulator (MZM)). This laser emits the signal wave at the wavelength of 1550.5 nm. The MZM modulated the amplitude of the optical signal with the non-return to zero NRZ format using On-Off keying at 40 Gb/s. Here also the polarization controller (PC) was placed to optimize the incoupling to the 4.48 cm long p-i-n waveguide (DUT). Both the signal wave and the pump wave, merged by a 3 dB coupler, were sent through the waveguide (DUT). The power was set at 7 dBm for the signal and at 27 dBm for the pump, before being coupled into the device under test (DUT).

The angle between the fiber axis and the normal to the top grating surface was set at 9° . The insertion loss of the grating coupler at this angle of incidence amounts to $\alpha_{GRC} = -4.5 \text{ dB/coupler}$. Thus the pump power ($P_p(0)$) coupled into the waveguide was 22.5 dB. In the case of the waveguides with the lateral p-i-n diode the DC reverse bias voltage was applied (DC BIAS). The narrow band (1 nm 3 dB bandwidth) optical band pass filter selects the converted signal. Then the conventional pre-amplified receiver measures the bit-error ratio BER. Before conducting the experiment of the wavelength conversion efficiency the 3-dB bandwidth of 10 nm was determined (as depicted in figure 3.36). Therefore, the chosen wavelength if the signal was 1550.5 nm and of the pump was 1552 nm.

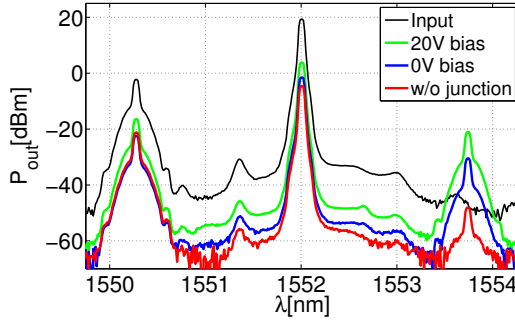


Figure 4.2: Input(black) and output spectra for the waveguides without and with the p-i-n junction. Observed η_{LL} values for the reference waveguide, 0V and 20V biased p-i-n waveguide were -26.9 dB, -8 and -4.6 dB respectively.

CHAPTER 4. SYSTEM ORIENTED EXPERIMENTS OF WAVELENGTH CONVERSION

To determine the conversion efficiency it was necessary to record the input and the output spectra. Therefore, the pre-amplified receiver was replaced by an optical spectrum analyzer (OSA). In figure 4.2 the wavelength conversion in the following waveguides were considered: the waveguide without p-i-n junction (C), the waveguide with p-i-n junction and reverse bias voltage of 0 V (B) and the waveguide with p-i-n junction with the reverse bias voltage $U_{bias} = -20$ V (A). The wavelength conversion efficiency of -26.9 dB (for C), -8 dB (for B) and -4.6 dB (for A) was observed. As described in section 2.5 the applied reverse bias voltage results in the reduction of the FCA. The substantial enhancement in the conversion efficiency was obtained in this experiment due to such decrease of the FCA (similarly to results reported in sections 3.3.5 and 3.3.6).

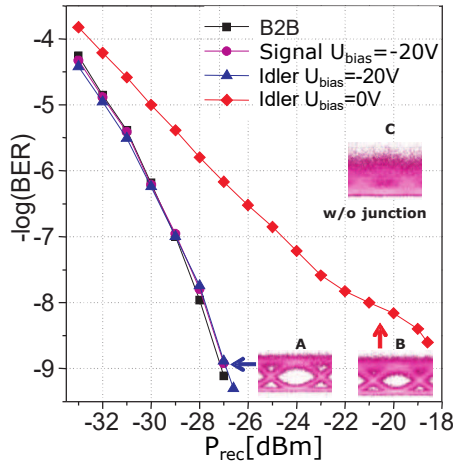


Figure 4.3: Measured BER versus received power: back-to-back, output signal and idler at -20 V reverse bias voltage and idler at 0 V bias voltage. The insets show the eye diagrams for the idler at -20 V bias voltage (A), at 0 V bias voltage (B) and for the waveguide without junction (C)

The quality of the converted signal (idler) was measured using the BER and is presented in figure 4.3. In the case of the waveguide without p-i-n junction the low conversion efficiency due to the FCA, resulted in a closed eye-diagram (figure 4.3 inset (C)). Thus, it was not possible to examine the BER. Using the p-i-n waveguide with 0 V bias voltage (4.3 inset (B)) the idler power was still strongly attenuated by the sample and needed am-

4.2. PHASE REGENERATION OF DPSK MODULATED SIGNALS

plification with an additional EDFA at the output. Amplifying such a weak signal lowers, however, the optical signal-to-noise ratio (Optical Signal-to-Noise Ratio (OSNR)) resulting in a moderately opened eye and the power penalty of over 8 dB. Applying the reverse bias voltage of 20 V to the waveguide's p-i-n diode suppressed the power penalty to a negligible value of 0.2 dB ($\text{BER}=10^{-9}$). Furthermore, the power of the converted signal (idler) was high enough to be detected without the output EDFA.

4.2 Phase regeneration of DPSK modulated signals

In this section the second experiment is presented. It is a system experiment realized in a joint research effort with Danmarks Tekniske Universitet DTU, published in [45]. This system experiment examined the phase regeneration of the phase modulated signal.

The results presented in section 3.3.7 indicate that the phase sensitive amplification in the silicon waveguide can be used for the phase squeezing and thus for the phase regeneration of the DPSK signal. Moreover, from the results it can be concluded that some improvements of the nano-rib silicon waveguide with the p-i-n junction are inevitable to make it competitive against the available solutions for a DPSK signal phase regeneration. The following could be improved: the coupling efficiency could be increased, the linear loss could be decreased as well as the geometry could be adapted in order to obtain the anomalous dispersion. The large Kerr coefficient and the high light confinement which is possible in the nano-rib waveguides would make them suitable candidates to replace the Highly Nonlinear Fiber (HNLF).

Figure 4.4 presents the changes in the static characterization setup shown in figure 3.40 made in order to investigate the scheme under dynamic conditions, i.e. with a DPSK-modulated signal. The optical processor was used to separate the signal from the pumps after the frequency comb generator by outputting it to a different port so that it could be modulated in the DPSK format at 10 Gbps using a standard Mach-Zehnder modulator (MZM) driven in push-pull operation by a non return-to-zero pseudo-random binary sequence (PRBS) of length $2^{15} - 1$. The pumps were propagated through 13.5 m of standard Single Mode Fiber (SMF) and coupled back together with the signal via a 3-dB coupler, to compensate for the delay in the other arm. The length of SMF was optimized in order to approximately match the pumps and the signal path lengths in order to ease

CHAPTER 4. SYSTEM ORIENTED EXPERIMENTS OF WAVELENGTH CONVERSION

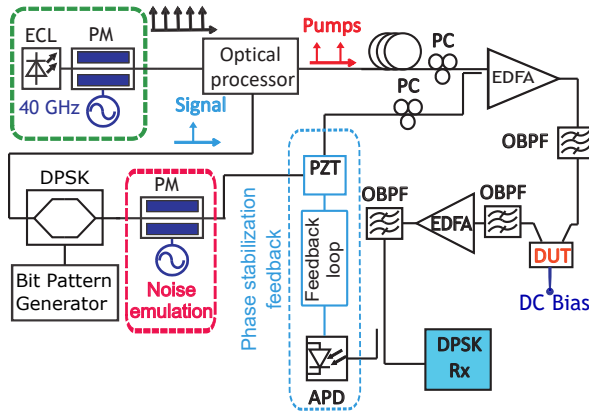


Figure 4.4: Experimental setup for dynamic phase regeneration of a 10 Gbps DPSK signal.

the operation of the phase control loop aiming at compensating for slow thermal drifts. A polarization controller (PC) in each arm was used to maximize the incoupling to the waveguide. After coupling back together, the three waves were amplified to a total power of 24 dBm, band-pass filtered and injected into the DUT. This relatively low input power has been chosen for the experiment, to minimize the coupling drifts due to the thermal effects in the DUT and the risk of the damages. Using a temperature controlled stage would allow to increase the power and thus enhance the performance. The p-i-n junction was reverse-biased with 25 V keeping the fiber-chip-fiber losses of the 4.48 cm long waveguide at around 14 dB. At the waveguide output a pair of optical band-pass filters (OBPF) with 0.8-nm and 0.3-nm bandwidths were used to select the signal and send it to the pre-amplified DPSK balanced receiver for the BER testing. A second EDFA located between the OBPFs was used to compensate for an extra insertion loss. Finally, phase-to-intensity demodulation in the receiver was performed by a 1-bit (100 ps) delay interferometer followed by a balanced photodiode with a cut-off frequency of 45 GHz and an electrical low-pass filter with a bandwidth of 7.5 GHz. The splitting of pumps and signal and their propagation along different paths inevitably results in a loss of phase coherence due to thermal effects, even when balancing the paths lengths. In order to lock the waves in phase, 10% of the signal power was detected by a slow speed avalanche photodiode APD after the OPBF's fol-

4.2. PHASE REGENERATION OF DPSK MODULATED SIGNALS

lowing the waveguide and used as a reference for a feedback loop based on a piezoelectric transducer PZT. The PZT has a bandwidth of 15 kHz and therefore is able to compensate for the slow thermal drift between the waves. In order to investigate the regeneration properties of the scheme, a phase noise was emulated deterministically by adding sinusoidal phase modulation to the DPSK signal using a phase modulator (PM) driven by a single RF tone generated from an independent unsynchronized RF source. The modulation index and the frequency of the noise tone have been varied to verify the effectiveness of the regenerator under different operation conditions.

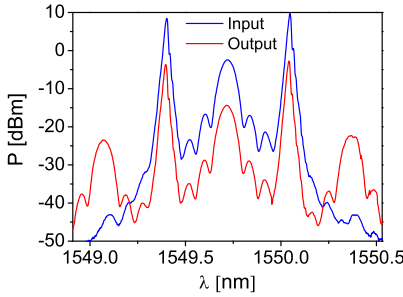


Figure 4.5: Optical spectra measured at the input and output of the waveguide under dynamic operation with the 10 Gbps signal.

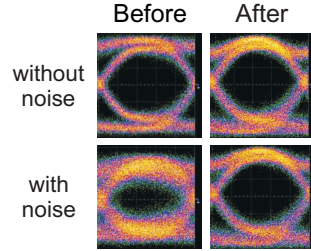


Figure 4.6: Eyes diagrams at the receiver for -36 dBm of received power before (left) and after (right) regeneration, without (top) and with (bottom) phase noise generated by a 5 GHz tone with a modulation index of 0.57.

Spectra at the input and the output of the waveguide are reported in figure 4.5 together with the eye diagrams in figure 4.6 before and after regeneration under two test conditions: when no driving signal is applied to the phase modulator (PM) ("without noise") and when the phase noise is emulated by a 5-GHz RF sinusoidal signal with a modulation index (V_{pp}/V_{π}) of 0.57 ("with noise"). Clear and open eye diagrams were observed after the regeneration with a little distortion compared to the back-to-back reference with no noise added and a significant improvement compared with the back-to-back with an additional phase noise. The BER of the signal before and after regeneration was measured for no degradation as well as phase noise frequencies of 4 GHz, 5 GHz and 6 GHz, in order to properly

CHAPTER 4. SYSTEM ORIENTED EXPERIMENTS OF WAVELENGTH CONVERSION

assess the regenerating performance of the waveguide. All the measurements have been carried out keeping the modulation index (V_{pp}/V_π) of the phase noise fixed at 0.57.

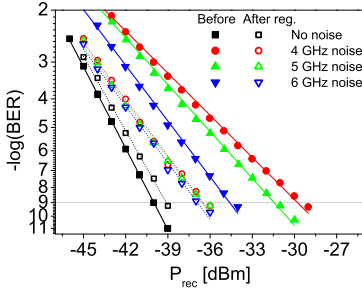


Figure 4.7: BER as a function of the received power for different phase noise loading conditions before (solid symbols) and after (hollow symbols) regeneration. Modulation index of 0.57 was used.

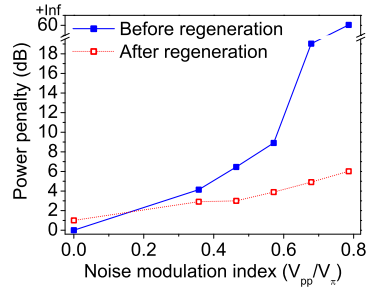


Figure 4.8: Power penalty (compared to back-to-back for a $BER=10^{-9}$) as a function of the modulation index of the 5-GHz radio frequency tone used to emulate the phase noise

The resulting BER curves as a function of the received power are shown in figure 4.7. In the absence of added noise, the scheme results in a power penalty of around 1 dB with respect to the back-to-back reference taken at the powermeter (PM) output. However, when phase noise is added to the signal, the regenerated output shows an improved receiver sensitivity (defined at a $BER = 10^{-9}$) for all the three considered "phase noise" frequencies, enabling to decrease the power penalty from 10 dB down to less than 3.5 dB. The degradation caused by increasing the noise frequency is partially mitigated by the electrical low-pass filter at the receiver. This can be observed on the BER plots of the signal before regeneration. No significant correlation can be seen between the performances of the regenerated output and the frequency chosen for the noise emulation. The last aspect that was investigated was the impact of the modulation index on the regeneration performance for a fixed noise frequency (5 GHz). The power penalty at $BER = 10^{-9}$ with respect to back-to-back without degradation is reported in figure 4.8 as a function of the modulation index, before and after regeneration. The results show that an increase of the phase noise modulation index causes a slow increase in the power penalty for the re-

4.2. PHASE REGENERATION OF DPSK MODULATED SIGNALS

generated signal. The degradation, however, advances faster for the signal without regeneration. This leads to an error floor at a $BER = 10^{-3}$ when the modulation index of the RF tone reaches 0.78. The corresponding regenerated signal can achieve error-free performances with a penalty below 6 dB.

5

State of the Art

In this thesis we investigated possibilities enabled by integration of the p-i-n junction with the silicon nano-rib waveguide. For the wavelengths around $1.55\text{ }\mu\text{m}$ silicon exhibits TPA and thus also FCA effects due to its energy bandgap [27, 35, 85–87]. This impeded its applicability for the non-linear application.

With limited FCA the nonlinearity of silicon allows for efficient wavelength conversion as well as PSA and PSA based signal regeneration. Even though its nonlinearity coefficient γ is lower than the maximum achieved in α -Si, crystalline silicon offers stability of material properties and reliability. Well known technology used for electronics circuitry enables monolithic integration of optical and electronic circuits on one SOI chip. The platform also offers the possibility to engineer dispersion and loss by change in the waveguide dimensions and claddings and thus enhance nonlinear properties [48, 52, 87].

Two approaches not requiring technology effort were so far used to bypass TPA and FCA. One, was to operate in the pulse mode with the repetition rate low enough (e.g tens of MHz) to avoid the accumulation of the electrons and holes in the waveguide region [88]. The second is to operate in the mid-infrared wavelength range [89] escaping from TPA and thus from FCA as well. Many research groups moved towards wavelengths longer than $2\text{ }\mu\text{m}$ [90, 91]. Both of these methods, however, exclude applications demanding continuous wave (CW) operation in telecommunication wavelength range around 1550 nm . The remaining method to suppress FCA is to decrease free carrier lifetime. Several groups have doped silicon waveguides with variety of ions to create recombination centers for electrons and holes. Early promising results were obtained with the He ions by

Liu and Tsang [66] where the reported effective lifetime of carriers was decreased from 100 to 1.9 ns with increase of propagation loss of about 0.3 dB/cm due to implant dosis of 10^{12} cm^{-2} . The solutions with other ions e.g. Au [67], Ar [68], O [69, 70] or Si [71] decreasing FCA increased the propagation loss due to scattering from implants. The severe decrease in transmission through the doped waveguides makes the devices in most of the cases unfeasible.

The active carrier removal with the p-i-n diode along the waveguide proposed by Rong et al. [38, 64, 72, 73] proved to be the direction to follow in decreasing concentration of the electrons and holes in the waveguide. Applying this method, the continuous wave (CW) Raman laser was demonstrated and enabled an efficient continuous-wave wavelength conversion via FWM. However, at the beginning of this work only relatively low wavelength conversion efficiencies had been reported in silicon waveguides. Malouthe et al. [65] reported an efficiency of -5.5 dB, and before that, Rong et al. obtained 8.5 dB in waveguides with $1.5 \times 1.5 \mu\text{m}$ rib waveguides with p-i-n [72]. To the best of my knowledge there was no report of high efficiency CW FWM at 1550 nm in nano-rib p-i-n waveguides until this work. In parallel to the work on this thesis Ong et al. presented the results of -4.4 dB [59]). The authors used only 160 mW in the waveguide and it is not sure why they did not exceed this power. Hence the highest CW conversion efficiency around 1550 nm wavelength to the best of my knowledge was reported in [61] and contributed to this thesis. Major results reported in the literature on the CW FWM conversion efficiency are summarized in the Table 5.1. The conversion efficiency η_{LL} is output idler to output signal conversion efficiency (imbalance between output at the signal wavelength originally coupled into the waveguide and the power measured at the idler (converted via FWM process)), α_{lin} is the linear loss coefficient, λ_{pump} the pump wavelength and L is the waveguide length.

Max. η_{LL} [dB]	α_{lin} [dB · cm ⁻¹]	λ_p [nm] (P_{P0} [mW])	$W_{wg} \times$ $H_{wg} \times S_{wg}$ [nm]	L_{wg} [cm]	Wave- guide type	U_{bias} [V]	Year [Ref.]
-8.6	0.4	1550 (450)	1500 x 1500 x 700	8	SOI rib	-25	2006 [42]
-4.4	0.74	1550 (160)	650x220	6.35	SOI rib	-20	2013 [59]
-0.7	0.9	1552 (400)	500x220	4.0	SOI rib	-20	2012 This work
-9.6	<1.5	1550 (110)	500 x 300	1.8	SOI wire	-	2007 [48]
-5.5	0.6	1552.12 (320)	600 x 340 x 210	2.5	SOI rib	-	2008 [65]
-40	15	1550 (35)	589 x 220 ¹	0.4	slot	-	2009 [33]

Table 5.1: Comparison of the CW wavelength conversion in SOI waveguides around the 1.5 μm wavelength. Given value of the bias voltage indicates presence of the lateral p-i-n diode.

6

Conclusions

At the beginning of the thesis the state-of-the-art in the nonlinear optical platforms was discussed. It was also explained why from these platforms the silicon on insulator (SOI) was selected. Furthermore, the disadvantages and advantages of the silicon material in respect to supporting nonlinear optical effects were discussed. The following disadvantages were identified: the linear loss, the two photon absorption (TPA) and the TPA induced free carrier absorption (FCA). On the other hand the advantageous properties of silicon were listed. First and the most important advantage is the high nonlinear optical Kerr coefficient around the 1550 nm wavelength. The high refractive index makes it possible to confine the light in the sub-micron cross-section of the waveguide. The high confinement with the high nonlinear optical Kerr coefficient leads to the high nonlinear coefficient (γ) of the sub-micron silicon waveguide.

Nevertheless, such high confinement results in the high light intensity in the silicon material and gives rise to the TPA and TPA induced FCA. The TPA results from the energy bandgap. The light at the wavelength around 1550 nm propagating through the silicon waveguide at a sufficiently high power causes additional loss. This loss cannot be avoided at this wavelength range. The TPA induced FCA, however, can be substantially decreased. The other important factor considering nonlinear optical effect in silicon is an optical dispersion. To support four wave mixing in the silicon waveguide the anomalous dispersion is preferred. Although the silicon material is characterized with the normal dispersion, the anomalous dispersion can be obtained by constructing of the suitable shape and dimensions of the waveguide.

In the theoretical part of this thesis the optical properties of the silicon and

the propagation of the wave in the nonlinear Kerr medium were introduced. With this background it was possible to define the direction of the silicon waveguide development in order to support the FWM effect. The sub-micron waveguide cross-section was chosen to assure the small nonlinear effective area. Moreover, the impact of the following parameters on the waveguide dispersion was examined: the width of the rib, the height of the rib, the thickness of the slab and the material covering the waveguide. The calculations results showed which dimensions can be used in order to obtain the anomalous dispersion in a silicon nano-rib waveguide. Additionally, it became clear that the free carriers substantially contribute to propagation loss while the light with a high power is sent through the waveguide. Thus, a suitable method of the free carriers removal from the waveguide had to be chosen. For this purpose ? the lateral p-i-n junction was added along the waveguide structure.

The electrical simulations performed within this thesis resulted in the design of the lateral p-i-n diode, which efficiently removes the free carriers from the waveguide region. In this place it must be mentioned that the electrical calculation contained some simplifications and did not fully fit to the measured values. Nevertheless the trends obtained from simulations were experimentally confirmed. It was also analyzed how the optical loss depends on the overlap of the mode of the light with the doped regions of the lateral diode.

The simulations performed in the theoretical part of the research were applied to design the nano-rib silicon waveguide with the lateral p-i-n diode. The waveguides were realized in the BiCMOS pilot line at Leibniz Institute IHP in Frankfurt(Oder). The height of the waveguides was enforced by the technology used for fabrication and the realization of the experimental samples within the multi-purpose wafer. This height assured the waveguides with the low linear loss.

When measuring the loss it was observed that the free carriers were present in the waveguides even before the use of the high power of the light. The measured optical loss of the waveguides without the bias voltage amounted to 2.1 dB/cm. Applying the reverse bias voltage to the p-i-n diode lateral to the waveguide allowed to decrease the loss to the level of below 1 dB/cm. The dispersion of the silicon nano-rib waveguides was measured using the MZI structures fabricated together with the waveguides. The measured value of the dispersion coefficient $D = -1.6\text{ps}/\text{n}\cdot\text{m}$ for the waveguides with the height of 220 nm at the wavelength of 1550 nm. The result falls in between the values determined in the simulations

and taking into account only single nitride or single oxide cladding. The fabricated sample, however, had both oxide and nitride cladding on top of the waveguide rib. The higher waveguides confirmed the simulated values. The waveguide with the rib height of 300 nm exhibits very low normal dispersion and the waveguides with the rib height of 400 nm exhibit the anomalous dispersion.

In order to achieve the FWM in the silicon waveguide the high power light was coupled into the waveguide. Under this condition additional loss mechanisms became important, which are present in the silicon waveguide. These were the TPA and the TPA induced FCA. The two mechanisms are dependent on the optical power coupled into the waveguide. Therefore they were characterized at the different power levels of the light coupled into the waveguide. Later, several experiments were conducted, in order to use the potentially high FWM effect in the silicon waveguide to convert the wavelength of light. The strength of the FWM effect depends on the phase shift between the high power light at one wavelength and the weak power light at another wavelength. Hence, measurements of the PSA were performed.

The nonlinear properties of the silicon nano-rib waveguides were characterized in several experiments. The experiments were performed with the CW pump light at the wavelength around 1550 nm. The CW FWM wavelength conversion efficiency η_{LL} equals -0.7 dB was achieved. It is important to note that, this is the highest value reported until now around the 1550 nm wavelength. Moreover, the 3-dB bandwidth of the conversion efficiency of 10 nm was obtained in the 220 nm high waveguides. Furthermore, the measurement of the PSA in the silicon waveguides with the lateral p-i-n diode was performed. In this experiment the PSA extinction ratio as high as 20 dB was obtained. It is crucial that both of this substantial achievements were obtained by applying the reverse bias voltage to the lateral p-i-n diode along the waveguide.

Additionally two experiments were performed, in order to check whether the silicon waveguides can be used in the fiber optic telecommunication system. First experiment demonstrated the wavelength conversion of the 40 Gb/s NRZ OOK signal. The BER was measured to assess the quality of the converted signal. With the applied reverse bias voltage the negligible power penalty of 0.2 dB was achieved. Furthermore the regeneration of the DPSK modulated signal was demonstrated with the simulated sinusoidal distortions at different frequencies and modulation depths.

CHAPTER 6. CONCLUSIONS

In the opinion of the author of the thesis further improvements shall be focused on the development of the high silicon nano-rib waveguide with the lateral p-i-n diode in order to achieve the anomalous dispersion. At the same time the linear loss below 1 dB/cm must be assured. Provided that the anomalous dispersion of the waveguide can be obtained and the waveguide loss can be lowered to 0.5 dB/cm with known optical nonlinear limiting TPA and FCA the CW FWM gain of about 8 dB should be feasible.

List of Acronyms and Chemical Symbols

Acronym or Chem. Symbol	Description
α -Si	amorphous silicon
$\text{Al}_x\text{Ga}_{1-x}\text{As}$	aluminum gallium arsenide
APD	Avalanche Photo Diode
As	arsenic
As_2S_3	arsenic sulfide
ASE	Amplified Spontaneous Emission
Au	gold
B	boron
BER	Bit-Error Ratio
CPL	Fiber Optic Coupler
c-Si	crystalline silicon
CW	Continuous Wave
DFG	Deutsche Forschung Gemeinschaft
DPSK	Differential Phase Shift Keying
DTU	Danske Tekniske Universitet
DUT	Device Under Test
DUV	Deep Ultra Violet
EDFA	Erbium Doped Fiber Amplifier
ER	Extinction Ratio
FCA	Free Carrier Absorption
fft	Fast Fourier Transform
FPC	Fiber Polarization Controller
FWM	Four Wave Mixing
GRC	Grating Coupler
HHI	Fraunhofer Heinrich Herz Institute
HNLF	Highly Nonlinear Fiber
ICP	Inductively Coupled Plasma

List of Acronyms and Chemical Symbols

Acronym or Chem. Symbol	Description
ifft	Inverse Fast Fourier Transform
IHP	Institute for High Performance Microelectronics
IL	Insertion Loss
MZI	Mach-Zehnder Interferometer
MZM	Mach-Zehnder Modulator
NLSE	Nonlinear Schrödinger Equation
NRZ	Non Return to Zero
OBPF	Optical Band-Pass Filter
OFDR	Optical Frequency Domain Reflectometry
OOK	On-Off Keying
OSA	Optical Spectrum Analyzer
OSNR	Optical Signal-to-Noise Ratio
PC	Fiber Polarization Controller
PSA	Phase Sensitive Amplification
PWM	Optical Power Meter
PZT	Piezoelectric Transducer
RF	Radio Frequency
Si	silicon
Si ₃ N ₄	silicon nitride
SiO ₂	silicon dioxide
SMF	Single Mode Fiber
SOI	Silicon On Insulator
SPM	Self Phase Modulation
TEC	Temperature Controller
TLS	Tunable Laser Source
TPA	Two Photon Absorption
TUB	Technische Universitaet Berlin
VOA	Variable Optical Attenuator
XPM	Cross Phase Modulation

List of symbols

Symbol	Description	Unit
A	slowly varying amplitude along z direction, in this thesis relation between amplitude and optical power is $ A ^2 = P$	V/cm
A_{eff}	effective area A_{eff} of the waveguide	cm^{-2}
$\alpha_{FCA,dB}$	absorption due to free carriers	$dB \cdot cm^{-1}$
α_{GRC}	incoupling loss due to the grating coupler	$dB/coupler$
α_{lin}	linear loss	$dB \cdot cm^{-1}$
α_{TPA}	loss coefficient due to TPA	cm^{-1}
β	mode propagation constant	m^{-1}
β_1	inverse of the group velocity	s/m
β_2	group velocity dispersion	s^2/m
β_n	n -th order dispersion term	s^n/m
β_{TPA}	two photon absorption coefficient	m/W
BW	FWM bandwidth	nm
χ	optical susceptibility	
d	grating coupler etch depth	nm
$\Delta\alpha_{FCA}$	excess propagation loss due to the presence of free carriers	
$\Delta\alpha_{pin}$	excess waveguide optical propagation loss due to the presence of doping regions aside a waveguide	dB/cm
D_{cl}	cladding cross-section area	cm^2
\hat{D}	differential operator used in symmetric split step fourier method accounting for linear loss and dispersion	
D	material dispersion coefficient	$ps/(nm \cdot m)$
D	electrical displacement	C/cm^2
Δn_{FCD}	change in the refractive index due to the free carriers	
D_{Si}	material dispersion coefficient of silicon	$ps/(nm \cdot m)$
D_{Si3N4}	material dispersion coefficient of silicon nitride	$ps/(nm \cdot m)$

List of symbols

Symbol	Description	Unit
D_{sub}	substrate cross-section area	cm^2
D_{tot}	total cross-section area of waveguide consisting of cladding-, substrate- and waveguide area	cm^2
D_{wg}	waveguide cross-section area	cm^2
E	electrical field	V/cm
\mathcal{E}_{BD}	break down field	V/cm
E_{bias}	bias voltage	V/cm
E_g	energy gap	eV
ε_{Si}	relative silicon permittivity	
η_{0L}	four wave mixing wavelength conversion efficiency comparing power of the idler wave at the output of the waveguide to the power of the signal wave at the waveguides input	dB
η_{LL}	four wave mixing wavelength conversion efficiency comparing powers of the idler and signal wave at the output of the waveguide	dB
$\mathcal{F}_E(x, y)$	vectorial electric mode profile	
$\mathcal{F}_E(x, y, t)$	vectorial electric transverse field distribution of the waveguide mode	
$\mathcal{F}_H(x, y)$	vectorial magnetic mode profile	
$\mathcal{F}_H(x, y, t)$	vectorial magnetic transverse field distribution of the waveguide mode	
ϕ	phase of the wave	rad
g	grating coupler groove width	nm
G	gain of the signal while four wave mixing giving ratio between power of the signal wave at the output to power of signal wave at the input of the waveguide	dB
γ	nonlinear coefficient of the waveguide dependent on Kerr coefficient n_2 and effective area A_{eff} of the waveguide	$(W \cdot m)^{-1}$
G_{TPA}	free carriers generation rate via TPA mechanism	$cm^{-3}s^{-1}$

Symbol	Description	Unit
H	magnetic field	A/cm
H_{GRC}	grating coupler height	nm
H_{wg}	waveguide height	nm
i	imaginary unit $i = \sqrt{-1}$	
I_{damage}	optical intensity damage threshold of silicon	$ps/(nm \cdot m)$
I_d	dark current of the p-i-n diode	A
IL	insertion loss of the waveguide	dB
I_{pin}	current flowing across the p-i-n diode	A
k	wave vector	nm^{-1}
k_0	wave number	nm^{-1}
λ	wavelength	nm
λ_i	idler wavelength	nm
λ_p	pump wavelength in pump degenerated FWM scheme	nm
λ_p	pump wavelength	nm
λ_s	signal wavelength	nm
L_{eff}	effective length	cm
L_{wg}	waveguide length	cm
μ_e	drift mobility of electrons	$cm^2/(V \cdot s)$
μ_h	drift mobility of holes	$cm^2/(V \cdot s)$
N	impurity concentration	cm^{-3}
n_0	refractive index of material	
n_1	linear part of refractive index	
n_2	Kerr coefficient	$m^2 \cdot W^{-1}$
N_A	acceptor impurity concentration	cm^{-3}
N_A	acceptor ions concentration	cm^{-3}
n_{air}	refractive index of air	
n_{cl}	refractive index of the cladding material	
N_D	acceptor impurity concentration	cm^{-3}
N_D	donors ions concentration	cm^{-3}
N_e	free electrons density	cm^{-3}

List of symbols

Symbol	Description	Unit
n_{eff}	complex effective refractive index	
n_g	group index	
N_h	free holes density	cm^{-3}
\hat{N}	differential operator used in symmetric split step fourier method accounting for nonlinear loss and phase shift	
N_i	intrinsic carriers concentration	cm^{-3}
n_{Si}	real part of the linear refractive index of silicon	
n_{Si3N4}	real part of the linear refractive index of silicon nitride	
n_{SiO2}	real part of the linear refractive index of silicon oxide	
n_{sub}	refractive index of the substrate material, in this thesis this refer to the SiO_2 buffer oxide layer	
ν	optical frequency	s^{-1}
n_{wg}	refractive index of the waveguide material, in this thesis it is refractive index of silicon	
\mathbf{r}	position vector $\mathbf{r} = [x, y, z]$, where x,y,z are Cartesian coordinates	m
ω	angular frequency	rad/s
\mathbf{P}_{NL}	linear part of electrical polarization	C/cm^2
P	power of light	dBm, W
P_i	optical power of idler wave	dBm, W
\mathbf{P}	electrical polarization	C/cm^2
\mathbf{P}_L	linear part of electrical polarization	C/cm^2
P_p	power of optical pump light at the beginning of the waveguide(after input grating coupler)	dBm
P_s	optical power of the signal wave	dBm, W
r	grating coupler ridge width	nm

Symbol	Description	Unit
σ_{FCA}	free carriers absorption cross-section resulting from the assumption that the density of electrons generated by TPA process is equal to the density of holes	cm^2
σ_{FCD}	free carriers refractive index change cross-section resulting from the assumption that the density of electrons generated by TPA process is equal to the density of holes	
s_{wg}	waveguide slab height	nm
t	time variable	s
τ_{eff}	effective carrier lifetime - time necessary to decrease density of free carriers by 1/e	s
U_{bias}	bias voltage	V
v_e	electron drift velocity	cm/s
v_g	group velocity	m/s
v_h	holes drift velocity	cm/s
v_{sat}	free carriers saturation velocity	cm/s
w_i	intrinsic region width	nm
W_{wg}	waveguide width	nm
\hat{x}	unity polarization vector along x direction	
\hat{y}	unity polarization vector along y direction	

List of used constants

Quantity	Symbol	Value
Electron-volt energy	eV	$1eV = 1.60218 \times 10^{-19} J$
Euler's constant	e	$\sim 2.71828182845904...$
Permeability in vacuum	μ_0	$1.25663 \times 10^{-8} H/cm$
Permittivity in vacuum	ε_0	$8.85418 \times 10^{-14} F/cm$
Planck's constant	h	$4.1357 \times 10^{-15} eV \cdot s$
Speed of light in vacuum	c	$2.99792 \times 10^{10} cm/s$

Bibliography

- [1] G. P. Agrawal, *Nonlinear fiber optics*, fourth edition ed. Academic press, 2007.
- [2] R. W. Boyd, *Nonlinear Optics, Third Edition*, 3rd ed. Academic Press, 2008. [Online]. Available: <http://www.fulviofrisone.com/attachments/article/404/Boyd%20Nonlinear%20Optics,%20Third%20Edition.pdf>
- [3] C. Grillet, L. Carletti, C. Monat, P. Grosse, B. B. Bakir, S. Menezo, J. M. Fedeli, and D. J. Moss, "Amorphous silicon nanowires combining high nonlinearity, fom and optical stability," *Opt. Express*, vol. 20, no. 20, pp. 22 609–22 615, Sep 2012. [Online]. Available: <http://www.opticsexpress.org/abstract.cfm?URI=oe-20-20-22609>
- [4] C. Lacava, V. Pusino, P. Minzioni, M. Sorel, and I. Cristiani, "Nonlinear properties of algaas waveguides in continuous wave operation regime," *Opt. Express*, vol. 22, no. 5, pp. 5291–5298, Mar 2014. [Online]. Available: <http://www.opticsexpress.org/abstract.cfm?URI=oe-22-5-5291>
- [5] J. J. Wathen, P. Apiratikul, C. J. K. Richardson, G. A. Porkolab, G. M. Carter, and T. E. Murphy, "Efficient continuous-wave four-wave mixing in bandgap-engineered AlGaAs waveguides," *Opt. Lett.*, vol. 39, no. 11, pp. 3161–3164, Jun 2014. [Online]. Available: <http://ol.osa.org/abstract.cfm?URI=ol-39-11-3161>
- [6] M. Pu, L. Ottaviano, E. Semenova, and K. Yvind, "AlGaAs-on-insulator nonlinear photonics," *ArXiv e-prints*, Sep. 2015.
- [7] M. Pu, H. Hu, L. Ottaviano, E. Semenova, D. Vukovic, L. K. Oxenlowe, and K. Yvind, "AlGaAs-on-insulator nanowire with 750 nm fwm bandwidth, -9 db cw conversion efficiency, and ultrafast operation enabling record tbaud wavelength conversion," in *Optical Fiber Communication Conference Post Deadline Papers*. Optical Society of America, 2015, p. Th5A.3. [Online]. Available: <http://www.osapublishing.org/abstract.cfm?URI=OFC-2015-Th5A.3>
- [8] I. Kaminow, T. Li, and A. Willner, *Optical Fiber Telecommunications Volume VIA: Components and Subsystems*, ser. Optics and Photonics. Elsevier Science, 2013. [Online]. Available: <https://books.google.de/books?id=8V8LMI9WhGEC>

BIBLIOGRAPHY

- [9] B. Little, S. Chu, F. Johnson, V. Van, and J. Hryniewicz, "A vlsi photonics platform for microwave photonic applications," in *Microwave Photonics, 2004. MWP'04. 2004 IEEE International Topical Meeting on*, Oct 2004, pp. 6–.
- [10] D. Duchesne, M. Ferrera, L. Razzari, R. Morandotti, B. E. Little, S. T. Chu, and D. J. Moss, "Efficient self-phase modulation in low loss, high index doped silica glass integrated waveguides," *Opt. Express*, vol. 17, no. 3, pp. 1865–1870, Feb 2009. [Online]. Available: <http://www.opticsexpress.org/abstract.cfm?URI=oe-17-3-1865>
- [11] D. J. Moss, R. Morandotti, A. L. Gaeta, and M. Lipson, "New cmos-compatible platforms based on silicon nitride and hydrex for nonlinear optics," *Nature Photonics*, vol. 7, no. 8, pp. 597–607, Aug. 2013. [Online]. Available: <http://dx.doi.org/10.1038/nphoton.2013.183>
- [12] V. Ta'eed, N. J. Baker, L. Fu, K. Finsterbusch, M. R. E. Lamont, D. J. Moss, H. C. Nguyen, B. J. Eggleton, D.-Y. Choi, S. Madden, and B. Luther-Davies, "Ultrafast all-optical chalcogenide glass photonic circuits," *Opt. Express*, vol. 15, no. 15, pp. 9205–9221, Jul 2007. [Online]. Available: <http://www.opticsexpress.org/abstract.cfm?URI=oe-15-15-9205>
- [13] J. Fatome, C. Fortier, T. N. Nguyen, T. Chartier, F. Smektala, K. Mes-saad, B. Kibler, S. Pitois, G. Gadret, C. Finot, J. Troles, F. Desevedavy, P. Houizot, G. Renversez, L. Brilland, and N. Traynor, "Linear and nonlinear characterizations of chalcogenide photonic crystal fibers," *Lightwave Technology, Journal of*, vol. 27, no. 11, pp. 1707–1715, June 2009.
- [14] M. Pelusi, V. Ta'eed, M. R. E. Lamont, S. Madden, D.-Y. Choi, B. Luther-Davies, and B. Eggleton, "Ultra-high nonlinear as2 s3 planar waveguide for 160-gb/s optical time-division demultiplexing by four-wave mixing," *Photonics Technology Letters, IEEE*, vol. 19, no. 19, pp. 1496–1498, Oct 2007.
- [15] R. Neo, J. Schröder, Y. Paquot, D.-Y. Choi, S. Madden, B. Luther-Davies, and B. J. Eggleton, "Phase-sensitive amplification of light in a $\chi^{(3)}$ photonic chip using a dispersion engineered chalcogenide ridge waveguide," *Opt. Express*, vol. 21, no. 7, pp. 7926–7933, Apr 2013. [Online]. Available: <http://www.opticsexpress.org/abstract.cfm?URI=oe-21-7-7926>

- [16] H. K. Tsang, C. S. Wong, T. K. Liang, I. E. Day, S. W. Roberts, A. Harpin, J. Drake, and M. Asghari, "Optical dispersion, two-photon absorption and self-phase modulation in silicon waveguides at 1.5 μm wavelength," *Appl. Phys. Lett.*, vol. 80, no. 3, p. 416, 2002. [Online]. Available: <http://dx.doi.org/10.1063/1.1435801>
- [17] G. W. Rieger, K. S. Virk, and J. F. Young, "Nonlinear propagation of ultrafast 1.5 μm pulses in high-index-contrast silicon-on-insulator waveguides," *Applied Physics Letters*, vol. 84, no. 6, pp. 900–902, 2004. [Online]. Available: <http://scitation.aip.org/content/aip/journal/apl/84/6/10.1063/1.1645991>
- [18] A. D. Bristow, N. Rotenberg, and H. M. van Driel, "Two-photon absorption and kerr coefficients of silicon for 850–2200nm," *Applied Physics Letters*, vol. 90, no. 19, pp. –, 2007. [Online]. Available: <http://scitation.aip.org/content/aip/journal/apl/90/19/10.1063/1.2737359>
- [19] M. Dinu, F. Quochi, and H. Garcia, "Third-order nonlinearities in silicon at telecom wavelengths," *Applied Physics Letters*, vol. 82, no. 18, pp. 2954–2956, 2003. [Online]. Available: <http://scitation.aip.org/content/aip/journal/apl/82/18/10.1063/1.1571665>
- [20] H. Yamada, M. Shirane, T. Chu, H. Yokoyama, S. Ishida, and Y. Arakawa, "Nonlinear-optic silicon-nanowire waveguides," *Japanese Journal of Applied Physics*, vol. 44, no. 9R, p. 6541, 2005. [Online]. Available: <http://stacks.iop.org/1347-4065/44/i=9R/a=6541>
- [21] B. Kuyken, S. Clemmen, S. K. Selvaraja, W. Bogaerts, D. V. Thourhout, P. Emplit, S. Massar, G. Roelkens, and R. Baets, "On-chip parametric amplification with 26.5 db gain at telecommunication wavelengths using cmos-compatible hydrogenated amorphous silicon waveguides," *Opt. Lett.*, vol. 36, no. 4, pp. 552–554, Feb 2011. [Online]. Available: <http://ol.osa.org/abstract.cfm?URI=ol-36-4-552>
- [22] B. Kuyken, H. Ji, S. Clemmen, S. K. Selvaraja, H. Hu, M. Pu, M. Galili, P. Jeppesen, G. Morthier, S. Massar, L. Oxenløwe, G. Roelkens, and R. Baets, "Nonlinear properties of and nonlinear processing in hydrogenated amorphous silicon waveguides," *Opt. Express*, vol. 19, no. 26, pp. B146–B153, Dec 2011. [Online]. Available: <http://www.opticsexpress.org/abstract.cfm?URI=oe-19-26-B146>

BIBLIOGRAPHY

- [23] J. Leuthold, W. Freude, J.-M. Brosi, R. Baets, P. Dumon, I. Biaggio, M. Scimeca, F. Diederich, B. Frank, and C. Koos, "Silicon organic hybrid technology - a platform for practical nonlinear optics," *Proceedings of the IEEE*, vol. 97, no. 7, pp. 1304–1316, July 2009.
- [24] S. Sze and K. Ng, *PHYSICS OF SEMICONDUCTOR DEVICES, 3RD ED.* Wiley India Pvt. Limited, 2008. [Online]. Available: <http://books.google.de/books?id=6HfSqvSwwMAC>
- [25] B. Jalali, V. Raghunathan, R. Shori, S. Fathpour, D. Dimitropoulos, and O. Stafsudd, "Prospects for silicon mid-ir raman lasers," *Selected Topics in Quantum Electronics, IEEE Journal of*, vol. 12, no. 6, pp. 1618–1627, Nov 2006.
- [26] F. Da Ros, C. Peucheret, J. Xu, and M. Galili, "Optical processing of high dimensionality signals," Ph.D. dissertation, Technical University of Denmark, 2014.
- [27] J. R. M. Osgood, N. C. Panoiu, J. I. Dadap, X. Liu, X. Chen, I.-W. Hsieh, E. Dulkeith, W. M. Green, and Y. A. Vlasov, "Engineering nonlinearities in nanoscale optical systems: physics and applications in dispersion-engineered silicon nanophotonic wires," *Adv. Opt. Photon.*, vol. 1, no. 1, pp. 162–235, Jan 2009. [Online]. Available: <http://aop.osa.org/abstract.cfm?URI=aop-1-1-162>
- [28] G. Dziallas, "Modelling of the nonlinear signal propagation in silicon waveguides," Master's thesis, Technische Universitaet Berlin, Juni 2014.
- [29] Q. Lin, O. J. Painter, and G. P. Agrawal, "Nonlinear optical phenomena in silicon waveguides: modeling and applications," *Opt. Express*, vol. 15, no. 25, pp. 16 604–16 644, Dec 2007. [Online]. Available: <http://www.opticsexpress.org/abstract.cfm?URI=oe-15-25-16604>
- [30] Q. Lin, J. Zhang, G. Piredda, R. W. Boyd, P. M. Fauchet, and G. P. Agrawal, "Anisotropic nonlinear response of silicon in the near-infrared region," in *Conference on Lasers and Electro-Optics/Quantum Electronics and Laser Science Conference and Photonic Applications Systems Technologies*. Optical Society of America, 2007, p. CMHH3. [Online]. Available: <http://www.osapublishing.org/abstract.cfm?URI=CLEO-2007-CMHH3>

- [31] S. Neal, "Lecture 4: The interaction of light with matter." [Online]. Available: http://www1.udel.edu/chem/sneal/sln_tchng/CHEM620.bak/Resources/Chi/4.LightDielectrics.pdf
- [32] R. del Coso and J. Solis, "Relation between nonlinear refractive index and third-order susceptibility in absorbing media," *J. Opt. Soc. Am. B*, vol. 21, no. 3, pp. 640–644, Mar 2004. [Online]. Available: <http://josab.osa.org/abstract.cfm?URI=josab-21-3-640>
- [33] C. Koos, L. Jacome, C. Poulton, J. Leuthold, and W. Freude, "Nonlinear silicon-on-insulator waveguides for all-optical signal processing," *Opt. Express*, vol. 15, no. 10, pp. 5976–5990, May 2007. [Online]. Available: <http://www.opticsexpress.org/abstract.cfm?URI=oe-15-10-5976>
- [34] A. Fallahkhair, K. S. Li, and T. E. Murphy, "Vector finite difference modesolver for anisotropic dielectric waveguides," *J. Lightwave Technol.*, vol. 26, no. 11, pp. 1423–1431, Jun 2008. [Online]. Available: <http://jlt.osa.org/abstract.cfm?URI=jlt-26-11-1423>
- [35] R. A. Soref and B. Bennett, "Electrooptical effects in silicon," *Quantum Electronics, IEEE Journal of*, vol. 23, no. 1, pp. 123–129, Jan 1987.
- [36] D. Dimitropoulos, R. Jhaveri, R. Claps, J. Woo, and B. Jalali, "Lifetime of photogenerated carriers in silicon-on-insulator rib waveguides," *Applied Physics Letters*, vol. 86, no. 7, pp. 071 115–071 115–3, Feb 2005.
- [37] R. Claps, V. Raghunathan, D. Dimitropoulos, and B. Jalali, "Influence of nonlinear absorption on raman amplification in silicon waveguides," *Opt. Express*, vol. 12, no. 12, pp. 2774–2780, Jun 2004. [Online]. Available: <http://www.opticsexpress.org/abstract.cfm?URI=oe-12-12-2774>
- [38] A. C. Turner-Foster, M. A. Foster, J. S. Levy, C. B. Poitras, R. Salem, A. L. Gaeta, and M. Lipson, "Ultrashort free-carrier lifetime in low-loss silicon nanowaveguides," *Opt. Express*, vol. 18, no. 4, pp. 3582–3591, Feb 2010. [Online]. Available: <http://www.opticsexpress.org/abstract.cfm?URI=oe-18-4-3582>
- [39] Y. Zhang, C. Husko, S. Lefrancois, I. H. Rey, T. F. Krauss, J. Schröder, and B. J. Eggleton, "Non-degenerate two-photon absorption in silicon waveguides: analytical and experimental study," *Opt. Express*, vol. 23, no. 13, pp. 17 101–17 110, Jun 2015. [Online]. Available: <http://www.opticsexpress.org/abstract.cfm?URI=oe-23-13-17101>

BIBLIOGRAPHY

- [40] Y. Zhang et al., "Cross-phase modulation-induced spectral broadening in silicon waveguides," *Opt. Express*, vol. 24, no. 1, pp. 443–451, Jan 2016. [Online]. Available: <http://www.opticsexpress.org/abstract.cfm?URI=oe-24-1-443>.
- [41] L. Yin, "Study of nonlinear optical effects in silicon waveguides," Ph.D. dissertation, University of Rochester Rochester, New York, 2009. [Online]. Available: <http://www.optics.rochester.edu/workgroups/agrawal/publications/thesis/Yin.pdf>
- [42] Y.-H. Kuo, H. Rong, V. Sih, S. Xu, M. Paniccia, and O. Cohen, "Demonstration of wavelength conversion at 40 gb/s data rate in silicon waveguides," *Opt. Express*, vol. 14, no. 24, pp. 11721–11726, Nov 2006. [Online]. Available: <http://www.opticsexpress.org/abstract.cfm?URI=oe-14-24-11721>
- [43] A. Gajda, F. Da Ros, D. Vukovic, L. Zimmermann, C. Peucheret, B. Tillack, and K. Peterman, "High efficiency wavelength conversion of 40 gbps signals at 1550 nm in soi nano-rib waveguides using p-i-n diodes," in *Group IV Photonics (GFP), 2013 IEEE 10th International Conference on*, Aug 2013, pp. 160–161.
- [44] F. DaRos, D. Vukovic, A. Gajda, L. Zimmermann, K. Petermann, and C. Peucheret, "Continuous wave phase-sensitive four-wave mixing in silicon waveguides with reverse-biased p-i-n junctions," in *Optical Communication (ECOC 2013), 39th European Conference and Exhibition on*, Sept 2013, pp. 1–3.
- [45] F. DaRos, D. Vukovic, A. Gajda, K. Dalgaard, L. Zimmermann, B. Tillack, M. Galili, K. Petermann, and C. Peucheret, "Phase regeneration of dpsk signals in a silicon waveguide with reverse-biased p-i-n junction," *Opt. Express*, vol. 22, no. 5, pp. 5029–5036, Mar 2014. [Online]. Available: <http://www.opticsexpress.org/abstract.cfm?URI=oe-22-5-5029>
- [46] G. Dziallas, M. Jazayerifar, A. Gajda, L. Zimmermann, and K. Petermann, "A numerical investigation of continuous wave parametric gain in silicon nano waveguides at wavelengths around 1550 nm," in *Numerical Simulation of Optoelectronic Devices (NUSOD), 2014 14th International Conference on*, Sept 2014. [Online]. Available: <http://www.nusod.org/2014/nusod14.paper58.pdf>

- [47] L. Vivien and L. Pavesi, *Handbook of Silicon Photonics*, ser. Series in Optics and Optoelectronics. Taylor and Francis, 2013. [Online]. Available: <http://books.google.de/books?id=lypGfgJqSM8C>
- [48] M. A. Foster, A. C. Turner, R. Salem, M. Lipson, and A. L. Gaeta, "Broad-band continuous-wave parametric wavelength conversion in silicon nanowaveguides," *Opt. Express*, vol. 15, no. 20, pp. 12 949–12 958, Oct 2007. [Online]. Available: <http://www.opticsexpress.org/abstract.cfm?URI=oe-15-20-12949>
- [49] L. Jia, M. Geng, L. Zhang, L. Yang, P. Chen, T. Wang, and Y. Liu, "Wavelength conversion based on degenerate-four-wave-mixing with continuous-wave pumping in silicon nanowire waveguide," *Optics Communications*, vol. 282, no. 8, pp. 1659 – 1663, 2009. [Online]. Available: <http://www.sciencedirect.com/science/article/pii/S0030401808013229>
- [50] B. A. Daniel and G. P. Agrawal, "Vectorial nonlinear propagation in silicon nanowire waveguides: polarization effects," *J. Opt. Soc. Am. B*, vol. 27, no. 5, pp. 956–965, May 2010. [Online]. Available: <http://josab.osa.org/abstract.cfm?URI=josab-27-5-956>
- [51] I. D. Rukhlenko, M. Premaratne, and G. Agrawal, "Nonlinear silicon photonics: Analytical tools," *Selected Topics in Quantum Electronics, IEEE Journal of*, vol. 16, no. 1, pp. 200–215, Jan 2010.
- [52] S. K. Selvaraja, W. Bogaerts, P. Absil, D. Van Thourhout, and R. Baets, "Record low-loss hybrid rib/wire waveguides for silicon photonic circuits," in *Group IV Photonics, 7th International conference, Proceedings*. IEEE, 2010, p. 3. [Online]. Available: <http://photonics.intec.ugent.be/publications/publications.asp?ID=2650>
- [53] J. Degallaix, R. Flaminio, D. Forest, M. Granata, C. Michel, L. Pinard, T. Bertrand, and G. Cagnoli, "Bulk optical absorption of high resistivity silicon at 1550 nm," *Opt. Lett.*, vol. 38, no. 12, pp. 2047–2049, Jun 2013. [Online]. Available: <http://ol.osa.org/abstract.cfm?URI=ol-38-12-2047>
- [54] E. Palik, *Handbook of Optical Constants of Solids, Five-Volume Set: Handbook of Thermo-Optic Coefficients of Optical Materials with Applications*. Elsevier Science, 1997. [Online]. Available: <http://books.google.de/books?id=FeeNeEzQ3GMC>

BIBLIOGRAPHY

- [55] C. Pollock and M. Lipson, *Integrated Photonics*. Springer, 2003. [Online]. Available: <http://books.google.de/books?id=7zvsOyljCMcC>
- [56] I. H. Malitson, "Interspecimen comparison of the refractive index of fused silica," *J. Opt. Soc. Am.*, vol. 55, no. 10, pp. 1205–1208, Oct 1965. [Online]. Available: <http://www.opticsinfobase.org/abstract.cfm?URI=josa-55-10-1205>
- [57] J. Levy, "Integrated nonlinear optics in silicon nitride waveguides and resonators," Ph.D. dissertation, Cornell University, Aug 2011. [Online]. Available: <http://hdl.handle.net/1813/30764>
- [58] A. Gajda, G. Winzer, B. Tillack, K. Petermann, L. Zimmermann, H. Tian, R. Elschner, T. Richter, and C. Schubert, "High efficiency cw four-wave mixing at 1.5 μm in soi nano-rib waveguides using p-i-n diodes," in *Group IV Photonics (GFP), 2012 IEEE 9th International Conference on*, Aug 2012, pp. 225–227.
- [59] J. R. Ong, R. Kumar, R. Aguinaldo, and S. Mookherjee, "Efficient cw four-wave mixing in silicon-on-insulator micro-rings with active carrier removal," *Photonics Technology Letters, IEEE*, vol. 25, no. 17, pp. 1699–1702, Sept 2013.
- [60] A. C. Turner-Foster, M. A. Foster, R. Salem, A. L. Gaeta, and M. Lipson, "Frequency conversion over two-thirds of an octave in silicon nanowaveguides," *Opt. Express*, vol. 18, no. 3, pp. 1904–1908, Feb 2010. [Online]. Available: <http://www.opticsexpress.org/abstract.cfm?URI=oe-18-3-1904>
- [61] A. Gajda, L. Zimmermann, M. Jazayerifar, G. Winzer, H. Tian, R. Elschner, T. Richter, C. Schubert, B. Tillack, and K. Petermann, "Highly efficient cw parametric conversion at 1550 nm in soi waveguides by reverse biased p-i-n junction," *Opt. Express*, vol. 20, no. 12, pp. 13 100–13 107, Jun 2012. [Online]. Available: <http://www.opticsexpress.org/abstract.cfm?URI=oe-20-12-13100>
- [62] M. A. Ettabib, K. Hammani, F. Parmigiani, L. Jones, A. Kapsalis, A. Bogris, D. Syvridis, M. Brun, P. Labeye, S. Nicoletti, and P. Petropoulos, "Fwm-based wavelength conversion in a silicon germanium waveguide," in *Optical Fiber Communication Conference/National Fiber Optic Engineers Conference 2013*. Optical Society of America, 2013, p. OTh1C.4. [Online]. Available: <http://www.opticsinfobase.org/abstract.cfm?URI=OFC-2013-OTh1C.4>

- [63] W. S. Zaoui, A. Kunze, W. Vogel, M. Berroth, J. Butschke, F. Letzkus, and J. Burghartz, "Bridging the gap between optical fibers and silicon photonic integrated circuits," *Opt. Express*, vol. 22, no. 2, pp. 1277–1286, Jan 2014. [Online]. Available: <http://www.opticsexpress.org/abstract.cfm?URI=oe-22-2-1277>
- [64] H. Rong, R. Jones, A. Liu, O. Cohen, D. Hak, A. Fang, and M. Paniccia, "A continuous-wave raman silicon laser," *Nature*, vol. 433, no. 7027, pp. 725–728, 2005. [Online]. Available: <http://dx.doi.org/10.1038/nature03346>
- [65] W. Mathlouthi, H. Rong, and M. Paniccia, "Characterization of efficient wavelength conversion by four-wave mixing in sub-micron silicon waveguides," *Opt. Express*, vol. 16, no. 21, pp. 16735–16745, Oct 2008. [Online]. Available: <http://www.opticsexpress.org/abstract.cfm?URI=oe-16-21-16735>
- [66] Y. Liu and H. K. Tsang, "Nonlinear absorption and raman gain in helium-ion-implanted silicon waveguides," *Opt. Lett.*, vol. 31, no. 11, pp. 1714–1716, Jun 2006. [Online]. Available: <http://ol.osa.org/abstract.cfm?URI=ol-31-11-1714>
- [67] A. Gajda, J. Muller, O. Nobis, J. Bruns, I. Giunttoni, M. Krause, H. Renner, K. Petermann, and E. Brinkmeyer, "Reducing the free-carrier lifetime in silicon waveguides by controlled au doping," in *Group IV Photonics, 2008 5th IEEE International Conference on*, Sept 2008, pp. 173–175.
- [68] T. Tanabe, K. Nishiguchi, A. Shinya, E. Kuramochi, H. Inokawa, M. Notomi, K. Yamada, T. Tsuchizawa, T. Watanabe, H. Fukuda, H. Shinojima, and S. Itabashi, "Fast all-optical switching using ion-implanted silicon photonic crystal nanocavities," *Applied Physics Letters*, vol. 90, no. 3, pp. –, 2007. [Online]. Available: <http://scitation.aip.org/content/aip/journal/apl/90/3/10.1063/1.2431767>
- [69] M. Foerst, J. Niehusmann, T. Plötzing, J. Bolten, T. Wahlbrink, C. Moormann, and H. Kurz, "High-speed all-optical switching in ion-implanted silicon-on-insulator microring resonators," *Opt. Lett.*, vol. 32, no. 14, pp. 2046–2048, Jul 2007. [Online]. Available: <http://ol.osa.org/abstract.cfm?URI=ol-32-14-2046>
- [70] M. Waldow, T. Plötzing, M. Gottheil, M. Först, J. Bolten, T. Wahlbrink, and H. Kurz, "25ps all-optical switching in oxygen implanted silicon-on-insulator microring resonator," *Opt. Express*,

BIBLIOGRAPHY

- vol. 16, no. 11, pp. 7693–7702, May 2008. [Online]. Available: <http://www.opticsexpress.org/abstract.cfm?URI=oe-16-11-7693>
- [71] N. M. Wright, D. J. Thomson, K. L. Litvinenko, W. R. Headley, A. J. Smith, A. P. Knights, J. H. B. Deane, F. Y. Gardes, G. Z. Mashanovich, R. Gwilliam, and G. T. Reed, “Free carrier lifetime modification for silicon waveguide based devices,” *Opt. Express*, vol. 16, no. 24, pp. 19779–19784, Nov 2008. [Online]. Available: <http://www.opticsexpress.org/abstract.cfm?URI=oe-16-24-19779>
- [72] H. Rong, Y.-H. Kuo, A. Liu, M. Paniccia, and O. Cohen, “High efficiency wavelength conversion of 10 gb/s data in silicon waveguides,” *Opt. Express*, vol. 14, no. 3, pp. 1182–1188, Feb 2006. [Online]. Available: <http://www.opticsexpress.org/abstract.cfm?URI=oe-14-3-1182>
- [73] H. Rong, A. Liu, R. Jones, O. Cohen, D. Hak, R. Nicolaescu, A. Fang, and M. Paniccia, “An all-silicon raman laser,” *Nature*, vol. 433, no. 7023, pp. 292–294, Jan. 2005. [Online]. Available: <http://dx.doi.org/10.1038/nature03273>
- [74] A. Gajda, L. Zimmermann, J. Bruns, B. Tillack, and K. Petermann, “Design rules for p-i-n diode carriers sweeping in nano-rib waveguides on soi,” *Opt. Express*, vol. 19, no. 10, pp. 9915–9922, May 2011. [Online]. Available: <http://www.opticsexpress.org/abstract.cfm?URI=oe-19-10-9915>
- [75] *Sentaurus Device User Guide (Version J-2014.09, September 2014)*, Synopsys, September 2014. [Online]. Available: <http://www.synopsys.com/TOOLS/TCAD/DEVICESIMULATION/Pages/SentaurusDevice.aspx>
- [76] A. Singh, “Influence of carrier transport on raman amplification in silicon waveguides,” *Opt. Express*, vol. 18, no. 12, pp. 12569–12580, Jun 2010. [Online]. Available: <http://www.opticsexpress.org/abstract.cfm?URI=oe-18-12-12569>
- [77] D. Taillaert, F. V. Laere, M. Ayre, W. Bogaerts, D. V. Thourhout, P. Bienstman, and R. Baets, “Grating couplers for coupling between optical fibers and nanophotonic waveguides,” *Japanese Journal of Applied Physics*, vol. 45, no. 8R, p. 6071, 2006. [Online]. Available: <http://stacks.iop.org/1347-4065/45/i=8R/a=6071>

- [78] H. Tian, G. Winzer, A. Gajda, K. Petermann, B. Tillack, and L. Zimmermann, "Fabrication of low-loss soi nano-waveguides including beol processes for nonlinear applications," *Journal of the European Optical Society - Rapid publications*, vol. 7, no. 0, 2012. [Online]. Available: http://www.jeos.org/index.php/jeos_rp/article/view/12032
- [79] T. K. Liang, H. K. Tsang, I. E. Day, J. Drake, A. P. Knights, and M. Asghari, "Silicon waveguide two-photon absorption detector at 1.5 μm wavelength for autocorrelation measurements," *Applied Physics Letters*, vol. 81, no. 7, pp. 1323–1325, 2002. [Online]. Available: <http://scitation.aip.org/content/aip/journal/apl/81/7/10.1063/1.1500430>
- [80] L. Alloatti, C. Koos, and J. Leuthold, "Optical loss by surface transfer doping in silicon waveguides," *ArXiv e-prints*, Apr. 2015. [Online]. Available: <http://arxiv.org/abs/1504.07613v1>
- [81] B. J. Soller, D. K. Gifford, M. S. Wolfe, and M. E. Froggatt, "High resolution optical frequency domain reflectometry for characterization of components and assemblies," *Opt. Express*, vol. 13, no. 2, pp. 666–674, Jan 2005. [Online]. Available: <http://www.opticsexpress.org/abstract.cfm?URI=oe-13-2-666>
- [82] R. Duncan, B. Soller, D. Gifford, S. Kreger, R. Seeley, A. Sang, M. Wolfe, and M. Froggatt, "Ofdr-based distributed sensing and fault detection for single-and multi-mode avionics fiber-optics," in *Joint Conf. on Aging Aircraft*, 2007. [Online]. Available: <http://lunainc.com/wp-content/uploads/2012/08/OFDR-Based-Distributed-Sensing.pdf>
- [83] R. Claps, D. Dimitropoulos, V. Raghunathan, Y. Han, and B. Jalali, "Observation of stimulated raman amplification in silicon waveguides," *Opt. Express*, vol. 11, no. 15, pp. 1731–1739, Jul 2003. [Online]. Available: <http://www.opticsexpress.org/abstract.cfm?URI=oe-11-15-1731>
- [84] R. Slavik, F. Parmigiani, J. Kakande, C. Lundstroem, M. Sjoedin, P. Andrekson, R. Weerasuriya, S. Sygletos, A. D. Ellis, L. Gruener-Nielsen, D. Jakobsen, S. Herstroem, R. Phelan, J. O'Gorman, A. Bogris, D. Syvridis, S. Dasgupta, P. Petropoulos, and D. J. Richardson, "All-optical phase and amplitude regenerator for next-generation

BIBLIOGRAPHY

- telecommunications systems," *Nature Photonics*, vol. 4, pp. 690–695, 2010.
- [85] P. Dumon, G. Priem, L. R. Nunes, W. Bogaerts, D. V. Thourhout, P. Bienstman, T. K. Liang, M. Tsuchiya, P. Jaenen, S. Beckx, J. Wouters, and R. Baets, "Linear and nonlinear nanophotonic devices based on silicon-on-insulator wire waveguides," *Japanese Journal of Applied Physics*, vol. 45, no. 8S, p. 6589, 2006. [Online]. Available: <http://stacks.iop.org/1347-4065/45/i=8S/a=6589>
- [86] Q. Lin, J. Zhang, G. Piredda, R. W. Boyd, P. M. Fauchet, and G. P. Agrawal, "Dispersion of silicon nonlinearities in the near infrared region," *Applied Physics Letters*, vol. 91, no. 2, pp. –, 2007. [Online]. Available: <http://scitation.aip.org/content/aip/journal/apl/91/2/10.1063/1.2750523>
- [87] Q. Lin, J. Zhang, P. M. Fauchet, and G. P. Agrawal, "Ultrabroadband parametric generation and wavelength conversion in silicon waveguides," *Opt. Express*, vol. 14, no. 11, pp. 4786–4799, May 2006. [Online]. Available: <http://www.opticsexpress.org/abstract.cfm?URI=oe-14-11-4786>
- [88] I.-W. Hsieh, X. Chen, J. I. Dadap, N. C. Panoiu, J. Richard M. Osgood, S. J. McNab, and Y. A. Vlasov, "Cross-phase modulation-induced spectral and temporal effects on co-propagating femtosecond pulses in silicon photonic wires," *Opt. Express*, vol. 15, no. 3, pp. 1135–1146, Feb 2007. [Online]. Available: <http://www.opticsexpress.org/abstract.cfm?URI=oe-15-3-1135>
- [89] B. Kuyken, X. Liu, R. M. O. Jr., R. Baets, G. Roelkens, and W. M. J. Green, "Mid-infrared to telecom-band supercontinuum generation in highly nonlinear silicon-on-insulator wire waveguides," *Opt. Express*, vol. 19, no. 21, pp. 20172–20181, Oct 2011. [Online]. Available: <http://www.opticsexpress.org/abstract.cfm?URI=oe-19-21-20172>
- [90] X. Liu, R. M. Osgood, Y. A. Vlasov, and W. M. J. Green, "Mid-infrared optical parametric amplifier using silicon nanophotonic waveguides," *Nature Photon*, vol. 4, no. 8, pp. 557–560, Aug 2010. [Online]. Available: <http://dx.doi.org/10.1038/NPHOTON.2010.119>
- [91] S. Zlatanovic, J. Park, F. Gholami, J. Boggio, S. Moro, N. Alic, S. Mookherjea, and S. Radic, "Mid-infrared wavelength conversion in silicon waveguides pumped by silica-fiber-based source," *Selected*

Topics in Quantum Electronics, IEEE Journal of, vol. 18, no. 2, pp. 612–620, March 2012.

List of Figures

1.1	Silicon nano-rib waveguide cross-section used in optical simulations	12
1.2	Four wave mixing scheme in variants: (a) nondegenerate, (b)pump degenerate, (c) signal degenerate	19
1.3	Visual representation for the sequence of calculations performed within the symmetric split step Fourier transform method	24
2.1	Loss coefficient from free carriers at 1550 nm wavelength, assuming uniform carriers distribution	26
2.2	Refractive index n_{Si} and material dispersion coefficient of Si versus wavelength λ	28
2.3	Refractive index n_{SiO_2} and material dispersion coefficient of SiO_2 versus wavelength λ	29
2.4	Refractive index $n_{Si_3N_4}$ and material dispersion coefficient $D_{Si_3N_4}$ of Si_3N_4 versus wavelength λ	29
2.5	Silicon nano-rib waveguide with lateral p-i-n diode, schematic view showing cladding and metal contacts	31
2.6	Results of the TE mode calculation for the quasi-TE mode in the silicon nano-rib waveguide with top and bottom SiO_2 cladding.	32
2.7	Effective index n_{eff} versus λ , (Air-cladded waveguide *)	34
2.8	First order dispersion β_1 versus λ , (Air-cladded waveguide *)	34
2.9	Second order dispersion β_2 versus λ , (Air-cladded waveguide *)	34
2.10	D versus λ , (Air-cladded waveguide *)	34
2.11	D versus W_{wg} for $s_{wg} = 50 \text{ nm}$ (Air-cladded waveguide *)	35
2.12	D versus s_{wg} , for $W_{wg} = 500 \text{ nm}$, (Air-cladded waveguide *)	35
2.13	Quasi-TE mode dispersion coefficient at 1550 nm wavelength versus slab height for different waveguide rib heights and $W=500\text{nm}$ with Si_3N_4 cladding	35
2.14	Quasi-TE mode dispersion coefficient D at 1550 nm wavelength versus slab height s for different H , and $W=500\text{nm}$ with SiO_2 cladding	36
2.15	Excess loss from doping regions $\Delta\alpha_{pin}$ for a waveguide with SiO_2 cladding and $W_{wg} = 500 \text{ nm}$, $H_{wg} = 220 \text{ nm}$ (a) dependent on N and w_i with $s_{wg} = 50 \text{ nm}$ and (b) dependent on slab thickness(s) with various N and $w_i = 1.2 \mu\text{m}$	37
2.16	Insertion loss (IL) versus $P(0)$ for different τ_{eff} for $\alpha_{lin} = 0 \text{ dB/cm}$ and $L_{wg} = 1 \text{ cm}$	39

2.17	Insertion loss (IL) versus $P(0)$ for different α_{lin} , $\tau_{eff} = 50$ ps and $L_{wg} = 4$ cm.	39
2.18	Insertion loss (IL) versus $P(0)$ for different L_{wg} , $\tau_{eff} = 50$ ps and $\alpha_{lin} = 0$ dB/cm.	39
2.19	Insertion loss (IL) versus L_{wg} for different $P(0)$, $\tau_{eff} = 10$ ps and $\alpha_{lin} = 0.5$ dB/cm.	39
2.20	Input and output spectrum with the η_{0L} and η_{LL}	40
2.21	Scheme of η_{LL} determination	40
2.22	Conversion efficiency η_{0L} versus $P_p(0)$ for various carrier lifetimes τ_{eff}	42
2.23	Conversion efficiency η_{LL} versus $P_p(0)$ for various carrier lifetimes τ_{eff}	42
2.24	Gain G versus $P_p(0)$ for various carrier lifetimes τ_{eff}	42
2.25	G , η_{0L} and η_{LL} versus $P_p(0)$ for carrier lifetime $\tau_{eff}=20$ ps	42
2.26	Gain versus wavelength for anomalous(solid) and normal(dashed) dispersion of 1 ps/nm \cdot m for free carriers effective lifetime of $\tau_{eff} = 60$ ps and linear loss $\alpha = 0.5$ dB/cm, $L_{wg} = 4.48$ cm, $A_{eff} = 0.1$ μ m ² . (Input power $P_p(0)$ in dBm)	43
2.27	Gain versus wavelength at different pump power $P_p(0)$ and the two waveguide lengths 2.25 (dashed) and 4.48 cm (solid), $\alpha_{lin} = 0.5$ dB/cm, $\tau_{eff} = 60$ ps.	44
2.28	Gain versus wavelength for free carriers effective lifetime τ_{eff} of 60 and 130 ps and linear loss of 0.5 and 1dB/cm.	44
2.29	Schematic view of the silicon rib waveguide used gold doping experiment.	45
2.30	Excess linear loss $\Delta\alpha_{lin}$ and effective free carrier lifetime τ_{eff} in the 1.5 μ m Au doped silicon rib waveguide versus diffusion temperature.	46
2.31	Scheme of the waveguide with marked doping regions	48
2.32	Bias connection scheme for p-i-n assisted waveguide and free carriers generation profile	48
2.33	Electron drift velocity across the waveguides crossection for slab heights s_{wg} of 50 nm and 150 nm. (a) $P=5$ mW, $U_{bias}=0$ V (b) $P=5$ mW, $U_{bias}=-25$ V	50
2.34	Electron drift velocity decrease, due to carriers screening, across the waveguide crossection for slab heights s_{wg} of 50 nm(left) and 150 nm(right), power $P = 1$ W and bias $U_{bias} = -25$ V.	51
2.35	Excess free carrier loss coefficient $\Delta\alpha_{FCA}$ versus P in the waveguide for different U_{bias} ($w_i = 1.2$ μ m, $s_{wg} = 50$ nm).	51

LIST OF FIGURES

2.36	Free carrier lifetime τ_{eff} versus P in the waveguide for different U_{bias} , ($w_i = 1.2 \mu m$, $s_{wg} = 50 nm$).	51
2.37	$\Delta\alpha_{FCA}$ versus optical power P for w_i of 1.0, 1.2, 2.4 μm and bias voltage of 0 and $-20 V$	52
2.38	Free carrier lifetime τ_{eff} versus optical power P for w_i of 1.0, 1.2 and 2.4 μm and U_{bias} of 0 and $-20 V$	52
2.39	Free carrier lifetime τ_{eff} versus U_{bias} for different s_{wg} and P of 1mW(dashed) and 1W(solid).	53
2.40	Excess free carrier loss $\Delta\alpha_{FCA}$ versus U_{bias} for different s_{wg} and P of 1mW(dashed) and 1W(solid).	53
2.41	Free carrier lifetime τ_{eff} versus P for s_{wg} of 50 nm (dashed) and 150 nm (solid) for $U_{bias} -10 V$ and $-20 V$	53
2.42	Excess free carrier loss $\Delta\alpha_{FCA}$ versus P for s_{wg} of 50 nm (dashed) and 150 nm (solid) for $U_{bias} -10 V$ and $-20 V$	53
3.1	Schematic view of silicon nano-rib waveguide with lateral p-i-n diode, showing bottom SiO_2 , cladding, metal contacts and metal paths at the top of the structure.	56
3.2	Side cross-section scheme of the fiber grating coupler	59
3.3	SEM picture of the standard fiber grating coupler	59
3.4	Fabrication procedure of samples	60
3.5	SEM cross-section of the waveguide with covering dielectric layers	61
3.6	SEM cross-section with contact pads	61
3.7	Electrical characteristics. Dark current (I_d) versus bias voltage (U_{bias}) for the waveguide lengths L_{wg} of 1.7 cm, 2.25 cm and 4.48 cm	62
3.8	Opto-electrical characteristics for different bias voltage. Diode current I_{pin} versus incoupled pump power $P_p(0)$ for $L_{wg} = 4.48 cm$, experimental data (symbols) and quadratic fit(lines) [78].	62
3.9	Measured transmission spectra (a) and extracted values (points with dashed lines) of $\Delta\lambda_{FSR}$ with linear fit(solid lines) (b) for MZI with delay line length $\Delta L = 0.5 mm$ based on silicon nano-rib waveguide with rib heights $H_{wg} = 220, 300$ and 400 nm.	64
3.10	(a) Group index n_g and (b) dispersion coefficient D , for silicon nano-rib waveguide with rib heights H_{wg} of 220 nm, 300 nm and 400 nm, obtained from measurements.	64
3.11	Scheme of the linear loss measurement setup with temperature control and bias voltage supply	66

3.12	Transmission (fiber-chip-fiber) spectrum of the waveguides with lateral p-i-n junction and without different lengths L_{wg} . $W_{wg}=500$ nm, $H_{wg}=220$ nm, $s_{wg}=50$ nm. No voltage applied.	66
3.13	Transmission (fiber-chip-fiber) of waveguides with p-i-n (subscript pin) and without (subscript nopin) versus length L_{wg} .	66
3.14	Transmission (fiber-chip-fiber) spectrum for different V_{bias} for $L=4.48$ cm.	67
3.15	Transmission (fiber-chip-fiber) vs reverse bias voltage for 1.7, 2.25 and 4.48 cm long p-i-n nano-rib waveguides at $\lambda = 1555$ nm.	67
3.16	OFDR measurements on the 4.48cm long waveguide for different bias voltage. $W_{wg}=500$ nm, $H_{wg}=220$ nm, $s_{wg}=50$ nm.	68
3.17	Measurement setup used to determine β_{TPA} with the mode locked pulsed pump laser.	70
3.18	Resulting inverse transmission versus input pump peak power (points). The β_{TPA} from the linear fitting of the data according to formula 3.3. Waveguide without p-i-n diode.	70
3.19	Continuous wave (CW) output power $P(L_{wg})$ versus input power $P(0)$. Fitting of the model developed in section 1.2.9 to the experimental data.	71
3.20	Insertion loss (IL) versus input power $P(0)$ (after grating coupler). Fitting of the developed model in section 1.2.9 to the experimental data.	72
3.21	Input and output spectrum with the η_{0L} and η_{LL} .	73
3.22	Scheme of η_{LL} determination	73
3.23	Scheme of the first setup for CW FWM measurement in Si waveguides. Realized in cooperation with Fraunhofer HHI in Berlin	75
3.24	Output power of pump, signal and idler for two waveguides: waveguide without p-i-n junction and length of 1.7 cm(solid, no pin) and waveguide with the 0 V reverse biased lateral p-i-n diode and length 1.52 cm (dashed, with pin).	76
3.25	Conversion efficiency η_{LL} versus $P_p(0)$ for four waveguides: two waveguides without the p-i-n junction and the lengths of 1.52 cm (circles) and of 4.74 cm(triangles); two waveguides with the 0 V biased p-i-n diode and the lengths of 1.7 cm(diamonds) and 4.48 cm(squares).	76

LIST OF FIGURES

3.26	Conversion efficiency η_{LL} for L_{wg} of 1.7 cm, 2.25 cm and 4.48 cm, $P_p(0) = 26\text{dBm}$, $\lambda_p = 1552.5\text{nm}$, $\lambda_s = 1550\text{nm}$. . .	77
3.27	Conversion efficiency η_{LL} for three pump wavelengths versus signal detuning $\Delta\lambda$. $P_p(0) = 26\text{ dBm}$, $L_{wg} = 4.48\text{ cm}$, $U_{bias} = 30\text{ V}$	77
3.28	Output spectrum recorded by OSA for the waveguide of length $L_{wg} = 4.48\text{ cm}$, $P_p(0) = 26.5\text{dBm}$, $\lambda_p = 1552.5\text{ nm}$, $\lambda_s = 1550\text{ nm}$, $U_{bias} = -20\text{ V}$	78
3.29	Dependence of the η_{LL} on $P_p(0)$ for several reverse U_{bias} values, $\lambda_p = 1552.5\text{ nm}$, $\lambda_s = 1550\text{ nm}$, $L_{wg} = 4.48\text{ cm}$	78
3.30	Comparison of η_{LL} relation to incoupled pump power $P_p(0)$ for 2.25 cm and 4.48 cm long waveguide for three bias voltage levels. $\lambda_p = 1552.5\text{nm}$, $\lambda_s = 1550\text{nm}$	79
3.31	Second measurement setup for CW FWM measurement in Si waveguides. Realized in cooperation with the group at DTU.	80
3.32	Measured power of signal at input $P_s(0)$ and output $P_s(L_{wg})$ and $P_i(L_{wg})$ idler versus wavelength of the input signal λ_s for $P_p(0) = 21.5\text{ dBm}$. The input signal was always the same, thus the signal curves overlap.	81
3.33	Measured conversion efficiency η_{0L} (solid) and η_{LL} (dashed) versus wavelength of the input signal λ_s for waveguide lengths 1.7 cm, 2.25 cm, 4.48 cm, pump wavelength $\lambda_p=1552\text{ nm}$ and $P_p(0) = 21.5\text{dBm}$, $U_{bias} = 0\text{V}$	83
3.34	Measured conversion efficiency η_{0L} versus wavelength of the input signal λ_s , for waveguide lengths 1.7 cm, 2.25 cm, 4.48 cm, pump wavelength $\lambda_p=1552\text{ nm}$ and $P_p(0) = 21.5\text{dBm}$, $U_{bias} = 28.2\text{V}$	83
3.35	Measured conversion efficiency η_{LL} versus wavelength of the input signal λ_s , for waveguide lengths 1.7 cm, 2.25 cm and 4.48 cm, pump wavelength $\lambda_p=1552\text{ nm}$ and $P_p(0) = 21.5\text{dBm}$, reverse $U_{bias} = 28.2\text{V}$	84
3.36	Experimentally determined η_{LL} versus λ_s variable U_{bias} (symbols) $L = 4.48\text{ cm}$, pump power $P_p(0)=21.5\text{dBm}$, and corresponding numerically determined characteristics for different free carrier lifetimes (solid curves). (Fit parameters $\gamma = 280\text{ [1/(W} \cdot \text{m)]}$, $\beta_{TPA} = 5.6 \cdot 10^{-10}\text{cm/W}$, $A_{eff} = 0.1\text{ }\mu\text{m}^2$, $\alpha_{lin} = 1.2\text{ dB/cm}$)	84

3.37	Experimentally determined η_{0L} versus λ_s variable U_{bias} (symbols) $L = 4.48$ cm, pump power $P_p(0)=21.5\text{dBm}$, and corresponding simulated characteristics for different lifetimes (solid curves). (Fit parameters $\gamma = 280$ $[1/(W \cdot m)]$, $\beta_{TPA} = 5.6 \cdot 10^{-10} \text{cm}/W$, $A_{eff} = 0.1 \mu\text{m}^2$, $\alpha_{lin} = 1.2 \text{dB}/\text{cm}$, $D = -1.9\text{ps}/(\text{nm} \cdot \text{m})$)	85
3.38	Measured nonlinear transmission G as a function of λ_s for variable U_{bias} (symbols) $L_{wg} = 4.48$ cm, pump power $P_p(0)=21.5\text{dBm}$, and corresponding simulated characteristics for different effective lifetimes τ_{eff} (solid curves). Linear transmission curve (at $U_{bias} = -20\text{V}$) was inserted (dashed) to indicate gain. (Fit parameters $\gamma = 280$ $[1/(W \cdot m)]$, $\beta_{TPA} = 5.6 \cdot 10^{-10} \text{cm}/W$, $A_{eff} = 0.1 \mu\text{m}^2$, $\alpha_{lin} = 1.2 \text{dB}/\text{cm}$, $D = -1.9\text{ps}/(\text{nm} \cdot \text{m})$)	85
3.39	Conversion efficiency η_{LL} versus λ_s for various pump power $P_p(0)$, length $L_{wg}=4.48$ cm, $U_{bias}=-28.2$ V. Comparison of the experimental data(points) to the numerically obtained curves (solid line) for the same optical power. (Fit parameters $\gamma = 280$ $[1/(W \cdot m)]$, $A_{eff} = 0.1 \mu\text{m}^2$, $\tau_{eff} = 130$ ps), $D = -1.9\text{ps}/(\text{nm} \cdot \text{m})$)	87
3.40	Measurement setup used to determine the phase sensitive gain in silicon waveguide	88
3.41	Spectra recorded at the input and output of the 4.48 cm long waveguide for maximum and minimum gain. The total power from two pumps $P_{p1}(0) + P_{p2}(0) = 19.5\text{dBm}$	89
3.42	Phase sensitive amplification in 1.7, 2.25 and 4.48 cm long p-i-n diode waveguides and the reference waveguide without p-i-n diode with length of 4.74 cm. Total pump power 19.5 dBm	90
3.43	Phase sensitive amplification as a function of phase shift for different total pumps power after the grating coupler and bias of $U_{bias} = -20$ V. For the highest power voltage was increased to $U_{bias} = -25$ V. $L_{wg}=4.48$ cm.	90
4.1	Measurement setup for the wavelength conversion of the 40 Gbps NRZ-OOK modulated signal in silicon waveguide with the lateral p-i-n diode. [43]	94
4.2	Input(black) and output spectra for the waveguides without and with the p-i-n junction. Observed η_{LL} values for the reference waveguide, 0V and 20V biased p-i-n waveguide were -26.9 dB, -8 and -4.6 dB respectively.	95

LIST OF FIGURES

4.3	Measured BER versus received power: back-to-back, output signal and idler at -20 V reverse bias voltage and idler at 0 V bias voltage. The insets show the eye diagrams for the idler at -20 V bias voltage (A), at 0 V bias voltage(B) and for the waveguide without junction (C)	96
4.4	Experimental setup for dynamic phase regeneration of a 10 Gbps DPSK signal.	98
4.5	Optical spectra measured at the input and output of the waveguide under dynamic operation with the 10 Gbps signal.	99
4.6	Eyes diagrams at the receiver for -36 dBm of received power before(left) and after(right) regeneration, without(top) and with(bottom) phase noise generated by a 5 GHz tone with a modulation index of 0.57.	99
4.7	BER as a function of the received power for different phase noise loading conditions before (solid symbols) and after (hollow symbols) regeneration. Modulation index of 0.57 was used.	100
4.8	Power penalty (compared to back-to-back for a $\text{BER}=10^{-9}$) as a function of the modulation index of the 5-GHz radio frequency tone used to emulate the phase noise	100

List of Publications

- [1] F. DaRos, D. Vukovic, A. Gajda, L. Zimmermann, K. Petermann, and C. Peucheret. Continuous wave phase-sensitive four-wave mixing in silicon waveguides with reverse-biased p-i-n junctions. In *Optical Communication (ECOC 2013), 39th European Conference and Exhibition on*, pages 1–3, Sept 2013.
- [2] Francesco DaRos, Dragana Vukovic, Andrzej Gajda, Kjeld Dalgaard, Lars Zimmermann, Bernd Tillack, Michael Galili, Klaus Petermann, and Christophe Peucheret. Phase regeneration of dpsk signals in a silicon waveguide with reverse-biased p-i-n junction. *Opt. Express*, 22(5):5029–5036, Mar 2014.
- [3] G. Dziallas, M. Jazayerifar, A. Gajda, L. Zimmermann, and K. Petermann. A numerical investigation of continuous wave parametric gain in silicon nano waveguides at wavelengths around 1550 nm. In *Numerical Simulation of Optoelectronic Devices (NUSOD), 2014 14th International Conference on*, Sept 2014.
- [4] A. Gajda, F. Da Ros, D. Vukovic, L. Zimmermann, C. Peucheret, B. Tillack, and K. Peterman. High efficiency wavelength conversion of 40 gbps signals at 1550 nm in soi nano-rib waveguides using p-i-n diodes. In *Group IV Photonics (GFP), 2013 IEEE 10th International Conference on*, pages 160–161, Aug 2013.
- [5] A. Gajda, J. Muller, O. Nobis, J. Bruns, I. Giuntoni, M. Krause, H. Renner, K. Petermann, and E. Brinkmeyer. Reducing the free-carrier lifetime in silicon waveguides by controlled au doping. In *Group IV Photonics, 2008 5th IEEE International Conference on*, pages 173–175, Sept 2008.
- [6] A. Gajda, G. Winzer, B. Tillack, K. Petermann, L. Zimmermann, H. Tian, R. Elschner, T. Richter, and C. Schubert. High efficiency cw four-wave mixing at 1.5 μm in soi nano-rib waveguides using p-i-n diodes. In *Group IV Photonics (GFP), 2012 IEEE 9th International Conference on*, pages 225–227, Aug 2012.
- [7] Andrzej Gajda, Lars Zimmermann, J. Bruns, B. Tillack, and K. Petermann. Design rules for p-i-n diode carriers sweeping in nano-rib waveguides on soi. *Opt. Express*, 19(10):9915–9922, May 2011.
- [8] Andrzej Gajda, Lars Zimmermann, Mahmoud Jazayerifar, Georg Winzer, Hui Tian, Robert Elschner, Thomas Richter, Colja Schubert,

LIST OF PUBLICATIONS

- Bernd Tillack, and Klaus Petermann. Highly efficient cw parametric conversion at 1550 nm in soi waveguides by reverse biased p-i-n junction. *Opt. Express*, 20(12):13100–13107, Jun 2012.
- [9] K Petermann, A Gajda, G Dziallas, M Jazayerifar, L Zimmermann, B Tillack, F Da Ros, D Vukovic, K Dalgaard, M Galili, and Christophe Peucheret. Phase-sensitive optical processing in silicon waveguides. In *Optical Fiber Communication Conference (OFC 2015)*, volume Tu2F of *Optical Fiber Communication Conference - Chip-scale All-optical Processing (2015)*, page Tu2F.4, Los Angeles, United States, March 2015. OSA (ISBN: 978-1-55752-937-4).
- [10] H. Tian, G. Winzer, A. Gajda, K. Petermann, B. Tillack, and L. Zimmermann. Fabrication of low-loss soi nano-waveguides including beol processes for nonlinear applications. *Journal of the European Optical Society - Rapid publications*, 7(0), 2012.

